

Université Pierre et Marie Curie
Ecole doctorale 397 : Physique et Chimie des Matériaux
Laboratoire de Réactivité de Surface, UMR7197 / Equipe Biointerfaces

Study of the interaction between proteins and TiO₂ NPs: nature of the interfacial processes

By Thomas Degabriel

Evaluation committee:

Supervisor:	Claire-Marie Pradier	DR, UPMC
Rapporteur:	Véronique Migonney	Pr, University Paris 13
	Sandrine Morandat	MdC, UTC
Examiner:	Christine Dupont-Gillain	Pr, UCL
	Jean-François Lambert	Pr, UPMC
Co-supervisors:	Jessem Landoulsi	MdC, UPMC
	Jolanda Spadavechia	CR, CNRS

Thesis submitted to obtain
the degree of Doctor of the University Pierre & Marie Curie

Acknowledgements

I would like to thank the members of the jury for this opportunity to present the results of my research. I sincerely thank Prof Véronique Migonney and Dr Sandrine Morandat for accepting to examine my work thesis. I thank also Prof Christine Dupont-Gillain and Prof Jean-François Lambert for reviewing this work.

I especially thank my thesis director Claire-Marie Pradier for her guidance, but mostly her demand for excellence. I would like to express my gratitude to my supervisors Jessem Landoulsi and Jolanda Spadavecchia. Jessem, for his advices (scientific and human) and his unbreakable support during these three years and of course for the good times spent together; Jolanda, thank for her help and her guidance. Together we survived to the Russian taxi (and Moscow subway...), now nothing can stop us.

Special thanks to Sandra Casale for TEM images and Dalil Brouir for HR-TEM measurements and for their help and explanations. I would like to thank warmly Rute Domingos for EPM measurements and for fruitful discussion as well as for her kindness. I sincerely thank Karim El Kirat for allowing me to manipulate at the UTC and Therri Robin for his advises on DLS. A big thank also to Irma for her help in water contact angle measurements. I want also to thank David Kreher for allowing me to use spin-coater and Christophe Calers for XPS analyses.

I owe my gratitude to the whole laboratory's team, who built a welcoming, helpful, warm work environment.

I would like to thank my family and my friends for their support and their friendship during many years.

Résumé

L'utilisation de nanoparticules (NPs) dans un milieu biologique est de plus en plus importante, alors que leur assimilation et leur toxicité reste peu maîtrisée. Dans ce contexte l'objectif de ce travail est d'étudier l'interaction entre nanoparticules de dioxyde de titane (TiO_2) avec des protéines ainsi que leur possible impact sur leurs propriétés structurales. Trois protéines d'intérêt ont été choisies: une protéine de la matrice extra cellulaire, le collagène, et deux protéines du plasma sanguin, l'albumine et le fibrinogène. Le choix a été basé sur l'importance biologique de ces protéines lors des interactions avec des NPs et sur la différence de leurs structures tridimensionnelles. L'étude de l'interaction protéine-NPs a été réalisée en solution et en phase adsorbée dans différentes conditions de température et de temps d'incubation.

Dans un premier temps des nanoparticules de dioxyde de titane ont été synthétisées par voie solvothermale, afin d'obtenir des nanoparticules de tailles et de formes contrôlées. Deux types de nanoparticules ont été sélectionnés en vue d'étudier l'effet de forme et de taille sur l'interaction protéines-nanoparticules: des nano-sphères de diamètre de 8 à 10 nm et des nano-bâtonnets d'environ 8 nm de largeur et 23 nm longueur. Leur comportement en solution physiologique ainsi que leur réactivité ont été caractérisés par DLS et absorption UV montrant une inhibition des propriétés catalytiques ainsi qu'une forte aggrégation en solution tampon phosphate saline (PBS).

Dans un deuxième temps les propriétés d'adsorption du collagène en présence de nanoparticules furent étudiées sur deux types de surfaces l'une hydrophobe et l'autre hydrophile par XPS et imagerie AFM ainsi que par des mesures de forces AFM. Le comportement du collagène en solution en présence de nanoparticules a été caractérisé par ATR liquide. Les observations suggèrent que la formation des fibrilles à l'interface surface-solution de collagène est affectée par le caractère hydrophobe ou hydrophile de la surface ainsi que par la présence de nanoparticules.

Enfin les propriétés d'adsorption de la HSA et du fibrinogène en présence de nanoparticules furent étudiées sur une surface hydrophile par imagerie AFM et analyses XPS. Leur comportement en solution en présence de nanoparticules fut étudié par ATR liquide. Les résultats suggèrent deux comportements différents des protéines en présence de nanoparticules pouvant être attribués à des propriétés physicochimiques différentes des protéines. La HSA subit d'importants changements structuraux en présence de nanoparticules contrairement au fibrinogène.

L'étude en phase liquide de l'interaction protéine-nanoparticules couplée à l'étude en phase adsorbée des protéines permet de déterminer les phénomènes impliqués lors de cette interaction ainsi que leurs conséquences sur les protéines, de plus l'utilisation de nanoparticules de taille et forme différentes permet d'étudier la sensibilité des protéines à ces facteurs

Mots-clés: Surface hydrophile/hydrophobe, TEM, DLS, ATR, XPS, AFM, nanoparticules de TiO_2 , collagène, fibrinogène, albumine.

Abstract

The extensive use of NPs in a biological environment raises the problem of their assimilation or their toxicity, the main objective of this work is to study the interaction of TiO₂ NPs with proteins as well as their possible impact on the structural properties of proteins. Three proteins were chosen, a protein of the extracellular matrix, the collagen, and two proteins of the plasma blood, the albumin and the fibrinogen for their biological importance as well as for their various tridimensional structures. The study of the protein-nanoparticle interaction was realized in solution and in the adsorbed phase under various condition of temperature and incubation time.

First, titanium dioxide NPs were synthesized by a solvothermal method, NPs with controlled size and form were obtained. Two types of NPs were selected in order to study the effect of shape and size on the protein-NPs interaction: nano-spheres with a diameter of 8 to 10 nm and nano-rods with a width about 8 nm and a length of 23 nm. The behavior in physiological solution as well as the reactivity were characterized by DSL and UV absorption showing an inhibition of catalytic properties as well as a strong aggregation in phosphate buffer saline solution (PBS).

Second, the adsorption properties of the collagen in the presence of NPs were studied on two kinds of surfaces, one hydrophobic and the other hydrophilic by XPS and AFM imaging as well as by AFM force measurements. The behavior of the collagen in solution in the presence of NPs was characterized by liquid ATR. The observations suggest that the formation of fibrils at the surface-collagen solution interface is affected by the hydrophobic or the hydrophilic character of the surface as well as by the presence of NPs.

In the last part the adsorption properties of HSA and fibrinogen in the presence of NPs were studied on a hydrophilic surface by AFM imaging and XPS analyses. Their behaviors in solution in the presence of NPs were studied by liquid ATR. The results suggest two different behaviors of proteins in the presence of NPs, which can be attributed to the different physico-chemical properties of the proteins. HSA undergoes important structural changes in the presence of NPs but not fibrinogen.

The study in the liquid phase of the protein-nanoparticle interaction, coupled to study of proteins in the adsorbed phase allows determining the involved phenomenon during the protein-nanoparticle interaction as well as the consequences on protein adsorption. Moreover, the use of NPs with different sizes and shapes revealed the sensitivity of proteins to these factors.

Key-words: Hydrophilic/hydrophobic surface, TEM, DLS, ATR, XPS, AFM, TiO₂ nanoparticle, collagen, fibrinogen, human serum albumin.

List of abbreviations and acronyms

AA	Acetic Acid
AFM	Atomic Force Microscopy
BM	Methylene Blue
BzOH	Benzyl alcohol
Col	Collagen
Col-Nano_S/ Col-Nano_R	Pre-incubation solution of collagen and nano-spheres or nano-rods respectively
DLS	Dynamic Light Scattering
DMF	Dimethylformamide
EPM	Electrophoretic measurement
Fg	Fibrinogen
Fg-Nano_S/ Fg-Nano_R	Pre-incubation solution of fibrinogen and nano-spheres or nano-rods respectively
HRTEM	High Resolution Transmission Electron Microscope
HSA	Human Serum Albumin
HSA-Nano_S/ HSA-Nano_R	Pre-incubation solution of human serum albumin and nano-spheres or nano-rods respectively
I	Ionic Strength
IR-ATR	Infrared Attenuated Total Reflectance
NPs	Nanoparticles
ROS	Radical Oxygen Specie
PBS	Phosphate Buffered Saline
PFT	Peak Force Tapping
pI	Isoelectric point
PS	Poly(styrene)
Si	Silicon
TEM	Transmission Electron Microscope
TiO ₂	Titanium dioxide
XPS	X-ray Photoelectron Spectroscopy
XRD	X-Ray Diffraction

Table of contents

Introduction	13
Chapter 1: State of the art.....	17
I. Introduction	19
II. Nanomaterials	20
A. Generalities	20
B. Titanium dioxide NPs.....	22
III. Protein adsorption	32
A. Generalities	32
B. Protein adsorption on flat surface	32
C. Protein adsorption on nano-structured surface	37
IV. Protein corona phenomenon	39
A. NPs and colloidal stability.....	39
B. Mechanism of protein adsorption.....	41
C. Kinetic of protein adsorption	43
D. Protein-NPs systems from the literature	45
V. Relevancy of studied system.....	47
A. Fibrinogen.....	47
B. Collagen	48
C. HSA	50
VI. References	52
Chapter 2: Materials and methods	61
I. Synthesis of titanium dioxide NPs (TiO₂ NPs).....	63
A. Materials.....	63
B. Synthesis of titanium dioxide nano-spheres	63
C. Synthesis of titanium dioxide nano-rods.....	63
II. Adsorption procedure to study Proteins-NPs interaction	65
A. Materials.....	65
B. Preparation of proteins solutions.....	65
C. Choice of NPs.....	65
D. Preparation of wafers.....	65
E. Preparation of NPs protein solution.....	66
F. Procedure of incubation: “procedure I”	66

G. Procedure of incubation: “procedure II”	66
III. Characterization techniques	67
A. Transmission electron microscope (TEM)	67
B. Electrophoretic mobility (EPM)	67
C. Dynamic Light Scattering (DLS).....	68
D. UV absorption.....	68
E. X-Ray Diffraction (XRD).....	69
F. X ray photoelectron spectroscopy (XPS)	69
G. Infrared spectroscopy in the attenuated total reflectance mode (IR-ATR)	70
H. Atomic force microscopy (AFM).....	71
Chapter 3: Properties and fate of sphere and rod-shaped TiO₂ nano-crystals in buffer solutions simulating biological fluids: Mechanism of interaction with phosphate species.....	85
I. Introduction	87
II. Synthesis and characterization of the TiO ₂ NPs.....	89
III. Catalytic properties in phosphate buffer	94
IV. Behavior in aqueous media	96
V. Catalytic properties in phosphate buffer saline (PBS).....	102
VI. Behaviour in PBS	102
VII. Conclusion	104
VIII. References	105
Chapter 4: Evidences of supramolecular structural changes of type I collagen upon interaction with sphere and rod-shaped TiO₂ NPs	113
I. Introduction	115
II. Organization of the collagen layer in the dried state.....	117
III. Organization of the collagen layer in the hydrated state	121
IV. Mechanism of collagen-TiO ₂ NPs interaction	125
V. Conclusion	133
VI. Bibliography.....	134
Chapter 5: Interaction of TiO₂ NPs with HSA and fibrinogen proteins in solution and in the adsorbed phase	143
I. Introduction	145
II. Interaction process in liquid phase.....	147
A. Organization of the protein layer in the hydrated state	147

B. Characterization of the protein-nanoparticle interaction in solution.....	151
III. Interaction process in the adsorbed dried phase	153
A. XPS measurements on adsorbed protein layer in dried phase	153
B. Organization of the protein layer in dried state.....	156
IV. Events in liquid phase.....	159
A. Mechanism of fibrinogen-TiO ₂ NPs interaction in solution.....	159
B. Mechanism of HSA-TiO ₂ NPs interaction in solution	160
V. Events in the adsorbed phase	161
A. Mechanism of fibrinogen-TiO ₂ NPs interaction in dried state.....	162
B. Mechanism of HSA-TiO ₂ NPs interaction in dried state.....	162
VI. Conclusion	162
VII. Bibliography.....	164
Conclusion and perspectives	169

Introduction

During the last years the use of NPs in industrial and medical application has been extensively developed. NPs are now commonly used in cosmetic product, food, packaging and in a wide range of medical application such as imaging or drug delivery. It has been observed when NPs come into contact with a biological fluid their surface may be covered with macromolecules forming a 'corona' around the NPs. Two consequences are resulting from this interaction, (i) the nanoparticles may acquire new chemical and surface properties allowing them to interact with cells, (ii) the conformation of adsorbed macromolecules may be altered leading to a loss of biological function. In this context the study of the interaction between NPs and proteins is essential to improve the biomedical application of NPs and anticipate the possible adverse health effect of these last.

The corona phenomenon can be understood by combining knowledges in interface science and biochemistry. On one hand the protein adsorption onto NPs surface depends on size, surface properties of NPs and the aggregation state of NPs. On the other hand this interaction depends on the protein properties such as size, surface charge and shape. The role of interfacial processes is essential, including hydrophobic interaction, charge effect and conformational changes. Therefore, due to the high variety and various physico-chemical properties of NPs and proteins the results from the literature may look ambiguous under physiological conditions.

The system studied in this work consists of TiO₂ NPs and two plasmatic proteins, human serum albumin (HSA) and fibrinogen, and one protein from the extracellular matrix, the collagen. TiO₂ are used in many nanotechnology fields such as electronics, sensors, cosmetics, and more recently in nano-medicines, as carrier for drug delivery for targeting cancer cells. HSA and fibrinogen are one of the most important plasmatic proteins, involved in various metabolic processes (transport of drugs and coagulation respectively). Collagen is the most abundant fibrillary protein of the extracellular matrix, and constitutes the connective tissue such as skin, bone, tendon, cartilage and ligament. These proteins may indeed be involved in the fate of NPs in vivo.

The strategy developed in aims to discriminate the influence of intrinsic properties of NPs and protein and their behavior at interfaces. This includes size and shape of NPs, which was investigated

by the use of TiO₂ nano-rods and TiO₂ nano-spheres obtained by solvothermal synthesis with controlled size and shape. The protein-NPs interaction was investigated in colloidal dispersion at physiological pH under different conditions of time incubation and temperature. Then, proteins resulting from the interaction with the NPs, were characterized by their adsorption behavior onto two different substrates: a hydrophilic (silicon wafer) and a hydrophobic surface (polystyrene). The behavior of proteins at the interface is a relevant indicator of the relationship between protein structure and protein properties. In the case of fibrillar proteins such as collagen the degrees of supramolecular organization on the surface gives information about structural changes, while for a globular protein such as HSA the aggregation state will be a good indicator of protein conformational changes. This study raises several questions which we will try to answer throughout this work. (i) In which way the NPs-proteins interaction impact the protein structure (ii) What is the resulting impact on their adsorption behavior (iii) Is there a shape effect of TiO₂ NPs?

The first chapter presents the state-of-art, describing the use of NPs in biomedical field and their impact on biological system, the physical properties of TiO₂ NPs as well as the principal ways of synthesis will be described. The phenomenon involved in the proteins adsorption on flat, nanostructured and NP surfaces will be explained. Then, the particularity of the studied systems will be described.

The second chapter describes the experimental conditions as well as the used characterization technique and their contribution in the present study, particularly for the AFM measurement. The protocols of incubation and proteins adsorption are explained in details in order to explain the information that will be exploited.

The third chapter lays the background for understanding the interfacial phenomena in solution between nanoparticle and protein. This chapter described on one hand the optimization of the synthesis of the TiO₂ NPs, and on the other hand the behavior of the TiO₂ NPs in solution. The physical properties of NPs such as morphology, cristallinity and catalytic properties will be investigated by UV-vis absorption, XRD and TEM. Moreover, the behavior of NPs in solution at physiological condition will be investigated for different ionic strengths in order to determine effect of charge shielding on the NPs, the aggregation state was analyzed by DLS and sedimentation test were brought by UV-vis absorption measurements.

The fourth chapter is focused on the interaction between the collagen and TiO₂ NPs. Collagen adsorption is known to depend on the surface properties, and the ability of collagen to form structured adsorbed layer depends on the behavior of collagen in solution such as fibrillation degree. The interaction in solution between collagen and NPs was investigated by liquid IR-ATR at physiological condition of pH and several times and temperatures of incubation. The evolution of adsorbed collagen in function of the different experimental condition (time and temperature of incubation) and on the different substrate was realized by XPS measurement. The organization of the collagen on adsorbed phase was characterised by liquid and air AFM imaging on hydrophilic and hydrophobic substrates, moreover the fibrillation degrees of collagen molecules was characterized by AFM force measurement in liquid on both substrates .

The last chapter is focused on the interaction between the two plasmatic proteins (HSA and fibrinogen) with the TiO₂ NPs. Due to their physical properties a comparison point may be established to characterise the effect of size and shape of protein on the NPs proteins interaction. Interaction in solution between proteins and NPs was investigated by liquid IR-ATR at physiological condition of pH and different times and temperatures of incubation. The evolution of the adsorbed protein layer for the different experimental conditions was characterized by XPS and air and liquid AFM imaging on SiO₂ substrate.

To conclude the mains results will be summarized and some, relevant outlooks will be detailed with the aim to point out the main future challenge.

Chapter 1: State of the art

Table of contents

Chapter 1: State of the art.....	17
I. Introduction.....	19
II. Nanomaterials	20
A. Generalities	20
B. Titanium dioxide NPs.....	22
III. Protein adsorption	32
A. Generalities	32
B. Protein adsorption on flat surface	32
C. Phenomena of protein adsorption on a surface structured at the nanometers scale	37
IV. Protein corona phenomenon	39
A. NPs and colloidal stability.....	39
B. Mechanism of protein adsorption.....	41
C. Kinetic of protein adsorption	43
D. Composition of corona and studied system from literature	45
V. Relevancy of studied system.....	47
A. Fibrinogen.....	47
B. Collagen	48
C. HSA	50
VI. References	52

I. Introduction

During the last years nanotechnologies have been developed, leading to the fabrication of nano-objects with tuned dimensions and properties. For instance, NPs are now recognized as synthetic materials with considerable potential applications with biological interest. With the apparition of near field microscopes it has been possible to characterize and manipulate nano-objects. The properties of NPs are exploited in many applications, including their ability to interact with biological systems in nano-medicines. For instance, the diffusion of NPs in the organism is crucial to deliver therapeutic agents in some cases. When NPs are released in a biological environment such as plasma, they bind to proteins by various interactions forming a layer of proteins around the nanoparticle, called protein corona. The nanoparticle acquires new surface properties leading to help them enter cells. Moreover, this interaction between the proteins and the NPs can lead to a conformational change of the protein, leading to a loss of their biological function. In other cases, proteins do not adsorb to NPs surfaces, depending on the dimensions of NPs, physicochemical conditions. The results of NPs-proteins interaction are contradictory or ambiguous under physiological conditions, certainly due to the high variety and various physicochemical properties of NPs and proteins. In order to improve and control the biomedical applications of NPs and their impact in daily life, understanding the phenomena at the interface proteins-NPs is essential. This aim of this chapter is to introduce the essential background and explain the phenomena at the interface proteins-NPs, by the understanding of the different physical and chemical properties of NPs and proteins.

II. Nanomaterials

A. Generalities

NPs are defined as particulate dispersions with a size in the range of 10-1000nm. NPs can have amorphous or crystalline form and their surfaces can act as carriers for liquid droplets or gases. To some degree, nano-particulate matter should be considered as a distinct state of matter, in addition to the solid, liquid, gaseous, and plasma states, due to its distinct properties (large surface area and quantum size effects¹). For example fullerene and carbon nanotubes are materials that form NPs in crystalline form, while graphite and diamond represent a solid form. Many authors choose the limit size of nanomaterials between 50 nm and 100 nm. The choice of this upper limit being justified by the fact that some physical properties of NPs approach those of bulk when their size reaches these values. However, this size threshold varies with material type and cannot be the basis for such a classification. A legitimate definition extends this upper size limit to 1 micron, the sub-micron range being classified as nano. The recent advance in characterization tools and science (synthesis, understanding of physical phenomena) enabled the emergence of nanoscience and nanotechnology. Nanoscience is the study of phenomena and material properties at the nanoscale, while nanotechnology is the application of the knowledge to create, produce and utilize materials exploiting nano phenomenon. The differences between nanomaterials and “macro” materials can be explained by two parameters: surface effects and quantum effects of nanomaterials. Surface effect is due to the very large surface area of nanomaterials. “For illustration, a carbon micro-particle with a diameter of 60 μm has a mass of 0.3 μg and a surface area of 0.01 mm^2 . The same mass of carbon in NPs form, with nanoparticle having a diameter of 60 nm, has a surface area of 11.3 mm^2 and is composed of 1 billion NPs¹”. Moreover, the chemical reactivity increases when decreasing the particle size. Quantum effect is due to the delocalization of electrons on the surface. These factors give unique properties to nanomaterials, such as chemical property (surface reactivity, catalysis ...) and physical property (electric, electronic, thermal and optical). The distinction between nanostructured immobilized structures (such as computer processors), and free NPs have to be made (figure 1).

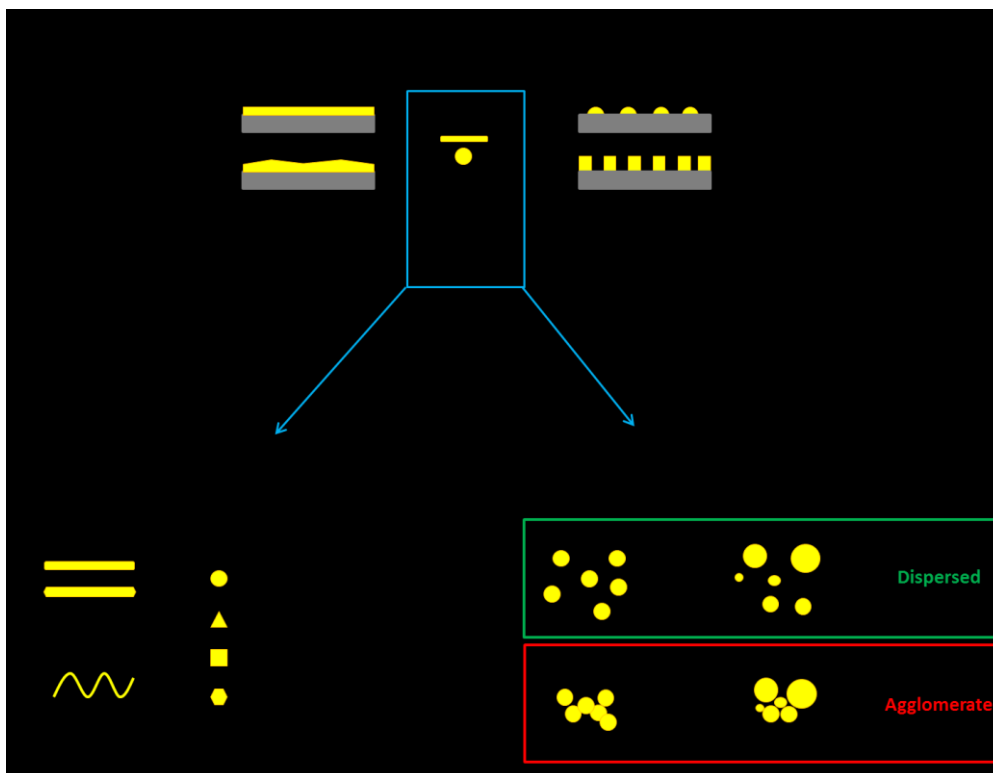


Figure 1.1: Classification of nano materials by dimensionality, morphology, and agglomeration state. Inspired from ref¹

NPs can be classified by their aspect ratio. The aspect ratio is calculated as the average ratio of the highest to the lowest dimension of the nanoparticle. As shown on figure 1, high aspect ratio includes nanotubes, nanowires (length greater than the width). Small aspect ratio includes spherical, oval, cubic NPs (the aspect ratio is generally close to one). NPs can be dispersed in various suspensions, aerosols and possess different agglomeration states. The components, agglomeration states, size, shape play an important role in nanoparticle reactivity. This provides a lot of applications in composite materials (several components), electronics, chemical and biomedical sectors. To name a few, carbon nanotubes can improve the structural properties of composite materials. Quantum dots are semiconductor material, and possess remarkable optical and electronic properties. Illuminated by ultraviolet, these nanocrystals emit light whose wavelength depends on the composition and the particle size. Due to their simple synthesis, the wavelength can be easily tuned². These materials can be used as luminescent markers in biological systems. Gold and silver metal NPs possess delocalized electrons on surface. Surface plasmon (SP) is the collective oscillations of conduction electrons excited by electromagnetic radiation at the metal-dielectric interface. The result of this collective oscillation is a strong light scattering, the surface plasmon absorption bands depends on the near field in the immediate vicinity of the particle surface. Plasmonic architectures enable surface-enhanced spectroscopies based on plasmon effect³. Gold NPs are used in SPR (surface plasmon resonance) devices, based on surface plasmon resonance. SPR spectroscopy is a surface sensitive

technique, used to detect refractive index changes. This technique is applied to immunoassays. Silver, gold NPs are also used for enhancing Raman signals, this is the surface-enhanced Raman Scattering (SERS). SERS is a spectroscopy based on the Raman effect and can provide a signal enhancements of up to 10^{14} over normal Raman. This technique can provide detection in the order of 0.1ppm. Superparamagnetic iron oxide NPs (SPIONs) offer many applications in medicine⁴. SPIONs are used to improve contrast in magnetic resonance imaging, heat source in magnetic fluid (with cell tracking to destroy the tumor), drug delivery and ultra-sensitive diagnostic assays. Metal oxide NPs possess many properties such as: magnetic⁵, photocatalytic⁶ and tunable optical properties⁷. Metal oxides NPs are finding increasing nanotechnology applications. To name a few: titanium dioxide (TiO_2), zinc oxide (ZnO), magnesium oxide (MgO), copper oxide (CuO), aluminium oxide (Al_2O_3), manganese oxide (MnO_2) and iron oxide (Fe_3O_4 , Fe_2O_3). These materials are used as pigments in paints (TiO_2), sunscreens and cosmetics (TiO_2 , ZnO), antimicrobial agents⁸ (MgO , CuO), industrial operations such as coating for solar cell or pigment (Al_2O_3 , MnO_2) and for medical purposes⁹ (Al_2O_3 , Fe_3O_4 , and Fe_2O_3). In recent years progress have been made in the preparation, modification, and applications of titanium dioxide (TiO_2) NPs, using for photocatalysts, ultraviolet protection and photovoltaic devices, to these reasons we focus on TiO_2 nano-particles.

B. Titanium dioxide NPs

Due to their stability and physical properties, TiO_2 particles are used in food industry, cosmetic industry, and personal care products. There are two kinds of TiO_2 particles: pigmentary TiO_2 (size range: 250 to 350nm) and nano- TiO_2 (under 250nm). TiO_2 is used in sunscreens (or similar cosmetics), toothpaste, pigments, clothing or food¹⁰. The global production in US of TiO_2 particles is estimated at 4 million metric tons per year. Most part of the production (70%) is used as a pigment in paints (because of its brightness, high refractive index, and resistance to discoloration). In 2010 the production in US of nano- TiO_2 was estimated to 5000 t, and it is expected that this number continues to increase in the coming years. Personal care products such as sunscreens or toothpaste contained 1%-10% titanium in weight. Young people are the most exposed to TiO_2 consumption, due to a large presence of TiO_2 in candies (greater than $1\mu\text{g}\cdot\text{mg}^{-1}$)¹¹. In the US, exposure of Nano- TiO_2 is estimated at 0.1mg TiO_2 /person/day.

a. Physical properties of titanium dioxide (TiO_2) NPs

The properties of TiO_2 NPs are exploited in various domains such as energy and environmental domain¹² (photovoltaics, photocatalysis, photo-electrochromics and sensors).

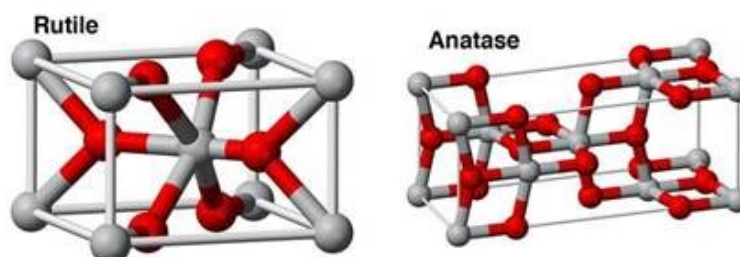


Figure 1.2: Lattice structures of the three crystalline phases of TiO_2 rutile, anatase.

Figure 2 shows the unit cell structures of rutile and anatase. These two structures can be described by a chain of TiO_6 octahedra. Ti^{4+} is surrounded by an octahedron of six O^{2-} . The difference between these two crystal structures is the distortion of each octahedron and the assembly pattern of the octahedra. In rutile structure, each octahedron is in contact with 10 neighbours octahedra, while in the anatase structure, each octahedron is in contact with 8 neighbour. These differences in lattice structures cause different mass densities and electronic properties between the two forms of TiO_2 . Rutile is the thermodynamically stable form of TiO_2 , at high temperatures and normal pressure. Small NPs (< 50nm) anatase are more stable, and transformed to rutile at $T > 373\text{K}$ ¹³. The theoretical density of TiO_2 ranges from 3895 kg/m^3 for anatase, to 4250 kg/m^3 for rutile. The refractive indexes of rutile and anatase are approximately 2.75 and 2.54, respectively¹⁰. TiO_2 is a semiconductor, with a gap of 3.0 eV for the bulk rutile phase, and 3.2 eV for the anatase one. This induces an absorption in UV range (< 400nm or 3.2 eV). For NPs, the band gap energy increases with decreasing size. TiO_2 NPs have photocatalytic properties, especially anatase mineral form and crystallites smaller than 20nm. TiO_2 NPs absorb light from low energy photon $h\nu < E_g + W_c$ (E_g is vibrational mode and W_c is the conduction band width). Electrons are excited from the valence band to the conduction band (Figure 3). This leads to excited electrons in the conduction band, and positive holes in valence band. There are two possibilities: either these charges can be recombined, or theses charges react with electron donors or acceptors on the surface of the NPs.

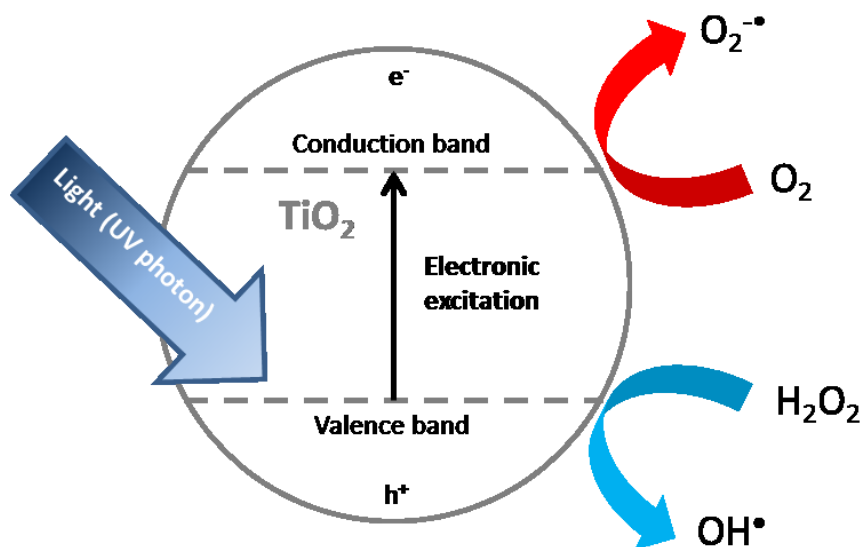
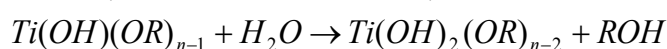
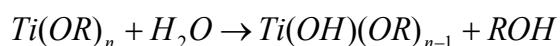


Figure 1.3: Scheme of photon-induced effect of TiO₂ Nanomaterials. In red: reduction of oxygen molecules by one electron, in blue: production of OH[•] by one electron oxidation of water molecules.

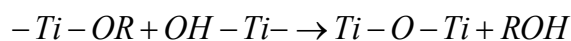
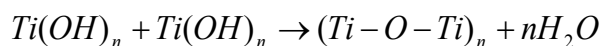
b. TiO₂ synthesis routes

Physical properties of TiO₂ NPs depend of the size, shape, chemical functionalization and the crystalline state of TiO₂ NPs. These parameters can be tuned by the way of synthesis. There is a number of synthetic routes for the preparation of TiO₂ NPs in solution¹⁴:

Sol Gel method is known as a versatile method in aqueous solvent¹⁵. TiO₂ is formed by hydrolysis and polycondensation of titanium alkoxide precursor¹⁶. During the process M–OH–M or M–O–M bonds are established between the metallic atoms M of the precursor molecules.



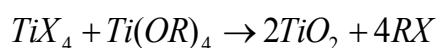
The reaction continues until the species Ti(OH)_n is formed, then the reaction continues with the polycondensation reactions:



The size and shape can be tuned by addition of surfactant¹⁷ such as amine, or long chain carboxylic acid, pH¹⁸ and temperature variation. Heat treatment is necessary to attain high crystallinity. Sol gel is used in spin coating and leads to highly porous materials. S. Mugundan et al¹⁶, synthesized Co-doped TiO₂ NPs at room temperature with heat treatment at 500 and 800°C for getting anatase and rutile phases, respectively. Jin Joo et al¹⁹, synthesized TiO₂ nano-rods with dimensions of 3.4 nm by 38 nm possessing a single crystalline anatase phase and a high photocatalytic activity.

Micelle and inverse micelle methods use aqueous and non-aqueous solvent²⁰. TiO₂ is formed by self-organization of surfactants and titanium alkoxide precursor. Shape is tuned by varying concentration between water and surfactant, or water and Ti precursor. The obtained material is often calcined to achieve crystallization²¹.

Sol method is a non-hydrolytic method²² taking place in solvent such as alcohols or ethers. The polycondensation between titanium chloride precursors and an oxygen donor (such as an organic ether) leads to the Ti-O-Ti bridge formation by the following reaction schemes (where R is the carboxylic chain of the metal alkoxide):

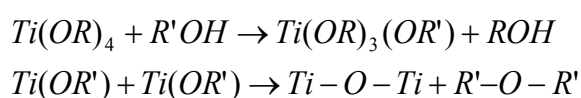


During the condensation reaction organic fragments are eliminated. Different surfactants such as acetylacetone or acetic acid can be used to control size distribution. The size, shape, crystalline state of formed NPs is highly controlled²³. Non-hydrolytic methods lead to better control and homogeneity than hydrolytic methods, which might be due to a better regulation of the polycondensation reaction rates.

Hydrothermal and solvothermal methods are based on a hydrolysis reaction. These methods are all one step procedures.

Hydrothermal method uses water as solvent²⁴. Titanium butoxyde and ammonium hydroxide are usually used as precursor and surfactant respectively. The size of synthesized NPs can be tuned by the pressure in the steel autoclave and the precursor²⁵. Hydrothermal method leads to small particles by precipitation (7nm).

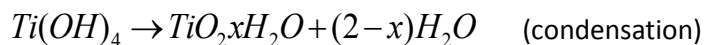
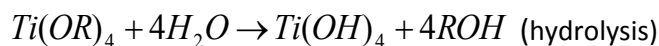
Solvothermal method uses non aqueous solvent (solvent with high boiling point). This method requires, or not, the use of surfactants. Nanoparticle characteristics can be tuned by temperature and by adding surfactant. This method leads to NPs with controlled size, shape²⁶, crystallinity²⁷ and reactivity^{28,29}. One of the most important parameters is the concentration ratio between products and surfactant²⁶. This influences the solubility, reactivity, diffusion of reagents and final crystallization. NPs are generated by the following reaction scheme (where R is the carboxylic chain of the metal alkoxide and R' the carboxylic chain of the alcohol):



Xiao-Lin et al²⁷., synthesized monodisperse TiO₂ nanocrystallites with various shapes by a non-hydrolytic condensation reaction with the Ti precursors Ti(O-C₄H₉)

The reaction of etherification of acid will generate H₂O for the hydrolysis and condensation reactions. The chain lengths of the carboxylic acids had a great influence on the formation of TiO₂. In the

presence of water, the Ti-O-Ti network is generated by the following reaction scheme (where R is the carboxylic chain of the metal alkoxide):



The low dielectric constant organic solvents used in the solvothermal method leads to a decrease in the solubility of TiO₂, which results in limited dehydration and the formation of smaller NPs, giving rise to better crystallinity of TiO₂. Cao-thang Dinh et al³⁰, synthesized TiO₂ nanocrystals with different shapes using water vapor as the hydrolysis agent to accelerate the reaction by solvothermal method. The table 1 gives an overview of advantage and inconvenient of each method.

Method	Advantages	Disadvantages	Reference
Sol Gel	Simple, cost effective and low temperature synthesis procedure	Drying and annealing are needed to obtain crystalized particles	15,16
Micelle and micelle inverse	Nano TiO ₂ products have high dispersion and uniform nanosizes. Moreover the surface modification through choosing different surfactants allows to synthesis inorganic nanosize functional materials.	Calcination is usually needed to achieve crystallization	20,21
Sol method	The size, shape, crystalline state of forming NPs are highly controlled	Slight changes in experimental conditions may result in altered particle size and morphology, hindering the reproducibility of the protocol	22,23
Hydrothermal	Heterogeneous chemical reaction, one step procedure. The synthesized nano TiO ₂ possesses high	Limited by the boiling point of water (T < 100°C)	24,25

	purity, crystal symmetry, and narrow particle size distributions.		
solvothermal	Same advantage as hydrothermal method, the temperature and pressure can be much higher than hydrothermal method.	Long time of synthesis	^{27,30}

Table 1.1: advantage and inconvenient of synthesis routes

Comparing different synthesis routes of nano TiO₂, better size-control nano-particles with higher crystallization and less agglomeration are obtained by the solvothermal method. For these reasons, solvothermal is the used method in this work.

c. Current understandings of TiO₂ NPs nanotoxicity

Nanotoxicology is a branch of toxicology which addresses the adverse health effects caused by nanoscale objects. In this case the nanoscale objects are the NPs, and the nanotoxicity is the possible toxic effects of these NPs. Due to the utilization of TiO₂ nanoparticle, in a large variety of products, TiO₂ NPs may be absorbed by the skin, pulmonary system or the gastrointestinal system as shown on figure 4. TiO₂ can be distributed in various organs such as liver, kidneys, spleen, or even brain causing localized effects³¹.

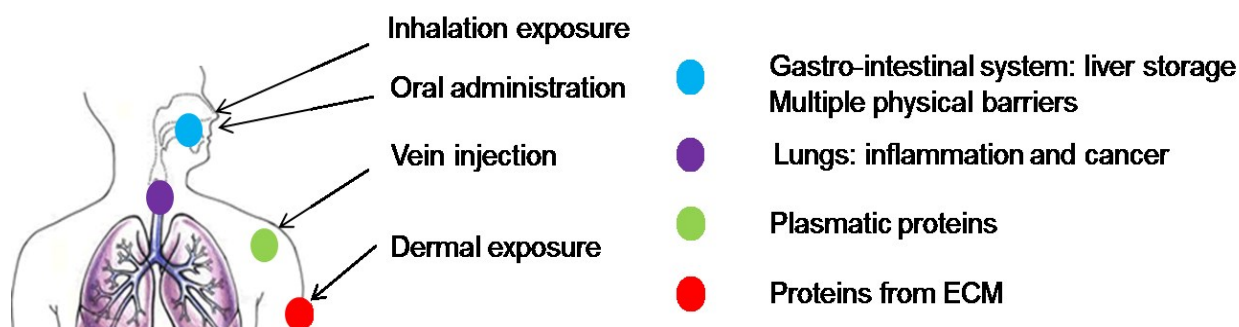


Figure 1.4: Schematics of human body with pathways of exposure to NPs and focalized interactions

Pulmonary inflammatory and lung cancers are the most frequent consequences observed in experimental animals due to TiO_2 nanoparticle exposures³¹. The toxicity depends on the surface area of NPs and their reactivity, which itself depends on the size, shape, chemical functionalization and electrical properties of TiO_2 NPs³³. Toxicity mechanisms are various: oxidative stress, damage to cell membrane integrity, genetic disruption and release of heavy metal^{34,35}. TiO_2 produces reactive oxygen species³⁶ (ROS) which may generate oxidant stress. The crystal size of TiO_2 NPs has large influence on $\cdot\text{OH}$ generation³⁷. ROS can be generated by Fenton-type reactions in the presence of molecule generating free radicals, or by the capacity to TiO_2 NPs to produce reactive oxygen under ultraviolet (UVB: 290-320 nm and UVA: 320-400 nm). The generated ROS or other radicals can modify the structure and function of the protein. Moreover the production of ROS can have detrimental effects on the genome, and induce oxidative DNA damage³⁸. The cell membrane is a semipermeable barrier. This barrier serves important cellular function (intercellular communication and regulation of material transport). As shown on figure 5 some NPs can interact with the cell surface and compromise the biological function. The NPs surface creates a region of highly concentrated ligands, which alters cell signaling³⁹.

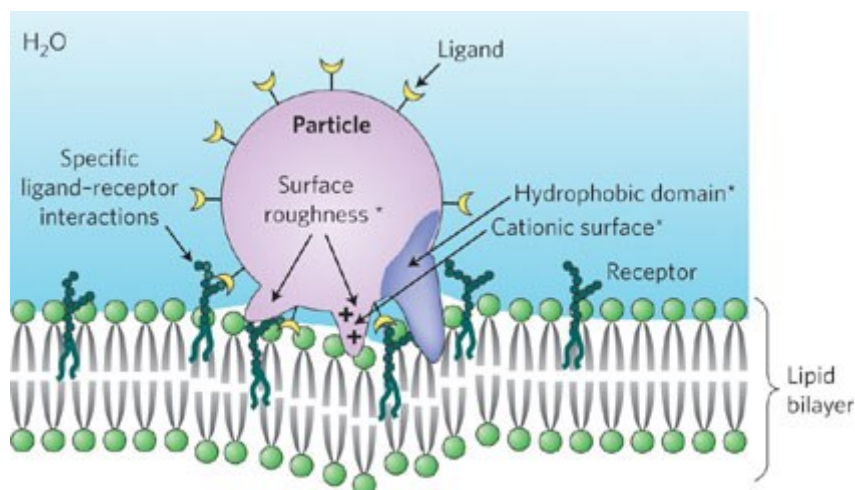


Figure 1.5: Nanoparticle-cell interaction with the different factors that can influence the interaction adapted with the permission from reference⁴⁰

NPs penetrate into the cell after binding to the receptor target on the membrane, and release heavy metal. NPs-proteins complex less than 100nm diameter can penetrate into the cell, while NPs less than 40nm can enter into the cell nucleus. The ways of internalization by the cell are various:

Large sized NPs (such as agglomerate NPs or nanoparticle-protein complexes) are ingested by macrophage via phagocytosis, consisting in a covering by the plasma membrane over the NPs to form a phagosome. NPs may also internalize via micropinocytosis which involves ruffling of the plasma membrane to form vesicles, when this internalization is directed by specific receptor thus involving the formation of caveosome or clathrin coated vesicle. The uptake pathway is a key parameter for nanoparticle intracellular applications. For example the contents in endosome is recycled back to the extracellular environment and degraded in acidic lysosomes (leading to a reduction efficiency of drugs^{41,42}). Mechanisms such as micropinocytosis are known to avoid the lysosomal degradation processes⁴³.

The difference in size, shape and crystalline phase between the used NPs gives conflicting results. For example, one study showed that DNA adduct formation in rat lungs was not detected following chronic inhalation for two years to TiO₂ NPs (10.4 mg/m³)⁴⁴, on the other hand, another study showed TiO₂ NPs (100mg/kg) increased the mutation of alveolar cells⁴⁵.

d. Nanoparticle design

One of the major difficulties in the efficiency of drugs is to target the concerned organs^{46,47} or cells without deteriorating or degrading the drug⁴⁸. The use of NPs can partially solve this problem by controlling the size, charge and surface functionalization of NPs. These parameters determine the physiological response and the targeted organs. The size of NPs plays important roles in physiological

barrier selection and mobility⁴⁹. For example in certain organs such as liver, the pore size, up to 100 nm, allows easier passage of larger particles, while in the blood brain barrier is closed up to 10nm. The charge and surface functionalization play an important role in half-life (time for the concentration in blood plasma of NPs to reach one-half of the original value). The pharmaceutical applications go from targeted drug delivery to biomedical imaging, or theranostic abilities⁵⁰. The evolution of nanoparticle design for biomedical application has evolved with the understanding of biological responses. The half-life ($t_{1/2}$) circulation in blood of NPs is a result of the interactions of NPs with serum proteins⁵¹. Proteins instantaneously bind onto the nanoparticle surface and dictate the half-lives, this is the corona phenomena. The size, shape and surface charge of nanoparticle dictate the behavior in blood. For example F.Rooli et al., has showed the influence of size and surface charge⁵², larger SPIOs have shorter blood half-lives than smaller (49min to 20nm SPIOs and 5min to 50nm SPIOs), and for the same size but different zeta potential, PEG-SPIOs have bigger blood half-lives than CDX-SPIOs (28min for -20mV and 5min for -30mV respectively). The administration of therapeutic agents has been limited by multiple factors: low solubility, stability and rapid clearance of NPs. These problems have led to the development of various targeting strategies, NPs in medical diagnostics and treatment are divided into three categories⁵³ as shown on figure 6 (1st categories: un-functionalized NPs, 2nd categories: functionalized NPs, 3rd categories: functionalized NPs and environment responsive). The first category is characterized by the ability to combine molecules of interest with basic surface chemistries, and allows to determine the effect of surface charge⁵⁴, and investigate the toxicity and cell interaction⁵⁵. NPs of the first category are easily captured by phagocytic cells of the reticuloendothelial system. The second category introduced the concept of stealth and active targeting on tumor cell. The goal of stealth is to escape from the vigilance of the immune system to avoid opsonization and thus phagocytosis of NPs. These NPs are coated with hydrophilic polymer chains, from neutral polyethylene glycol (PEG). PEG constitutes a steric hindrance preventing the opsonin fixation (serum proteins, complement, antibodies ...), making NPs undetectable by macrophages⁵¹. Gref et al⁵⁶, have showed that the amount of proteins absorbed on PLA-PEG 5 kDa was substantially reduced (~80%) compared to the amount of non-pegylated PLA NPs. The chain length and surface density affect the nanoparticle stability⁵⁷. Active targeting refers to the enhanced permeation and retention effect (EPR) of tumor cell. Unfortunately, the excess of targeting ligands increased the clearance by the phagocyte system. Secondly, the barrier effect of the liver retains most part of NPs. The last category incorporates the concept of dynamic environment responsive. Tumor cell environment is characterized by low pH⁵⁸ and low concentration of O₂. NPs of the third category are functionalized to release drugs at low pH, or degrade the nanoparticle in order

to release drugs inside the local tumor environment. The understanding of corona phenomenon is the key point to improve the use of NPs in biomedical domain, especially avoid protein adsorption.

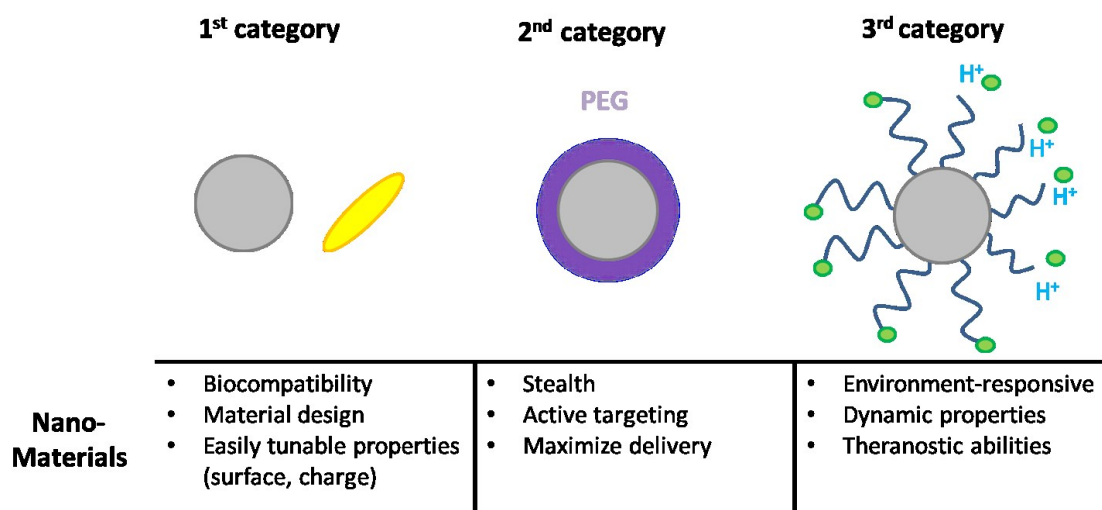


Figure 1.6: Evolution of nanoparticle design in nano-bio technology.

III. Protein adsorption

A. Generalities

Cells are fundamental units of living organisms, whose genetic information is located inside the nucleus (DNA). The genes contained in the DNA sequence can be transcribed to make a molecule called mRNA. Proteins result from a process called translation using the mRNA as a template, and are formed to address cell needs. Proteins are copolymers of L-amino acids which are linked to each other to form a polypeptide chain. There are 20 different amino acids. An amino acid is composed of an amino group ($-NH_2$), a carboxyl acid group ($-COOH$), and a side group ($-R$). The polypeptide chain varies in size, shape, charge and hydrogen bonding capacity. Side-chains also vary in polarity, hydrophobicity. The protein primary structure is the sequence of amino acids in the polypeptide chain, it also implies the location of disulfide bridges. The primary structure determines the spatial organization of the protein molecule. The secondary structure is responsible of the flexibility in the chain. Two famous secondary structures are the α -helix and the β -sheet, both being held together by hydrogen bonds and twist. Another important secondary structure is the random coils and β -sheet. And tertiary structure is the overall topology of the polypeptide chain. This is the three-dimensional arrangement of the secondary structure, corresponding to a global minimum energy. The quaternary structure is composed by several tertiary structures bound together.

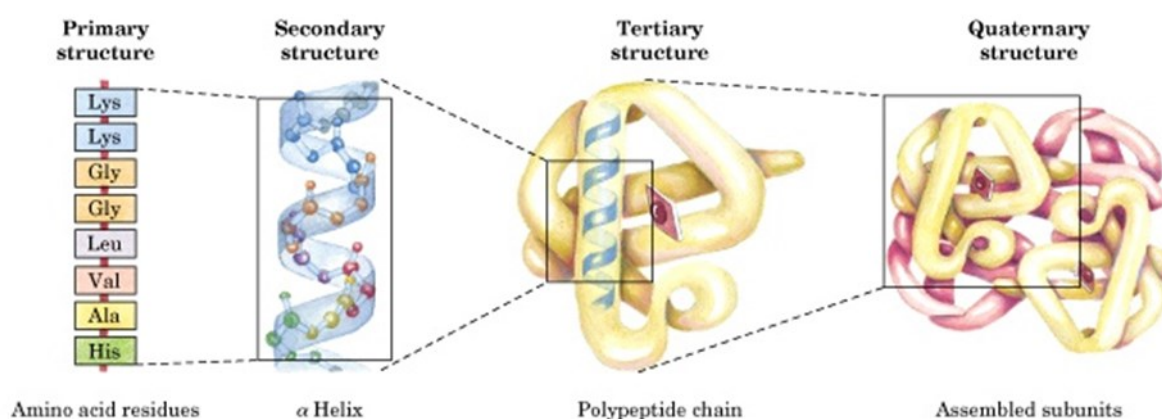


Figure 1.7: Representation of different levels of protein structure. (From: Nelson, D.L. and Cox, M.M., *Lehninger principles of biochemistry* 2005, New York: W.H. Freeman)

B. Protein adsorption on flat surface

When a solid material is in contact with a biological medium it becomes quickly recovered by a proteins layer⁵⁹. The adsorption process consists in two steps: (i) first proteins with high affinity with the materials are adsorbed, (ii) second other biological materials are adsorbed such as cells and other

proteins. The first step is in general irreversible and leads to conformational change of proteins. The adsorption mechanism is complex, depending on the properties of proteins, the surface (hydrophobicity, nano structuration, chemical functionalization...) and the surrounding medium (ionic strength, pH, solvent and temperature).

The adsorption process can be divided into three steps. The first step is the transport of molecules from the liquid near to the surface (convective and the diffusion effect). Far from the surface, the convective motion dominates. Near the surface (10 μm) diffusion takes over. In second, even closer the surface the interfacial force becomes more important. The force with the longest range is the solvation force, which governs the reorganization of water to form a ramified hydrogen bond network in liquid. It has a characteristic length of about 1nm, depending on solvent polarization. Last, the electrostatic force is important. Due to the ions present in the solution, the electrostatic force has a characteristic length (Debye length), also about 1 nm. The reorganization of charges favors the interaction between protein and surface. The Van der Waals interaction is even a shorter range one, but is also important in the protein surface interaction.

a. Driving forces

Protein adsorption is spontaneous if the Gibbs free energy of the system decreases⁵⁸: $\Delta_{ads}G = \Delta_{ads}H - T\Delta_{ads}S < 0$. Where H is the enthalpy and S entropy of the system and Δ_{ads} is the operator. On the one hand, the adsorption is generally an exothermic process, as it originally tends to minimize the free enthalpy of the system, owing to unbalanced forces at the interface. On the other hand, the reduction of molecule mobility (adsorption on the surface) leads to a decrease of the system entropy. This illustrates the compensation between $\Delta_{ads}H$ and $T\Delta_{ads}S$ terms in the adsorption process. The interactions involved in the driving force of short peptide adsorption can be summarized but not limited to : Electrostatic interaction between electric double layer of metal and oxide surfaces and charged groups of peptide molecules, interaction of van der Waals (London) forces and interaction of solvation forces (positive contribution in ΔS).

b. Hydrophobic interaction

The hydrophobic or hydrophilic character of the surface has been characterized as a key parameter for the protein adsorption process, it is generally accepted that hydrophobic surfaces adsorb more proteins than hydrophilic surfaces. The hydrophobic surface allows interaction with hydrophobic domains and residues in the protein; the process is assisted by an entropy gain during the release water at the surface.

c. Change of hydration state and reorganization of electric charges

Proteins possess polar and non-polar groups, thus, in an aqueous environment proteins are surrounded by counter ions (Stern layer). When proteins approach the surface, the electrical layer interacts, resulting in ion redistribution. The adsorbed proteins form a compact layer where the density of charge is neutral (compensation of surface charges). Surface is covered by water molecules, which when proteins approach reorganize. This change of hydration state, leads to an entropy gain by the release of water molecules in solution⁶¹ (figure 8). Water molecules, interacting with ions in solution (electrostatic interaction), may lead to conformational changes of proteins. The protein can expose a non-polar group to the surface during the adsorption, leads to a change in the secondary structure and a decrease in Gibbs free energy.

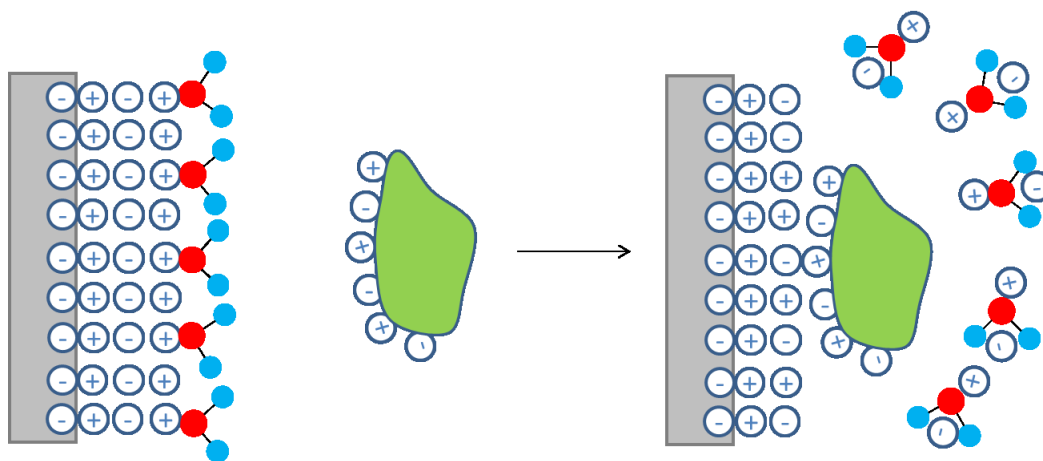


Figure 1.8: Schematic representation of the change of hydration state to an interaction between negative charged surface and proteins. Ions in solution are represented by negative and positive charges.

d. Impact of protein structures

Protein can be described in terms of “hard” and “soft” proteins⁶² (figure 9). Hard proteins possess stable structure (high internal cohesion) and retain their native conformation after adsorption. They adsorb on hydrophobic interfaces under all conditions of charge interaction, and on hydrophilic surfaces only if electrostatically attracted. Examples include α -chymotrypsinogen, ribonuclease, cytochrome-c, lysozyme and β -lactoglobulin. Soft proteins lose their conformation more easily, due weakness internal cohesion, the conformation changes after adsorption and lead to an entropy gain. This structural rearrangement allows adsorption in repulsive electrostatic condition and on hydrophilic and hydrophobic surface, to cite a few: BSA, HSA, immunoglobulin, α -lactalbumin, β -casein and haemoglobin.

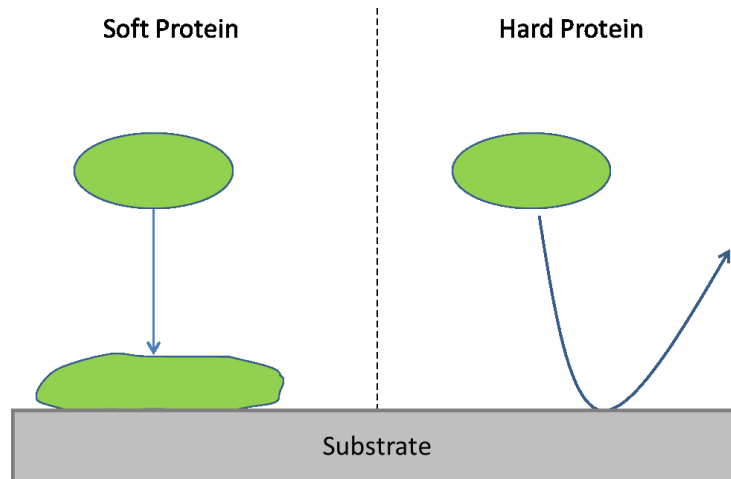


Figure 1.9: Schematic representation of interaction between a hydrophilic surface and a protein.

e. Solution parameters

Experimental conditions, pH, ionic strength, temperature and protein concentration play an important role on protein adsorption.

1. pH and Ionic strength

pH and ionic strength determine the electrostatic state of the protein. In a general manner, if protein and surface are electrostatically neutral, the adsorption is decreased (no surface charge interaction). If pH is equal to pI (isoelectric point is the pH at which a protein is not electrically charged) the protein will be electrically neutral, in this case protein-protein interaction will be governed by steric repulsions (means a maximal repulsion between proteins). But if the pH is different from pI, protein will be positively or negatively charged. In this case, adsorption can occur by electrostatic attraction. For example it has been established that at pH 3.5, fibrinogen (pI= 5.5) adsorption on mica (zeta potential: -66mV) is irreversible for ionic strength varying between 3×10^{-4} (low value) and 0.15 M (high value), and for pH 7.4 a partial desorption of fibrinogen was observed for ionic strength below 10^{-2} M⁶³ (zeta potential of mica: -71mV). Ionic strength can regulate the electrical potential of proteins (by surface charge compensation), and impact on the repulsion between proteins which govern the density of population on the surface (table 2). The equilibrium between pH and ionic strength is an important parameter. For example hemoglobin has a pI of 6.7 for a different value of pH the adsorption on hydrophobic surface decrease, moreover for a high value of ionic strength (200mM KCl) a formation of a single monolayer is observed⁶⁴.

pH vs pI	Ionic strength (I)	Effect on surface coverage
pH=pI	High I value	Monolayer
pH=pI	Low I value	High coverage
pH<<pI or pH>>pI	No impact	Low coverage

Table 1.2: Effect of pH and ionic strength on surface coverage.

2. Temperature

Temperature plays a key role on protein adsorption. Protein adsorption is generally higher at high temperature, due to denaturation of protein. Structural rearrangement increases the amount of hydrophobic contacts between the protein and the surface. For example, adsorption of BSA (globular protein) in a temperature range of 20 from to 40C° increases with an increase in temperature (for pH 4 and 5) due to the increase of diffusion on adsorbent surfaces with increasing activity of protein⁶⁵. However, this is not always valid, for example, native collagen (fibrillary protein) is known to be weakly surface active, a study has proved that increasing the temperature during adsorption helps to reduce surface tension due to a partial denaturation, and reduces protein adsorption⁶⁶.

3. Concentration of proteins

The coverage of the surface depends on protein concentration. For example, at high concentration (>0.5mg mL⁻¹) albumin formed a first saturated monolayer onto hydrophobic surfaces⁶⁷. In the case of multistage adsorption additional proteins tend to adsorb on the first layer, and form multilayers. The formation of these multilayers is governed by protein-protein interactions. These interactions may be ionic, covalent, hydrophilic or hydrophobic. At a low protein concentration (~40ug mL⁻¹), protein can more easily maximize the interaction with the surface by denaturation and irreversible adsorption of the protein at the surface. For example, Vörös et al., showed that the highest coverage is observed at the higher concentration, lower at the lower concentration for HSA on TiO₂ surface, but at low protein concentrations denatured proteins show the highest adsorption⁶⁸. In general, small proteins adsorb more than large proteins (small protein is more compact). This leads to a higher mass surface density for small proteins at high concentration (figure 10). At high concentration a multistage process can occur. P, Roach et al., showed a rearrangement or orientation change for fibrinogen due to protein-protein interactions, driven by increased hydrophobic interactions between adsorbed molecules⁶⁷.

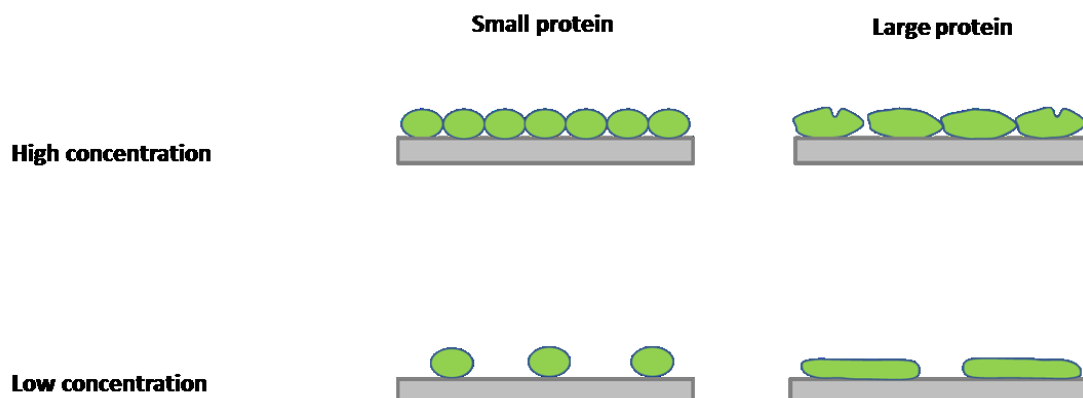


Figure 1.10: Schematic representation of protein monolayer to show difference between high and low concentration on protein adsorption on flat surface. “soft” proteins are more denatured at low concentration.

f. Protein adsorption on flat surface

Protein adsorption can be described in several steps. First step: transport of proteins from the solution to the surface. Second step: initial adsorption of protein, and conformational changes of protein on the surface. In the case of a mixture of proteins, the proteins with the highest concentration will dominate the adsorption in the first time. Then, these proteins will be replaced by proteins with higher affinity to the surface. The surface property play an important role on adsorption proteins^{69,70,71}. The denaturation process is generally more important on a hydrophobic surface than on a hydrophilic surface. This is due to the hydrophobic interaction, between hydrophobic residues of proteins and the surface. The last step is the possible detachment of adsorbed proteins from the surface and their re-attachment, this process of denaturation may lead to a loss of biological functions.

C. Protein adsorption on nano-structured surface

The nanoscale surface topography (dimensions less than 100nm) has an effect on protein adsorption. It is important to control and understand the physicochemical interaction between nano-structured surfaces and proteins for biomedical applications such as: regenerative medicine, tissue engineering, biomedical implants and biosensors. The adsorption depends on the surface roughness, surface chemistry and concentration of adsorbed proteins. At the nanoscale, it has been reported that the surface roughness impacts the wettability⁵⁹. This leads to a local change in surface chemistry and a restricted access to proteins, it's also induces different degrees of geometrical packing of the proteins. K. Rechendorff et al., found that for fibrinogen adsorption on tantalum samples, the saturation increases by about 70% when the roughness increases from 2.0 to 32.9 nm (increase of

surface area $\sim 20\%$), whereas the increase of BSA adsorption is closer to the increase of surface area⁷² (meaning that BSA adsorption is proportional to the surface increasing). This effect is due to a different configuration of proteins during adsorption. Therefore, the relationship between nano-structured surface and protein adsorption is not simple. For example, on one hand, Cai et al., found that the amount of fibrinogen adsorbed onto oxidized titanium, rough at the nanoscale is not altered compared to flat titanium surface when corrected for the increase in surface area created by the surface topography⁷³. On the other hand, M.S. Lord et al., found that the amount of fibrinogen is altered by various surface roughnesses, using colloidal silica particles adsorbed onto a polycationic polymer⁷⁴. Less fibrinogen is adsorbed on the 11 nm nano-rough surfaces compared to the less rough surfaces (7 and 8 nm) and on the flat model control surfaces (corresponds to the same surface without nano-rough). The influence of the structure is specific to each protein. It is established that the effect of surface curvature plays an important role on protein adsorption. When the protein is about the same size as the surface curvature the latter is not altered. When the difference between proteins size and the size of surface curvature is too important, the protein is denatured (figure 11). P Roach et al., showed that albumin and fibrinogen have different interactions due to their differing shapes. Albumin is stabilized by high surface curvature, while, fibrinogen, is distorted by wrapping around surface curvature, inducing secondary structure loss⁷⁵.

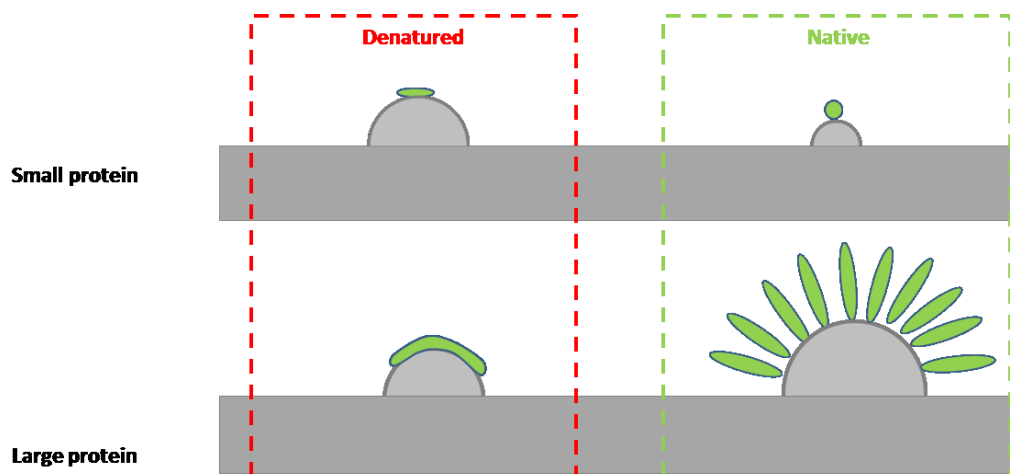


Figure 1.11: Schematic to show the impact of size difference, between nanostructured surface and protein. Inspired by P Roach et al⁷⁵

IV. Protein corona phenomenon

Understanding the physiological response of nanoparticle is a fundamental challenge of nanomedicine. The question is “what does cells see?”. When a nanoparticle is placed in a biological fluid, it becomes quickly recovered by a layer of proteins: it’s the protein corona^{76,39}. As we saw before the nanoscale has an effect on protein adsorption. At the nano-scale the physical properties have changed. NPs possess a high surface energy and high surface reactivity. The biological identity of corona determines the physiological response by mediating the interaction of the nanoparticle with biomolecules, membranes, and physical barriers. The corona can be described by the affinity binding, conformation, quantity and thickness of the adsorbed protein layer. The physicochemical properties of nanomaterials (size, shape, surface charge, and hydrophilicity/hydrophobicity) and the environmental factors (pH, ionic strength, and temperature) must be taken into account to explain corona formation.

A. NPs and colloidal stability

The corona is the result of the interaction between nanoparticle and proteins in solution. The behavior of NPs in solution is a key point to understand this interaction. NPs in solution present three different states: primary particles, aggregate particles and agglomerate particles. The colloid system is regulated by the equilibrium of colloidal forces, these colloidal forces are: Van der Waals, steric forces and the electrical double layer around the NPs.

a. Colloidal forces

Van der Waals (VdW) forces are weak attractive forces and only efficient at a very short distance (<3nm). VdW force is the attraction between two dipoles. For two spherical particles with the same radius r , and separated by a distance d , VdW attraction is given by the following equation:

$$V_a = \frac{Ar}{12d}$$

Equation 1.1: Where: V_a is the attractive potential energy, d the distance between particles, r the radius of particles and A the Hamaker constant.

The electrostatic force is associated with the surface charge and the electrical potential at the interface of NPs. The electric charge plays a role in colloidal stability, especially for charged NPs like oxides (such as titanium dioxide, iron oxide, quartz...). Electrostatic force depends on the solvent, ionic strength and pH. These parameters determine the agglomeration state of charged NPs. Two

important factors are the thickness of the electrical layer and the zeta potential. The ionic strength of solutions controls the thickness of the double electrical layer. In general, when ionic strength increase, the double electrical layer is diminished, this favors the aggregation. The pH controls the surface ionization. For extreme values of pH the zeta potential is increasing, this leads to a domination of the electric repulsive force. When two particles are far from each other, the electrostatic force is zero. When two particles approach each other, the repulsive force increases. For two equally sized spherical particles, the force can be described by the following equation:

$$V_r = 2\pi\epsilon r \zeta^2 e^{(-kd)}$$

Equation 1.2: Where: V_r is the repulsive potential energy, $\epsilon = \epsilon_0 \epsilon_r$ (ϵ_r is the dielectric constant of the solvent and ϵ_0 the permittivity of vacuum), r is the particle radius, π is the solvent permeability, K is a Debye-Hückel parameter, d the distance between particles and ζ is the zeta potential.

b. DLVO theory

The colloidal stability and agglomeration state of NPs can be explained by the DLVO (derjaguin–landau–verwey–overbeek) theory. DLVO theory is based on the electrostatic repulsion, steric repulsion and Van der Waals forces (VdW)⁷⁷. In the DLVO theory, the agglomeration state is determined by the sum of attractive and repulsive forces between particles. The total potential energy V_T is expressed as $V_T = V_A + V_R$. Figure 12 shows the total energy V_T resulting from the addition of VdW and electrostatic forces. At far distance, VdW potential and electrostatic potential are reduced to zero. When two particles are approaching each other, the curve passes through a maximum, which constitutes an energy barrier against particle agglomeration.

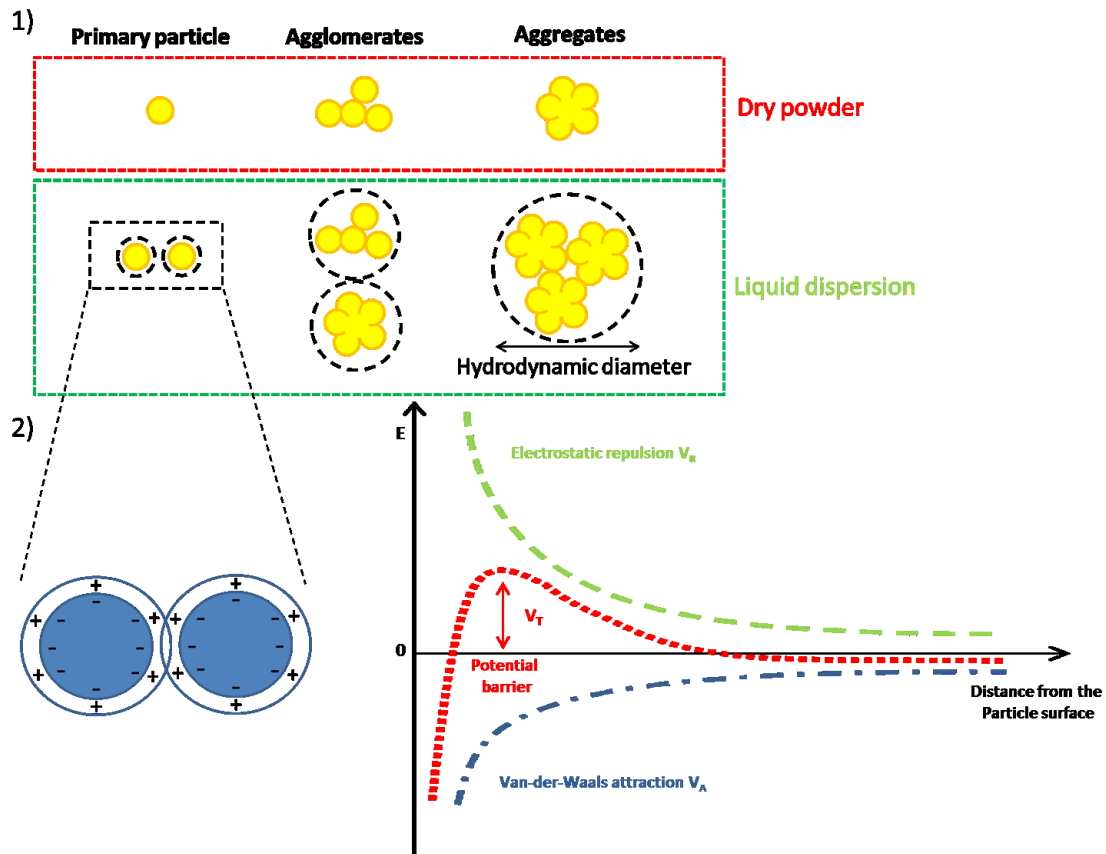


Figure 1.12: 1) Representation of the different state of NPs in colloidal solution. The hydrodynamic diameter increased with the degrees of aggregation. 2) Representation of the DLVO theory for two spherical NPs and the corresponding energy curve when the particles are approaching each other (V_T).

B. Mechanism of protein adsorption

Phenomenon such as interfacial rearrangement of water molecules, conformational changes of protein, and physiochemical properties of proteins are still applicable such as on a surface. On the other hand, the adsorption depends on the nano-scale characteristic of particles. Nanoparticle size, shape, curvature, surface charge, solubility and surface modification will highly impact the adsorption.

a. Size of nanoparticles

Due to the nano-scale effect of particle, protein adsorption is different on NPs and on flat surface or on nano-structured surface. The composition of protein corona can be different for the same kind of NPs but with different sizes. The difference in size between proteins and NPs seems decisive on protein adsorption. Conversely to expectation, for the same mass small particles with the higher specific surface area do not automatically bind more proteins than larger particles. The increase in surface curvature tends to lower the affinity of a protein to the nanoparticle. Presumably by

decreasing the area of interaction and decreasing the protein-protein interaction with the surface. Therefore, the role of curvature and nanoparticle size is not clear. Cedervall et al., studied the role of particle size and surface area on the protein adsorption on NIPAM/BAM (N-Isopropylacrylamide /N-tert-butyl acrylamide) (50:50) copolymer NPs. The nanoparticle size varied between 70 and 700 nm. In their case, the amount of bound proteins varied with size of NPs, and with the amount of available surface area, but the surface curvature no impacts the relative affinities of proteins for the particles⁷⁸. On another side, Silvia H et al., used gold NPs with a diameter range from 5 to 100 nm and showed that the protein binding depends on the nanoparticle size⁷⁹, the thickness of the adsorbed protein layer increases with nanoparticle size. For example, they observed that the thickness of protein layers increases from 10 to 50 nm with fibrinogen and HSA for an increasing of size of gold NPs from 20 to 100 nm.

b. Surface charge of nanoparticles

The hydrophobicity of nanoparticles affects the adsorbed protein. Hydrophobic or charged surfaces tend to adsorb more proteins and increase their denaturation. Cedervall et al., showed that increasing the negative charge density and hydrophobicity of polystyrene NPs increases protein adsorption from plasma⁸⁰ (a single layer of albumin is adsorbed onto the surface of the most hydrophobic particle, whereas a sparser layer is adsorbed onto the more hydrophilic particles). Increasing surface charge of nanoparticle may also influence protein adsorption. Gessner et al., showed proteins with isoelectric points (pI)<5.5 such as albumin will preferentially adsorb on positively charged NPs. While, proteins with pI>5.5 such as IgG will preferentially adsorb on negatively charged NPs⁸¹. Surface charge can also denature the adsorbed proteins. Zhou J deng et al., showed for oxide metal NPs such as ZnO or TiO₂, protein binding behavior was distinct for each type of nanoparticle (in despite of the fact that these NPs possess identical surface charge)⁸².

c. Physicochemical processes at the interface

The phenomena that may occur on the surface are numerous (figure 13). The physical parameters, such as functionalization by polymers, generation of ROS, release of metal determine what the protein sees and the interaction. As seen before, NPs for biomedical application are functionalized. The functionalization by polymers can prevent the adsorption by steric hindrance or favors the interaction with specific targets. The nature of polymer is not the only factor. With the same polymer with different Mw, the amount of adsorbed protein can change. K. Natte et al⁸³, Showed short chain reduces more significantly the amount of adsorbed protein than a long chain of the same polymer. Other physical properties such as ROS generation can change the conformation of protein, and

impact the adsorption. The agglomeration state of NPs in solution affected the protein binding, led to an increase in the amount and number of proteins bound to NPs⁸². Proteins can also increase the dissolution rates of particles of metal oxide by two mechanisms. Aqueous complexation (aqueous species complex free ions released by the materials surface), and ligand-enhanced dissolution (adsorbed protein extract metal atoms from the nanoparticle surface).

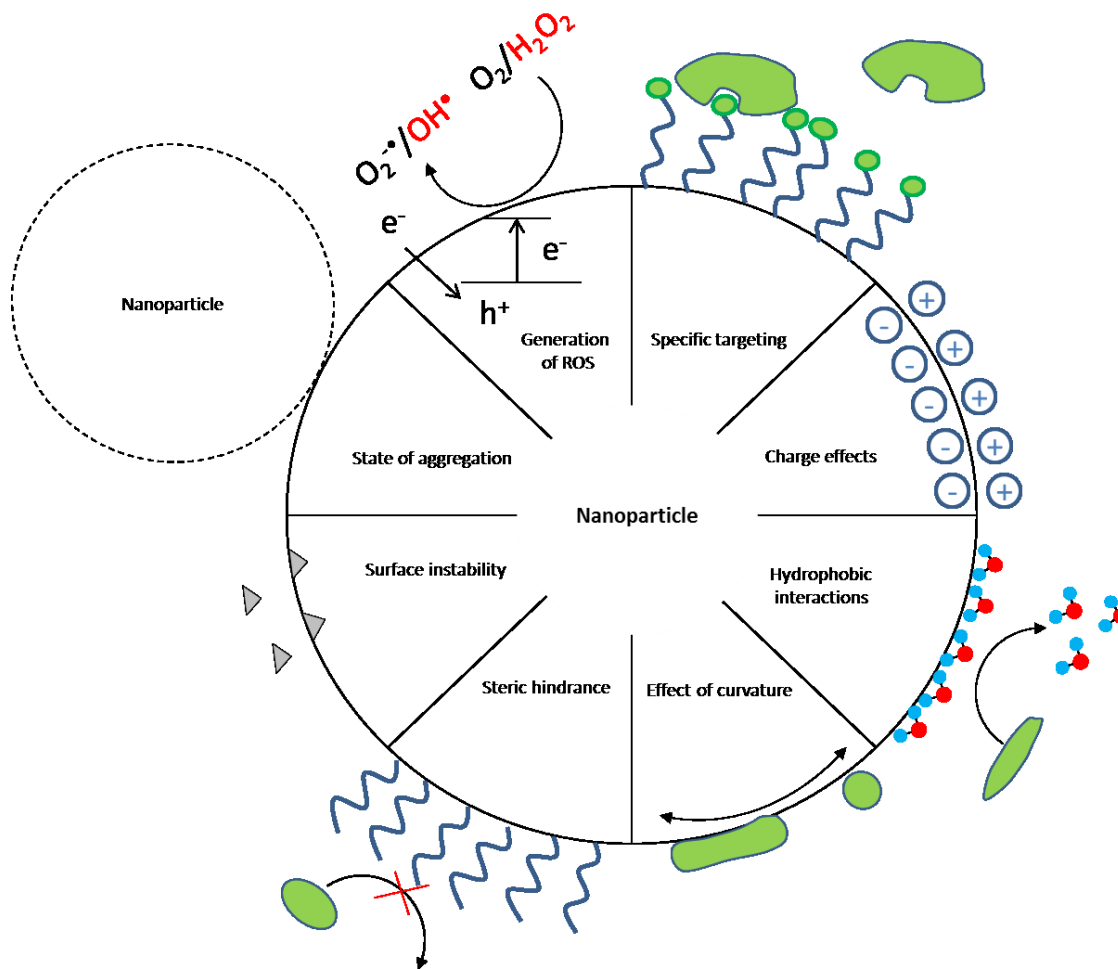


Figure 1.13: Schematic representation of some interaction/phenomena at the nanoparticle surface and possible effects on protein adsorption.

C. Kinetic of protein adsorption

Protein adsorption is a dynamic process, proteins are continually adsorbing and desorbing to the nanoparticle surface. The protein adsorption takes place in the very first time of contact between nanoparticle and biological medium, it is governed by protein–nanoparticle binding affinities, as well as protein–surface interactions. Proteins adsorbed with high affinity to the surface are known as “hard corona”. In general, it is an almost irreversible process, leading to protein conformation loss.

Proteins that adsorb with low affinity are known as “soft corona”; the difference between “hard” and “soft” corona is based on their exchange time⁸⁴ (kinetics of adsorption). The rate association and dissociation are described by “ k_{on} ” and “ k_{off} ” respectively. The value of k_{on} depends on the probability of adsorption events (the frequency of contact between the protein and the nanoparticle). k_{off} depends on the binding energy of the protein nanoparticle complex. The balance between k_{on} and k_{off} determines the strengths of protein nanoparticle interaction. Onto metal oxide NPs (TiO_2 , SiO_2 and ZnO), the equilibrium takes place in the first minutes of incubation⁸². During plasma protein adsorption to NIPAM/BAM copolymer NPs, a hard corona is formed in seconds, while a soft corona builds on a timescale of minutes to hours. Desorption shows similar timescale of 10 minutes for the soft corona, and 8 hours for the hard corona⁸⁴.

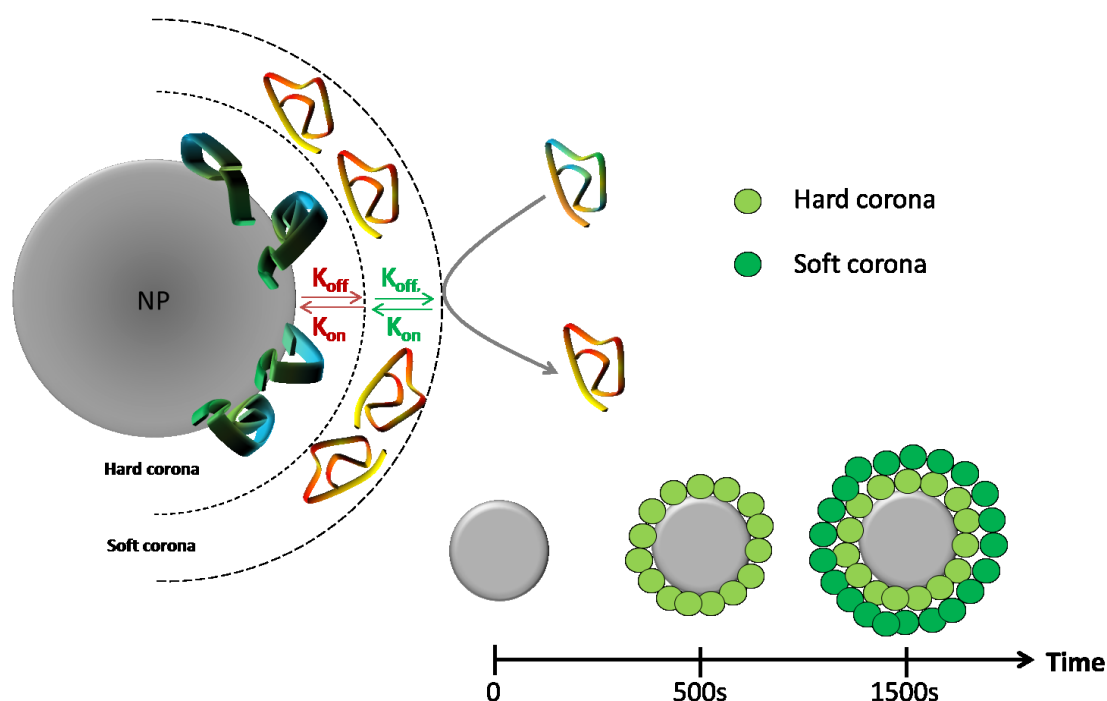


Figure 1.14: Schematic representation of formation of hard and soft corona and time dependence. Adsorption time are based on reference⁸⁴

The changes in the composition of the protein corona results from continuous adsorption and desorption of proteins, is called the ‘Vroman Effect’⁸⁵. The adsorbed proteins can change over time, but the total amount of adsorbed protein is constant at equilibrium. The proteins with the highest association rate adsorbs to the nanoparticle first. If these proteins have short residence times, they will be replaced by other proteins with slower association rates but longer residence times. Proteins such as fibrinogen are replaced in seconds, while protein adsorption such as albumin increases with incubation time⁸⁶.

D. Protein-NPs systems from the literature

The studies on protein-NPs interaction are multiple. Some focus on the effect of NPs size, surface charge, and functionalization on specific proteins and the possible denaturation of these proteins. Other deals with the identity and quantity of adsorbed plasmatic proteins on specific NPs and the thickness, association rate of protein layers and adsorbed proteins. Walkey et al⁸⁷, showed that a plasma protein corona consists of approximately 2–6 adsorbed proteins at high abundance and many others proteins with low abundance (representing a thickness between 20-40nm in the most cases of the corona). All these studies have in common the employed techniques to determine corona parameter: gel electrophoresis, liquid chromatography tandem mass of spectrometry (LC-MS/MS) are used to identify and quantify the adsorbed proteins. Dynamic light scattering (DLS), size exclusion chromatography (SEC), transmission electron microscopy (TEM) are used to determine the thickness of the corona. Size exclusion chromatography (SEC), surface plasmon resonance (SPR), isothermal titration calorimetry (ITC) are used to determine the affinity binding of proteins with NPs. And circular dichroism (CD), fluorescence quenching are used to determine the conformation of adsorbed proteins. Table 3 gives an overview of literature about this subject.

Proteins	Studied NPs	Technique used for protein-NPs interaction study	Study and topic
Transferrin	Polystyrene latex beads, sulfonated modified PSOSO ₃ H (100 nm), and carboxy modified PSCOOH (100 and 50 nm)	Fluorescence Correlation Spectroscopy(FCS)	Dynamics of the protein adsorption layer (hard and soft corona) ⁸⁸
plasma proteins	PEG-coated (160–270 nm)	2-D PAGE, DLS	Influence of PEG Mw, zeta potential and size on plasmatic protein adsorption ⁵⁶
Bovine serum albumin	PEG-coated with different monomeric units (7, 44 and 113)	Electrophoretic Mobility (ZP), TEM, AFM	Influence of PEG Mw, zeta potential and size on plasmatic proteins adsorption ⁸³ (corona thickness between 10-15 nm)
plasma proteins	Magnetite NPs stabilized	SDS-PAGE, Mass	Influence of coating,

	with three different carboxylic coating agents: citric acid (~90nm), poly(acrylic acid) (~110nm), and oleic acid double layer (~130nm)	Spectrometry (MS), DLS, ATR-FTIR	influence of plasma concentration. The corona was composed of a wide range of proteins (94 different proteins). ⁸⁹
plasma proteins	Particles of 6 and 9nm silica, 50nm polystyrene, and 50nm carboxyl-modified polystyrene	SDS-PAGE, electrospray liquid chromatography mass spectrometry (LC MS/MS).	Influence of NPs size and surface. To small size of the NPs (9nm) the size of adsorbed proteins is in the same range. ⁹⁰
plasma proteins	NPs of PSOSO ₃ or SiO ₂ (200 and 50 nm)	SDS-PAGE, electrospray liquid chromatography mass spectrometry (LC MS/MS).	Influence of NPs size and surface properties, influence of plasma concentration (3% to 80%) ⁹¹
plasma proteins	Gold NPs 30 and 50nm	2D PAGE, TEM, AFM, DLS, mass spectrometry	Influence of NPs size (more proteins were detected on the 30nm particles than the 50nm particles). Fibrinogen is the most abundant protein adsorbed ⁹² .
Plasma proteins	TiO ₂ (21nm), SiO ₂ (7nm) and ZnO (30nm) NPs	1D and 2D PAGE, mass spectrometry	Influence of NPs composition and size. Fibrinogen and albumin are the most abundant proteins adsorbed ⁸²
Fibrinogen	TiO ₂ (10, 20, 35nm)	Fluorescence, Circular dichroism, DLS, TEM	Influence of NPs size on binding constant with fibrinogen. The size of Fibrinogen-NP complex decrease with time. No structural change is observed ⁹³ .

Table 1.3: overview of literature about protein corona

V. Relevancy of studied system

The interaction between proteins and NPs is essentially investigated by surface techniques (AFM, XPS) and liquid ATR. The effect of shape and size is investigated by selecting two kinds of TiO_2 NPs: nano-rods and nano-sphere. These particles were chosen to have the same diameter (the diameter of spheres equal the width of rods). The aim of this study is to differentiate the formation of corona in solution and the possible denaturation of proteins by the NPs, from the effect at the surface-proteins interface on the protein configuration/denaturation. To do this, two surfaces were investigated, being either hydrophobic or hydrophilic surface (silicon and polystyrene spin coated wafer). The chosen proteins are fibrinogen, human albumin serum (HSA) and collagen for their specific and different properties as well as their natural abundance.

A. Fibrinogen

Fibrinogen (Fg) is a fibrillary plasmatic glycoprotein with a large abundance in the blood (3mg/ml). Fibrinogen interferes in the tissue formation by formation of fibril network. Fg is known to have good adsorption on various surfaces and synthetic material, especially onto hydrophobic and charged surfaces. This protein is composed of two symmetric dimers, each being made of three identical pairs of polypeptides chain: A_α , B_β , γ . A_α is the longest chain compound by 610 amino acid, B_β and γ are approximatively of the same mass (460 and 411 amino acid) to a total of 338kDa for the protein (figure 15). Fg have two preferential conformations, depending on the solution pH (pI=5.5) and ionic strength⁶³. At pH 7.4 the overall charge of fibrinogen is negative.

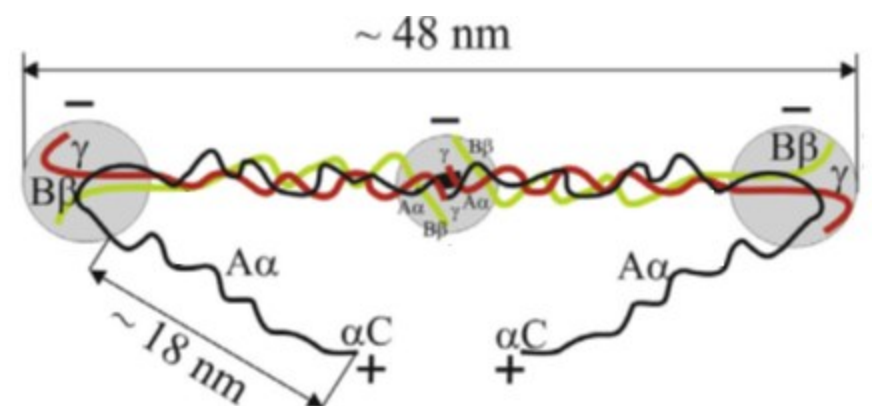


Figure 1.15: fibrinogen molecule conformations and schematic charge distributions at pH 7.4⁹⁴

Fibrinogen is usually used to investigate cell adhesion due to the structural similarity with fibronectin. Anna Gry H et al., studied fibrinogen adsorption on various substrates: titanium oxide, tantalum oxide, and gold using QCM. A difference between the different films was observed showing that the surface chemistry plays a large role in determining the adsorbed amount of proteins⁹⁵.

Christian F. Wertz studied several aspects of fibrinogen adsorption, including the effect of surface hydrophobicity, post-adsorption relaxations and competitive adsorption⁹⁶. They reports that on hydrophobic surfaces, the surface-protein interactions are sufficiently strong to compromise the internal protein structure (footprint= 500nm²), while, on a hydrophilic surface the ultimate footprint is closer to 160 nm² for an isolated fibrinogen molecules. Recently Allouni et al., showed that the adsorption of fibrinogen is time-dependent on spherical TiO₂ anatase nanoparticle (10, 24, 44nm)⁹⁷.

B. Collagen

Collagen is the most abundant structural protein in mammals, located in the extracellular matrix (ECM) of connective tissues. It is also one of the most common bio-compounds with broad applications in biomaterials research, including in drug delivery and tissue engineering. The type I collagen is a right-handed helix composed of three polypeptide chains with non-helical ends (telopeptides), yielding a molecular anisotropic dimensions of ~ 300 nm in length and ~ 1.5 nm in diameter⁹⁸. Each polypeptide chain is a left-handed helix and consists of repeating Gly-X-Y triplets, with about 20% of the X and Y positions occupied by proline and hydroxyproline, respectively. The collagen triple-helix is stabilized via direct inter-chain hydrogen bonds and inter- and intra-chain water-mediated hydrogen bonds⁹⁹. In particular, collagen molecules are strengthened by the formation of water-mediated hydrogen bonds between hydroxyproline residues.

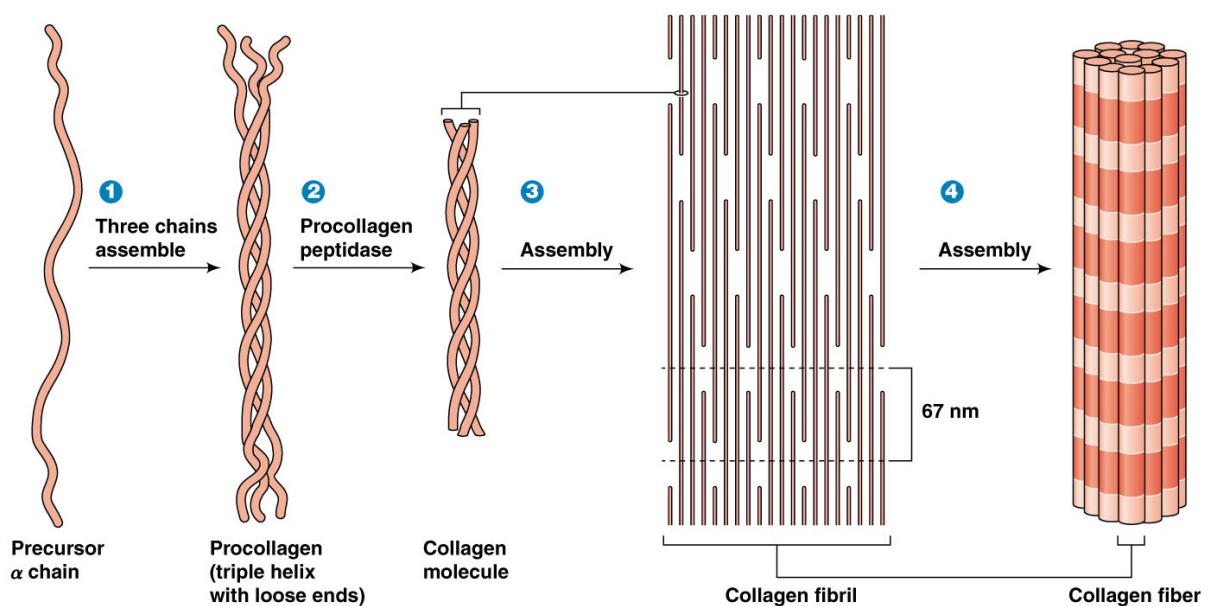


Figure 1.16: Collagen organization and structure at different scales from precursor α chain to collagen fibers¹⁰⁰

Nanostructured collagen layers may be obtained by adjusting the adsorption procedure, the characteristic of the medium (pH, T °C, composition and ionic strength), collagen conformation (native or denatured). The organization of collagen, in the adsorbed phase, depends on the surface properties as shown on figure 17. Collagen adsorption on the surface is governed by the entropy gain due to the dehydration, and the surface property (hydrophobic, hydrophilic and topography). Discontinuous films with holes are observed on hydrophobic substrate while a homogenous film is observed on less hydrophobic substrates¹⁰¹. The behavior of collagen in solution such as fibrillation degree or aggregation in solution determines the formation of fibrillary structure at the liquid (collagen solution) solid (surface) interface. The size and the density of the fibrils formed on hydrophobic substrates decreased with the increasing degree of aggregation of the collagen. Collagen fibrillation in solution depends of the surrounding environment (pH, ionic strength, temperature). While, fibrils formation at the interface is governed by a competitive adsorption process between collagen monomers and aggregates of the solution⁹⁸ (looks like Vroman effect for altered proteins). The effect of drying collagen layers was investigated by AFM¹⁰².

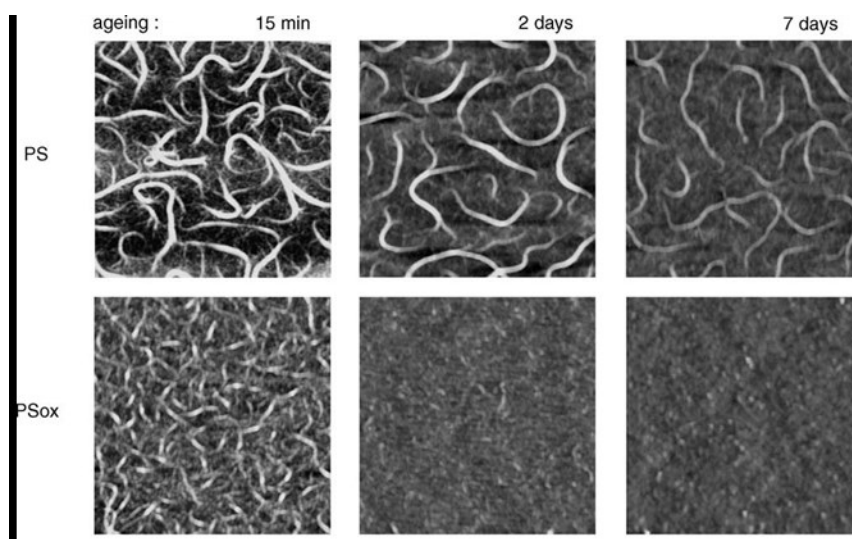


Figure 1.17: AFM air images showing the Impact of hydrophobic or hydrophilic surface on collagen fibrils formation⁹⁸

Collagen adsorption depends on time. On hydrophobic surfaces with short times of incubation (1min or 30min), and for short time or long time (24h) of drying, discontinuous structures are observed, due to the ruptures and displacement of collagen film during drying. But, for the longest time of incubation (>2h) homogenous structure is formed, due to increased collagen–collagen intermolecular interactions. Another study suggests that collagen molecules which are partially denatured in the adsorbed state or during adsorption are less capable of forming a solid network at the interface⁶⁶. The ability of collagen to form structured layers makes it an ideal candidate for surface studies. To the best of our knowledge the interaction between NPs and collagen is not reported in the literature.

C. HSA

Human serum albumin (HSA) is the most abundant plasma protein with a molecular mass of 67kDa. This protein is composed by 585 amino acid residue monomer that contains three homologous α -helical domains. The domains contain ten helices and are divided into antiparallel six-helix and four-helix sub-domain A and B (figure 17). The shape of HAS is approximately equilateral triangular prism with length of $\sim 8\text{nm}$ and height of $\sim 3\text{nm}$ ¹⁰³. At physiological conditions (pH=7,4) HSA is negatively charged (pI=4.7). The principal biological function of HSA is hormones, fatty acids and drug transportation and distribution into the metabolism by travel in plasma.

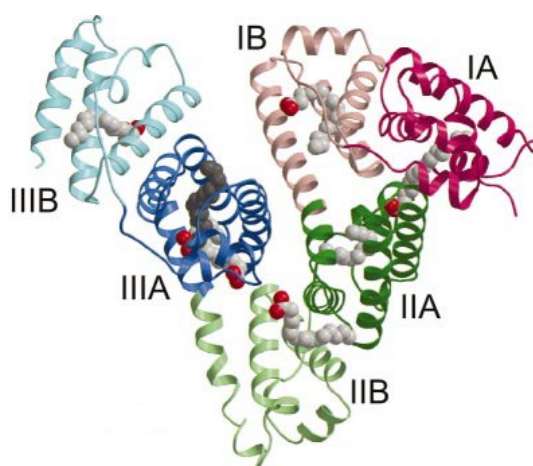


Figure 1.18: Structure of HSA complexed. The protein secondary structure is shown schematically with the domains colored¹⁰³.

It has been reported HSA adsorption depends on pH and temperature⁶⁵. At 37C° the adsorption is higher than at 20C° due to its partial denaturation on the surface. Moreover, adsorption was found to be much lower at pH= 7 than pH= 4.7 (isoelectric point of HSA) on negatively charged surface¹⁰⁴. Fabiana Y et al, studied the adsorption of HSA on colloidal TiO₂ particles (anatase, 30nm). They showed that HSA adsorption onto colloidal TiO₂ particles depends on ionic strength and pH. The adsorption steady state is obtained in few minutes, HSA adsorption depends on the intermolecular lateral repulsion. At physiological pH, the adsorption processes by electrostatic interaction or hydrogen bonding with mono- and di-coordinated surface –OH groups¹⁰⁵.

The three chosen proteins possess various 3D structures which are involved in different biological process. The aim of this study is to probe their interaction with NPs and evaluate the impact in terms

of structural supramolecular organization in solution and in the adsorbed phase. This strategy takes advantages from surface science technique operating in both dried and hydrated phases.

VI. References

1. Buzea, C., Pacheco, I. I. & Robbie, K. Nanomaterials and nanoparticles: sources and toxicity. *Biointerphases* **2**, MR17–R71 (2007).
2. Sun, Y. P. *et al.* Quantum-sized carbon dots for bright and colorful photoluminescence. *J. Am. Chem. Soc.* **128**, 7756–7757 (2006).
3. Stewart, M. E. *et al.* Nanostructured plasmonic sensors. *Chem. Rev.* **108**, 494–521 (2008).
4. Solar, P. *et al.* Multifunctional polymeric nanoparticles doubly loaded with SPION and ceftiofur retain their physical and biological properties. *J. Nanobiotechnology* **13**, 1–12 (2015).
5. Akbarzadeh, A., Samiei, M. & Davaran, S. Magnetic nanoparticles: preparation, physical properties, and applications in biomedicine. *Nanoscale Res. Lett.* **7**, 144 (2012).
6. Cozzoli, P. D. *et al.* Role of Metal Nanoparticles in TiO₂/Ag Nanocomposite-Based Microheterogeneous Photocatalysis. *J. Phys. Chem. B* **108**, 9623–9630 (2004).
7. Musumeci, A. *et al.* SERS of semiconducting nanoparticles (TiO₂) hybrid composites). *J. Am. Chem. Soc.* **131**, 6040–6041 (2009).
8. Beyth, N., Hourri-haddad, Y., Domb, A., Khan, W. & Hazan, R. Alternative Antimicrobial Approach : Nano-Antimicrobial Materials. *Evidence-Based Complement. Altern. Med.* **2015**, 1–16 (2015).
9. Barrow, M. *et al.* Tailoring the surface charge of dextran-based polymer coated SPIONs for modulated stem cell uptake and MRI contrast. *Biomater. Sci.* 608–616 (2015). doi:10.1039/C5BM00011D
10. Report, F. State of the Science Literature Review : Nano Titanium Dioxide. *Environ. Prot.*
11. Weir, A., Westerhoff, P., Fabricius, L., Hristovski, K. & von Goetz, N. Titanium dioxide nanoparticles in food and personal care products. *Environ. Sci. Technol.* **46**, 2242–50 (2012).
12. Valencia, S. H., Marín, J. M. & Restrepo, G. M. Evolution of natural organic matter by size exclusion chromatography during photocatalytic degradation by solvothermal-synthesized titanium dioxide. *J. Hazard. Mater.* **213-214**, 318–324 (2012).
13. Hwu, Y., Yao, Y. D., Cheng, N. F., Tung, C. Y. & Lin, H. M. X-ray absorption of nanocrystal TiO₂. *Nanostructured Mater.* **9**, 355–358 (1997).
14. Chen, X. & Mao, S. S. Titanium dioxide nanomaterials: Synthesis, properties, modifications and applications. *Chem. Rev.* **107**, 2891–2959 (2007).
15. Pierre, A. C. & Pajonk, G. M. Chemistry of aerogels and their applications. *Chem. Rev.* **102**, 4243–4265 (2002).

16. Mugundan, S. *et al.* Synthesis and characterization of undoped and cobalt-doped TiO₂ nanoparticles via sol–gel technique. *Appl. Nanosci.* **5**, 449–456 (2015).
17. Dastan, D. & Chaure, N. B. Influence of Surfactants on TiO₂ Nanoparticles Grown by Sol-Gel Technique. *Int. J. Mater. Mech. Manuf.* **2**, 21–24 (2014).
18. Mahata, S., Mahato, S. S., Nandi, M. M. & Mondal, B. Synthesis of TiO₂ nanoparticles by hydrolysis and peptization of titanium isopropoxide solution. *AIP Conf. Proc.* **1461**, 225–228 (2011).
19. Joo, J. *et al.* Large-Scale Synthesis of TiO₂ Nanorods via Nonhydrolytic Sol - Gel Ester Elimination Reaction and Their Application to Photocatalytic Inactivation of *E. coli*. 15297–15302 (2005).
20. Baek, S., Chai, S., Hur, K. & Lee, W. Synthesis of Highly Soluble TiO₂ Nanoparticle with Narrow Size Distribution. *Bull. Chem. Soc.* **26**, 1333–1334 (2005).
21. Lin, J. *et al.* Hot-fluid annealing for crystalline titanium dioxide nanoparticles in stable suspension. *J. Am. Chem. Soc.* **124**, 11514–11518 (2002).
22. Tang, J. *et al.* An organometallic synthesis of TiO₂ nanoparticles. *Nano Lett.* **5**, 543–548 (2005).
23. Jun, Y. W. *et al.* Surfactant-Assisted Elimination of a High Energy Facet as a Means of Controlling the Shapes of TiO₂ Nanocrystals. *J. Am. Chem. Soc.* **125**, 15981–15985 (2003).
24. Yang, J., Mei, S. & Ferreira, J. M. F. In situ preparation of weakly flocculated aqueous anatase suspensions by a hydrothermal technique. *J. Colloid Interface Sci.* **260**, 82–88 (2003).
25. Morgan, D. L., Liu, H. W., Frost, R. L. & Waclawik, E. R. Implications of precursor chemistry on the alkaline hydrothermal synthesis of Titania/ Titanate nanostructures. *J. Phys. Chem. C* **114**, 101–110 (2010).
26. Dinh, C. T., Nguyen, T. D., Kleitz, F. & Do, T. O. A solvothermal single-step route towards shape-controlled titanium dioxide nanocrystals. *Can. J. Chem. Eng.* **90**, 8–17 (2012).
27. Li, X. L., Peng, Q., Yi, J. X., Wang, X. & Li, Y. Near monodisperse TiO₂ nanoparticles and nanorods. *Chem. - A Eur. J.* **12**, 2383–2391 (2006).
28. Zhao, Y., Zhang, Y., Li, J. & Chen, Y. Solvothermal synthesis of nonmetals-modified SnO₂ nanoparticles with high visible-light-activated photocatalytic activity in the reduction of aqueous Cr(VI). *Sep. Purif. Technol.* **129**, 90–95 (2014).
29. He, F., Ma, F., Li, T. & Li, G. Solvothermal synthesis of N-doped TiO₂ nanoparticles using different nitrogen sources, and their photocatalytic activity for degradation of benzene. *Chinese J. Catal.* **34**, 2263–2270 (2013).
30. Dinh, C., Nguyen, T., Kleitz, F. & Do, T. Shape-Controlled Synthesis of. *ACS Nano* **3**, 3737–3743 (2009).

31. Shi, H., Magaye, R., Castranova, V. & Zhao, J. Titanium dioxide nanoparticles: a review of current toxicological data. *Part. Fibre Toxicol.* **10**, 15 (2013).
32. Kumar, A. *et al.* Innovative pharmaceutical development based on unique properties of nanoscale delivery formulation. *Nanoscale* **5**, 8307 (2013).
33. Sheikhnejad-bishe, O., Zhao, F., Rajabtabar-darvishi, A. & Khodadad, E. Influence of temperature and surfactant on the photocatalytic performance of TiO₂ Nanoparticles. **9**, 4230–4240 (2014).
34. Bayat, N., Lopes, V. R., Schölermann, J., Jensen, L. D. & Cristobal, S. Vascular toxicity of ultra-small TiO₂ nanoparticles and single walled carbon nanotubes in vitro and in vivo. *Biomaterials* **63**, 1–13 (2015).
35. Erriquez, J. *et al.* Nanosized TiO₂ is internalized by dorsal root ganglion cells and causes damage via apoptosis. *Nanomedicine Nanotechnology, Biol. Med.* **11**, 1309–1319 (2015).
36. Geiseler, B., Miljevic, M., Müller, P. & Fruk, L. Phototriggered production of reactive oxygen species by TiO₂ nanospheres and rods. *J. Nanomater.* **2012**, (2012).
37. Uchino, T., Tokunaga, H., Ando, M. & Utsumi, H. Quantitative determination of OH radical generation and its cytotoxicity induced by TiO₂-UVA treatment. *Toxicol. Vitro.* **16**, 629–635 (2002).
38. Bhattacharya, K. *et al.* Titanium dioxide nanoparticles induce oxidative stress and DNA-adduct formation but not DNA-breakage in human lung cells. *Part. Fibre Toxicol.* **6**, 17 (2009).
39. Saptarshi, S. R., Duschl, A. & Lopata, A. L. Interaction of nanoparticles with proteins: relation to bio-reactivity of the nanoparticle. *J. Nanobiotechnology* **11**, 26 (2013).
40. Nel, A. E. *et al.* Understanding biophysicochemical interactions at the nano-bio interface. *Nat. Mater.* **8**, 543–557 (2009).
41. Duncan, R. & Richardson, S. C. W. Endocytosis and Intracellular Trafficking as Gateways for Nanomedicine Delivery : Opportunities and Challenges Endocytosis and Intracellular Trafficking as Gateways for Nanomedicine Delivery : Opportunities and Challenges. (2012). doi:10.1021/mp300293n
42. Khalil, I. a, Kogure, K., Akita, H. & Harashima, H. Uptake pathways and subsequent intracellular trafficking in nonviral gene delivery. *Pharmacol. Rev.* **58**, 32–45 (2006).
43. Q, M. Endosomal leakage and nuclear translocation of multiwalled carbon nanotubes: developing a model for cell uptake. *Nano Lett.* **9**, 4370–4375 (2009).
44. Gallagher, J. *et al.* Formation of DNA adducts in rat lung following chronic inhalation of diesel emissions, carbon black and titanium dioxide particles. *Carcinogenesis* **15**, 1291–1299 (1994).
45. Driscoll, K. E. *et al.* Effects of particle exposure and particle-elicited inflammatory cells on mutation in rat alveolar epithelial cells. *Carcinogenesis* **18**, 423–430 (1997).

46. Salerno, C. & Bregni, C. Molecular Pharmaceutics & Organic Process Research Lipid-based Microtubes : A Promising Drug Carrier. **1**, 1000103 (2013).
47. Zhou, P., Sun, X. & Zhang, Z. Kidney-targeted drug delivery systems. *Acta Pharm. Sin. B* **4**, 37–42 (2014).
48. Chourasia, M. K. & Jain, S. K. Pharmaceutical approaches to colon targeted drug delivery systems. *J. Pharm. Pharm. Sci.* **6**, 33–66 (2003).
49. Panyam, J. & Labhasetwar, V. Biodegradable nanoparticles for drug and gene delivery to cells and tissue. *Adv. Drug Deliv. Rev.* **55**, 329–347 (2003).
50. Bao, G., Mitragotri, S. & Tong, S. Multifunctional nanoparticles for drug delivery and molecular imaging. *Annu. Rev. Biomed. Eng.* **15**, 253–82 (2013).
51. Owens, D. E. & Peppas, N. a. Opsonization, biodistribution, and pharmacokinetics of polymeric nanoparticles. *Int. J. Pharm.* **307**, 93–102 (2006).
52. Roohi, F., Lohrke, J., Ide, a, Schutz, G. & Dassler, K. Studying the effect of particle size and coating type on the blood kinetics of superparamagnetic iron oxide nanoparticles. *Int J Nanomedicine* **7**, 4447–4458 (2012).
53. Albanese, A., Tang, P. S. & Chan, W. C. W. The Effect of Nanoparticle Size, Shape, and Surface Chemistry on Biological Systems. *Annu. Rev. Biomed. Eng.* **14**, 1–16 (2012).
54. Hauck, T. S., Ghazani, A. a. & Chan, W. C. W. Assessing the effect of surface chemistry on gold nanorod uptake, toxicity, and gene expression in mammalian cells. *Small* **4**, 153–159 (2008).
55. Kirchner, C. *et al.* Cytotoxicity of colloidal CdSe and CdSe/ZnS nanoparticles. *Nano Lett.* **5**, 331–338 (2005).
56. Gref, R. *et al.* ‘Stealth’ corona-core nanoparticles surface modified by polyethylene glycol (PEG): Influences of the corona (PEG chain length and surface density) and of the core composition on phagocytic uptake and plasma protein adsorption. *Colloids Surfaces B Biointerfaces* **18**, 301–313 (2000).
57. Zhang, G. *et al.* Influence of anchoring ligands and particle size on the colloidal stability and in vivo biodistribution of polyethylene glycol-coated gold nanoparticles in tumor-xenografted mice. *Biomaterials* **30**, 1928–1936 (2009).
58. Lee, E. S., Gao, Z. & Bae, Y. H. Recent progress in tumor pH targeting nanotechnology. *J. Control. Release* **132**, 164–170 (2008).
59. Scopelliti, P. E., Bongiorno, G. & Milani, P. High-throughput tools for the study of protein-nanostructured surface interaction. *Comb. Chem. High Throughput Screen.* **14**, 205–216 (2011).
60. Haynes, C. a & Norde, W. Structures and Stabilities of Adsorbed Proteins. *Journal of Colloid and Interface Science* **169**, 313–328 (1995).

61. Schlenoff, J. B. Zwitteration: Coating Surfaces with Zwitterionic Functionality to Reduce Nonspecific Adsorption. *Langmuir* **30**, 9625–9636 (2014).
62. Arai, T. & Norde, W. The behavior of some model proteins at solid-liquid interfaces 1. Adsorption from single protein solutions. *Colloids and Surfaces* **51**, 1–15 (1990).
63. Nattich-Rak, M., Adamczyk, Z., Wasilewska, M. & Sadowska, M. Revealing fibrinogen monolayer conformations at different pHs: Electrokinetic and colloid deposition studies. *J. Colloid Interface Sci.* **449**, 62–71 (2015).
64. Höök, F., Rodahl, M., Kasemo, B. & Brzezinski, P. Structural changes in hemoglobin during adsorption to solid surfaces: Effects of pH, ionic strength, and ligand binding. *Proc. Natl. Acad. Sci.* **95**, 12271–12276 (1998).
65. Kopac, T., Bozgeyik, K. & Yener, J. Effect of pH and temperature on the adsorption of bovine serum albumin onto titanium dioxide. *Colloids Surfaces A Physicochem. Eng. Asp.* **322**, 19–28 (2008).
66. Kezwon, A. & Wojciechowski, K. Effect of temperature on surface tension and surface dilational rheology of type I collagen. *Colloids Surfaces A Physicochem. Eng. Asp.* **460**, 168–175 (2014).
67. Roach, P., Farrar, D. & Perry, C. C. Interpretation of protein adsorption: Surface-induced conformational changes. *J. Am. Chem. Soc.* **127**, 8168–8173 (2005).
68. Vörös, J. The density and refractive index of adsorbing protein layers. *Biophys. J.* **87**, 553–561 (2004).
69. Chen, H., Yuan, L., Song, W., Wu, Z. & Li, D. Biocompatible polymer materials: Role of protein-surface interactions. *Prog. Polym. Sci.* **33**, 1059–1087 (2008).
70. Kogler, P., Clayton, A., Thissen, H., Santos, G. N. C. & Kingshott, P. The influence of nanostructured materials on biointerfacial interactions. *Adv. Drug Deliv. Rev.* **64**, 1820–1839 (2012).
71. Lins, L., Thomas, A. & Brasseur, R. Analysis of accessible surface of residues in proteins. *Protein Sci.* **12**, 1406–1417 (2003).
72. Rechendorff, K., Hovgaard, M. B., Foss, M., Zhdanov, V. P. & Besenbacher, F. Enhancement of protein adsorption induced by surface roughness. *Langmuir* **22**, 10885–10888 (2006).
73. Cai, K., Bossert, J. & Jandt, K. D. Does the nanometre scale topography of titanium influence protein adsorption and cell proliferation? *Colloids Surfaces B Biointerfaces* **49**, 136–144 (2006).
74. Lord, M. S. *et al.* The effect of silica nanoparticulate coatings on serum protein adsorption and cellular response. *Biomaterials* **27**, 4856–4862 (2006).
75. Roach, P., Farrar, D. & Perry, C. C. Surface tailoring for controlled protein adsorption: Effect of topography at the nanometer scale and chemistry. *J. Am. Chem. Soc.* **128**, 3939–3945 (2006).

76. Walczyk, D., Bombelli, F. B., Monopoli, M. P., Lynch, I. & Dawson, K. a. What the cell 'sees' in bionanoscience. *J. Am. Chem. Soc.* **132**, 5761–5768 (2010).
77. Jiang, J., Oberdörster, G. & Biswas, P. Characterization of size, surface charge, and agglomeration state of nanoparticle dispersions for toxicological studies. *J. Nanoparticle Res.* **11**, 77–89 (2009).
78. Cedervall, T. *et al.* Detailed identification of plasma proteins adsorbed on copolymer nanoparticles. *Angew. Chemie - Int. Ed.* **46**, 5754–5756 (2007).
79. De Paoli Lacerda, S. H. *et al.* Interaction of gold nanoparticles with common human blood proteins. *ACS Nano* **4**, 365–379 (2010).
80. Cedervall, T. *et al.* Understanding the nanoparticle-protein corona using methods to quantify exchange rates and affinities of proteins for nanoparticles. *Proc. Natl. Acad. Sci. U. S. A.* **104**, 2050–2055 (2007).
81. Gessner, A., Lieske, A., Paulke, B.-R. & Müller, R. H. Functional groups on polystyrene model nanoparticles: influence on protein adsorption. *J. Biomed. Mater. Res. A* **65**, 319–326 (2003).
82. Deng, Z. J. *et al.* Differential plasma protein binding to metal oxide nanoparticles. *Nanotechnology* **20**, 455101 (2009).
83. Natte, K. *et al.* Impact of polymer shell on the formation and time evolution of nanoparticle-protein corona. *Colloids Surfaces B Biointerfaces* **104**, 213–220 (2013).
84. Lynch, I. *et al.* The nanoparticle-protein complex as a biological entity; a complex fluids and surface science challenge for the 21st century. *Adv. Colloid Interface Sci.* **134-135**, 167–174 (2007).
85. Adams, a L. in *Plasma at.* **55**, 156–159 (1980).
86. Göppert, T. M. & Müller, R. H. Adsorption kinetics of plasma proteins on solid lipid nanoparticles for drug targeting. *Int. J. Pharm.* **302**, 172–186 (2005).
87. Walkey, C. D. & Chan, W. C. W. Understanding and controlling the interaction of nanomaterials with proteins in a physiological environment. *Chem. Soc. Rev.* **41**, 2780 (2012).
88. Milani, S., Baldelli Bombelli, F., Pitek, A. S., Dawson, K. a. & Rädler, J. Reversible versus irreversible binding of transferrin to polystyrene nanoparticles: Soft and hard corona. *ACS Nano* **6**, 2532–2541 (2012).
89. Jedlovsky-Hajdú, A., Bombelli, F. B., Monopoli, M. P., Tombácz, E. & Dawson, K. a. Surface coatings shape the protein corona of SPIONs with relevance to their application in vivo. *Langmuir* **28**, 14983–14991 (2012).
90. Lundqvist, M. *et al.* The evolution of the protein corona arounds Nanoparticles: A test study. *ACS Nano* **5**, 7503–7509 (2011).

91. Monopoli, M. P. *et al.* Physical-Chemical aspects of protein corona: Relevance to in vitro and in vivo biological impacts of nanoparticles. *J. Am. Chem. Soc.* **133**, 2525–2534 (2011).
92. Dobrovolskaia, M. a. *et al.* Interaction of colloidal gold nanoparticles with human blood: effects on particle size and analysis of plasma protein binding profiles. *Nanomedicine Nanotechnology, Biol. Med.* **5**, 106–117 (2009).
93. Wang, C. & Li, Y. Interaction and nanotoxic effect of TiO₂ nanoparticle on fibrinogen by multi-spectroscopic method. *Sci. Total Environ.* **429**, 156–160 (2012).
94. Adamczyk, Z. *et al.* Fibrinogen conformations and charge in electrolyte solutions derived from DLS and dynamic viscosity measurements. *J. Colloid Interface Sci.* **385**, 244–257 (2012).
95. Hemmersam, A. G., Foss, M., Chevallier, J. & Besenbacher, F. Adsorption of fibrinogen on tantalum oxide, titanium oxide and gold studied by the QCM-D technique. *Colloids Surfaces B Biointerfaces* **43**, 208–215 (2005).
96. Santore, M. M. & Wertz, C. F. Protein spreading kinetics at liquid-solid interfaces via an adsorption probe method. *Langmuir* **21**, 10172–10178 (2005).
97. Allouni, Z. E., Gjerdet, N. R., Cimpan, M. R. & Hol, P. J. The effect of blood protein adsorption on cellular uptake of anatase TiO₂ nanoparticles. *Int. J. Nanomedicine* **10**, 687–695 (2015).
98. Dupont-Gillain, C. C., Jacquemart, I. & Rouxhet, P. G. Influence of the aggregation state in solution on the supramolecular organization of adsorbed type I collagen layers. *Colloids Surfaces B Biointerfaces* **43**, 179–186 (2005).
99. Grant, C. a., Phillips, M. a. & Thomson, N. H. Dynamic mechanical analysis of collagen fibrils at the nanoscale. *J. Mech. Behav. Biomed. Mater.* **5**, 165–170 (2012).
100. Markus J. Buehler Nature designs tough collagen: Explaining the nanostructure of collagen fibrils PNAS 2006 103 (33) 12285-12290.
101. Dufr ne, Y. F., Marchal, T. G. & Rouxhet, P. G. Influence of Substratum Surface Properties on the Organisation of dsorbed Collagen Films: In Situ Characterization by Atomic Force Microscopy. *Langmuir* **15**, 2871–2878 (1999).
102. Jacquemart, I., Pamula, E., De Cupere, V. M., Rouxhet, P. G. & Dupont-Gillain, C. C. Nanostructured collagen layers obtained by adsorption and drying. *J. Colloid Interface Sci.* **278**, 63–70 (2004).
103. Petitpas, I., Gru, T., Bhattacharya, A. a & Curry, S. Crystal Structures of Human Serum Albumin Complexed with Monounsaturated and Polyunsaturated Fatty Acids. 955–960 (2001). doi:10.1006/jmbi.2001.5208
104. Haynes, C. a. & Norde, W. Globular proteins at solid/liquid interfaces. *Colloids Surfaces B Biointerfaces* **2**, 517–566 (1994).
105. Oliva, F. Y., Avalor, L. B., C mara, O. R. & De Pauli, C. P. Adsorption of human serum albumin (HSA) onto colloidal TiO₂ particles, Part I. *J. Colloid Interface Sci.* **261**, 299–311 (2003).

Chapter 2: Materials and methods

Table of contents

Chapter 2: Materials and methods	61
I. Synthesis of titanium dioxide NPs (TiO₂ NPs).....	63
A. Materials.....	63
B. Synthesis of titanium dioxide nano-spheres	63
C. Synthesis of titanium dioxide nano-rods synthesis	63
II. Adsorption procedure to study Proteins-NPs interaction	65
A. Materials.....	65
B. Preparation of proteins solutions.....	65
C. Choice of NPs.....	65
D. Preparation of wafer	65
E. Preparation of NPs protein solution.....	66
F. Procedure I for protein-nanoparticle deposition on wafers	66
G. Procedure II for protein-nanoparticle deposition on wafers	66
III. Characterization techniques	67
A. Transmission electron microscope (TEM)	67
B. Electrophoretic mobility (EPM)	67
C. Dynamic Light Scattering (DLS).....	68
D. UV absorption.....	68
E. X-Ray Diffraction (XRD).....	69
F. X ray Photoelectron spectroscopy (XPS)	69
G. Infrared spectroscopy in the attenuated total reflectance mode (IR-ATR)	70
H. Atomic force microscopy (AFM).....	71

I. Synthesis of titanium dioxide NPs (TiO₂ NPs)

A. Materials

Reagents: Ti(IV) isopropoxide (Ti(OPri)₄, assay 97%), benzyl alcohol (BzOH, assay 99%) and acetic acid (CH₃COOH, assay 99.7%) were obtained from commercial sources (sigma Aldrich) and used without further purification, MilliQ water was filtered (MilliQ, Millipore, France). Experiments were carried out at room temperature if not specified otherwise. All glassware, sample and material were cleaned with a piranha solution (2:1 volume of concentrated sulfuric acid and hydrogen peroxide 30%), rinsed with ultrapure water and dried on N₂ flux.

B. Synthesis of titanium dioxide nano-spheres

Spheres were obtained varying the molar concentration between Ti(IV) isopropoxide (Ti(OPri)₄) and benzyl alcohol (BzOH) as described in table 1. The reagents were mixed and the resulting solution was stirred for 30 min at room temperature. Then, the mixture was transferred into a steel autoclave equipped with a Teflon cap and kept to 200 °C for 20 h. During this time the mixture turned from liquid to white suspension. After 20h the reaction was stopped and cooled at room temperature. The suspension was centrifuged (9000 rpm for 30 min) and washed with ethanol and dichloromethane twice. After each centrifugation, the precipitate was sonicated 10 min to favor a complete dispersion of solid precipitate. Then, the precipitate was dried at atmosphere.

Concentration of reagents (mol L ⁻¹)		Molar concentration ratios
Ti(OPri) ₄	BzOH	[BzOH]/[Ti(OPri) ₄]
0.96	6,86	7,1
0.67	7,69	11,4
0.56	8.00	14,2

Table 2.1: Composition of the reaction mixture: concentration of the main reagents and the corresponding molar concentration ratios used for the synthesis of nano-spheres

C. Synthesis of titanium dioxide nano-rods

Rods were obtained by different molar concentration between Ti(IV) isopropoxide (Ti(OPri)₄), benzyl alcohol (BzOH) and acetic acid (CH₃COOH) as reagents (see table 2). TiO₂ nano-rods were synthesized at three concentration ratios between Ti(OPri)₄ and BzOH. To each ratio described above the concentration ratio between CH₃COOH and BzOH was varied in order to observe the influence of acetic acid on the resulting NPs. The reagents were mixed and then, the solution was stirred for 30 min at room temperature and transferred into a steel autoclave equipped with a Teflon cap and kept

to 200 °C for 20 h. During this time, the mixture turned from liquid to white suspension. After 20h the reaction was stopped and cooled to room temperature. The suspension was centrifuged (9000 rpm for 30 min) and washed with ethanol and dichloromethane twice time. After each centrifugation, the precipitate was sonicated 10 min to favor a complete dispersion of solid precipitate. Then, the precipitate was dried at atmosphere.

Concentration of reagents (mol L ⁻¹)			Molar concentration ratios	
CH ₃ COOH	Ti(OPri) ₄	BzOH	[CH ₃ COOH]/[BzOH]	[BzOH]/[Ti(OPri) ₄]
2.88	0.56	6.41	0.45	11.4
2.26	0.59	6.69	0.34	11.4
1.59	0.61	6.99	0.23	11.4
0.82	0.64	7.33	0.11	11.4
1.34	0.52	7.38	0.18	14.2
0.69	0.54	7.68	0.09	14.2
0.56	0.54	7.74	0.07	14.2
0.42	0.55	7.80	0.05	14.2
0.28	0.55	7.87	0.04	14.2
0.14	0.56	7.93	0.02	14.2
2.70	0.81	5.78	0.47	7.1
2.18	0.84	6.00	0.36	7.1
0.66	0.93	6.59	0.10	7.1

Table 2.2: Composition of the reaction mixture: concentration of the main reagents and the corresponding molar concentration ratios used for the synthesis of nano-rods.

II. Adsorption procedure to study Proteins-NPs interaction

A. Materials

Si wafers were purchased from Sigma Aldrich. Wafers were polished only on single side by the manufacturer and were N-type with no dopant, the thickness is 0.5mm, and the crystalline plan is [100]. Wafers were cut with a diamond pen in order to obtain regular dimension of about 1cm by 1cm sample. All glassware and sample were cleaned with a piranha solution, rinsing with ultrapure water and dried on N₂ flux. Proteins were purchased from Sigma Aldrich. The tablets of phosphate buffer saline (PBS: NaCl 137mM, Na₂HPO₄ 10 mM, NaH₂PO₄ 10 mM) were purchased from Sigma Aldrich (pH=7.4) and diluted in ultrapure water (MilliQ, Millipore, France) at room temperature during 10min.

B. Preparation of protein solutions

Proteins (Collagen, HSA and Fibrinogen) were studied, in order to investigate the influence of size and shape of NPs during the process of interaction and corona formation (see procedure I paragraph 2.6). Proteins were dissolved in PBS solution and then stored in the refrigerator at 4°C.

C. Choice of NPs

Nanoparticle were synthesized in order to investigate the evolution of aspect ratio in function of the increasing of the AcOH/BzOH molar concentration ratio, here, we focus on the characteristic of TiO₂ NPs with the smallest aspect ratio ~1 (nano-spheres,) and the biggest aspect ratio ~3 (nano-rods). Table 3 shows the average size of selected NPs.

Shape of NPs	Width (nm)	Length (nm)	Diameter (nm)
Rod	7.8±0.8	21.8±2.6	
Sphere			7.6±1.0

Table 2.3: Characteristics of chosen NPs

D. Preparation of wafers

All wafers were cleaned with Piranha solution (2:1 volume of concentrated sulfuric acid and hydrogen peroxide 50%) in the order to remove all organic contamination. In this study two types of surface were used: an Si clean surface (as a hydrophilic surface), and an Si surface modified by a deposit of Polystyrene (PS) (as a hydrophobic surface). Solution for spin coating was prepared by

dissolving PS blocks in anhydrous toluene. PS blocks have Mw around 350,000 and Mn around 170,000 g.mol⁻¹. Solution at 10 g/L of PS was used, dissolving PS blocks in anhydrous toluene during 5h at 50°C. Two drops of this solution were deposited on Si wafer (1cm*1cm) followed by spin coating at 5000 rpm (acceleration 9000 rpm/s) during 40sec. Then, wafers were used immediately, or kept under vacuum and used after.

E. Preparation of NPs protein solution

NPs and proteins were dispersed in phosphate buffer saline solution (obtained from Sigma tablet) with a ratio of 1:10 (100ug.ml⁻¹ proteins and 10ug.ml⁻¹ NPs), after a previous sonication of NP solution of 5min.

F. Procedure of incubation: “procedure I”

Procedure I consists in three main steps: (i) Firstly, proteins and NPs are mixed, the resulting NPs-proteins interaction is responsible to the formation of corona's effect. Parameters of temperature and time of interaction can be modified in order to check their influence on corona formation. For this purpose, we adopt two temperatures (20°C and 37°C) and two interaction times (20 min and 24h). The selected temperature (20°C or 37°C) is kept for the rest of the experiment. (ii) The second step consists in the incubation of the wafer during 2hours. (iii) The third step includes a rinsing of the wafer in PBS solution, three times during 5min and drying with the same conditions of drying time under N₂ flux for 10s.

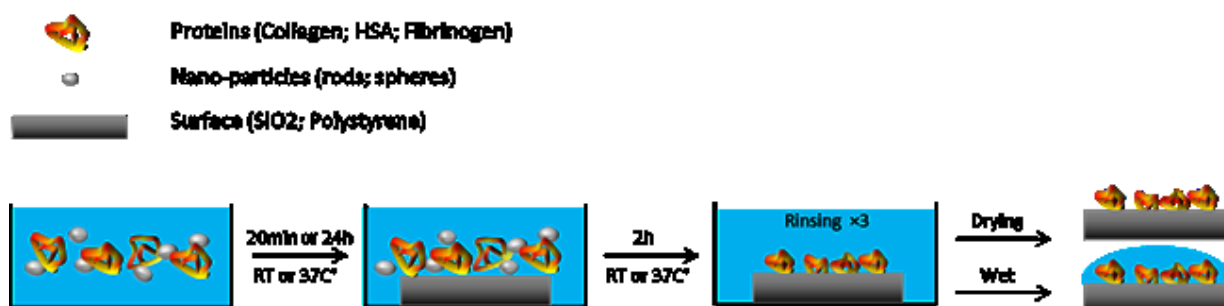


Figure 2.1: Schematic representation of procedure I with the different steps.

G. Procedure of incubation: “procedure II”

This procedure was developed in order to study the interaction of NPs onto a surface previously covered by proteins. This procedure consists in three steps. (i) First, the wafer is incubated in 2ml of

protein solutions for 2 hours at room temperature. (ii) Second, a solution of NPs is gradually injected, to replace the original solution (three cycles: 1 ml of proteins solution was taken and 1 ml of NPs solution is injected). For that step, the incubation time of wafer and NPs is fixed at 24 h and the temperature at 20°C. The last step is the rinsing of wafer in PBS solution (three cycles: 1 ml of NPs solution was taken and 1 ml of PBS solution is injected) and dried with the same conditions of drying time under N_2 flux for 10 s.

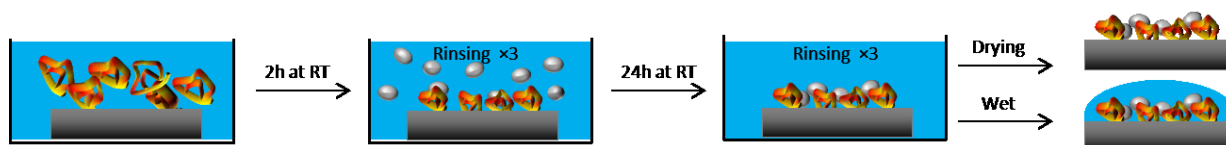


Figure 2.2: Schematic representation of procedure with the different steps.

III. Characterization techniques

A. Transmission electron microscope (TEM)

The size and shape of NPs is a key parameter in order to describe and understand the interaction between protein and NPs. TEM was used to image the synthesized NPs and possibly obtain crystallographic information. Electron microscope imaging was performed on a JEOL JEM 1011 microscope operating at an accelerating voltage of 100 kV. Images were treated by ImageJ software. High resolution analyses (HRTEM) were performed using a Jeol electron microscope 2011 UHR (LaB6) operating at 200 kV voltage and having a punctual resolution of 1.8 Å. Micrographies were recorded using Orius Gatan camera and images were processed by DigitalMicrograph software. For classical and high resolution imaging the nano-particles were solubilized in ultrapure water or DMF. After the ultrasonic treatment, the solution was deposited on 400-mesh carbon-coated copper grids and the solution was immediately evaporated.

B. Electrophoretic mobility (EPM)

The electrophoretic mobility (EPM) of particles is measured by applying an externally electric field. The direction and rate of the movement depend on the polarity and the density of the particles net surface charge as well as the strength of the electric field, the ionic strength, the temperature and the pH of the medium. EPM measurements were carried out using a Malvern Zetasizer nanoZS using disposable polystyrene cuvettes (Malvern, DTS1061, Malvern Instruments Ltd, Malvern, UK), at 22

°C. The performance of the instrument was systematically verified (every six samples) using a zeta potential standard solution (Malvern, DTS1232). The results are presented as the mean and standard deviation of three to five replicates.

C. Dynamic Light Scattering (DLS)

DLS was used to characterize the behavior of titanium dioxide NPs in solution, this technique gives information about the aggregation state of NPs, by analyzing the size distribution of the formed aggregates in solution. Buffer solutions were prepared in ultrapure water (MilliQ, Millipore, France). The composition, the measured pH values and the ionic strength (I) are given in the table 4. For incubation tests, TiO₂ nanoparticle powder was dissolved in a freshly prepared buffer and the mixture was stirred using a vortex until a homogenous suspension was obtained. 1mg of titanium dioxide NPs (nano-spheres or nano-rods) was diluted in 1ml PBS or phosphate buffer non-saline and transferred to 2.0 ml polystyrene tank. The Z-average hydrodynamic diameter and polydispersity index were measured using a ZetaSizer Nano ZS (Malvern Instruments) with attenuator position set to automatic. Six to nine measurements were performed for each solution of NPs

Compounds	Solutions				
	PBS (mM)	Phosphate buffer (mM)			
NaH ₂ PO ₄	30	30	30	30	30
Na ₂ HPO ₄	70	70	70	70	70
NaCl	154	0.0	17	85	154
Measured pH	7.4	7.4	7.4	7.4	7.4
I (mM)	239.7	240	257	325	394

Table 2.4: Composition of the solutions used for the incubation of TiO₂ NPs, measured pH, and computed ionic strength (I). The highest phosphate buffer concentration represents the same concentration as PBS composition.

D. UV absorption

The chemical catalytic activities of the TiO₂ NPs samples (spheres and rods) were evaluated by the color degradation of methyl blue (BM) in an aqueous solution and PBS. The ability of TiO₂ NPs to generate radicals in aqueous solution was monitored by the bleaching of BM. Absorbance was measured by a spectrometer at 660 nm, using a UV PMMA (polymethyl methacrylate) reservoir, having with a length of 1 cm. BM was diluted in ultrapure water or in PBS solution. Degradation of BM was studied at various concentrations of NPs and peroxide hydrogen (H₂O₂) in PBS and water for 2 h. Solutions of BM at 200 µM and hydrogen peroxide at 4.9M (at 30 wt. % in H₂O) were used. Each

solution was mixed during 1 min and protected from ambient light with a tin foil. Before each measurement the solutions were centrifuged. Table 5 shows the concentration ratio tested. The fraction of BM bleaching was computed as follows: Fraction of BM bleaching = $1 - A_t/A_0$. Where A_0 and A_t correspond to the absorbance values measured at $t = 0$ s and after MB bleaching ($t = 2$ h), respectively.

	[NPs] 10ug.ml ⁻¹	[NPs]100 ug.ml ⁻¹	[NPs] 1000 ug.ml ⁻¹
PBS, 3% [H₂O₂]			
150uL BM	15ug NPs	150ug NPs	1500ug NPs
150uL H ₂ O ₂			
1200uL PBS			
Water, 3% [H₂O₂]			
150uL BM	15ug NPs	150ug NPs	1500ug NPs
150uL H ₂ O ₂			
1200uL H ₂ O			
Water, 9% [H₂O₂]			
150uL BM	15ug NPs	150ug NPs	1500ug NPs
450uL H ₂ O ₂			
900uL H ₂ O			

Table 2.5: Composition of the solutions used for the incubation of TiO₂ NPs

E. X-Ray Diffraction (XRD)

XRD was used to check the cristallinity of NPs and identify the crystallographic structure of NPs. Powder X-ray diffraction (XRD) was recorded on a Siemens D500 diffractometer, on a Bruker D8 diffractometer using Cu K α radiation (1.5418 Å). The XRD patterns were recorded in the range of $2\theta = 20 - 80^\circ$, using 2θ increments of 0.02 and a fixed counting time of 2s/step. The crystalline phases were determined from a comparison of the registered on the American mineralogist crystal structure database.

F. X ray photoelectron spectroscopy (XPS)

XPS is an analytical method to study surface, based on emission of photoelectrons from a solid, induced by X ray irradiation. This technique gives the chemical composition of the surface with a depth penetration of 1 to 10 nm (depends of the analyzed electrons and the type of sample). The obtained values of binding energy of photoelectrons are precise to 0.2 eV. In the case of protein adsorption on a substrate this technique allows to get information about the surface coverage and the thickness of protein films by analyzing the relative intensities of nitrogen, an element typically present in proteins, and that of the substrate. Moreover, by analyzing the binding energy of the

various contributions in a peak, chemical groups can be identified. The analyzed samples were obtained from procedures I and II (meaning Si or PS substrates covered by proteins under different conditions of incubation, with or without NPs). Before XPS measurements the samples were dried in a N₂ flux, then, the samples were fixed on the support by a double side adhesive tape. XPS analyses were performed using a SPECS (Phoibos MCD 100), X-ray photoelectron spectrometer (SPECS, Germany) equipped with a monochromatized aluminum X-ray source ($h\nu = 1,486.74$ eV), and a Phoibos 100 hemispherical energy analyzer. Pass energies of 20 eV was used for survey scans; and 10 eV for narrow scans, no charge stabilization was applied. The pressure in the analysis chamber during measurement was around 10^{-10} Torr. The photoelectron collection angle between the normal to the sample surface and the analyzer axis was 0. Spectra were treated with Casa XPS software (Casa Software Ltd., UK).

G. Infrared spectroscopy in the attenuated total reflectance mode (IR-ATR)

Due to the high polarity of amide bands (C=O stretching vibrations, N-H bend and C-N stretch), and its sensitivity to the chemical environment, infrared spectroscopy is an optimal technique to investigate the possible conformational changes of proteins in solution and/or in the presence of NPs. By analyzing the band position as well as the intensity ratio of amide I/amide II bands, information could be deduced relative to the secondary structure (β -sheet, random coil, α -helix...) of the proteins. The experiments were conducted in order to observe the influence of NPs on protein conformation, in particular after the procedure I (formation of a corona). NPs and proteins were dispersed in Phosphate buffer saline solution with a ratio of 10:1 (1 mg.ml⁻¹ proteins and 100 μ g.ml⁻¹ NPs). The formation of corona takes place at room temperature (or 37 C°) and during 20 min (or 24 h). Then, the mixture was centrifuged during 15 min at 13 000 rpm and the supernatant was recovered. 1 ml of the supernatant was placed on the ATR crystal (ZnSe). In order to remove adsorption signals from CO₂ in the air, the device was purged by N₂ during 10 min between each measurement. Other experiments were realized with the same procedure without centrifugation in order to observe the nanoparticle contribution on the spectra. For each measurement, a reference was realized with PBS twice and three spectra were recorded for each sample. Spectra were acquired with 256 scans in the 400-4000 cm⁻¹ range, the resolution was 8 cm⁻¹.

H. Atomic force microscopy (AFM)

AFM is the main technique of this work. AFM allows imaging surfaces with a nanometer resolution giving also precise information on the z-scale. AFM technique is based on measurement of force interaction between the analyzed surfaces and the tip, as shown on figure 3. The tip is mounted on a cantilever made of silicon nitride (Si_3N_4). Shape of tip, spring constant and resonance frequency are important parameters to choose the tip, depending on the type of analyzed sample. The sample is fixed on an electrical piezo, the application of a tension allows to move the sample in the three directions of space x,y and z. The laser beam is reflected on the surface of the tip, this reflection is collected by a photodiode compound by four dials. The position variations of the laser on the photodiode allows to measure deflection of the tips on the surface. The tip is subjected to mechanical stress, which results in changes of the laser position on the photodiode. A control loop (feedback loops) permits to control the applied force on the sample and avoid breaking the tips. AFM has three main working modes: contact, non-contact and oscillating. This technique is optimal to image biological elements in aqueous solution at physiological conditions. Mechanical properties of the surface such as: hardness, Young modulus, interaction force between the tip and the elements on the surface are provided by analyzing data.

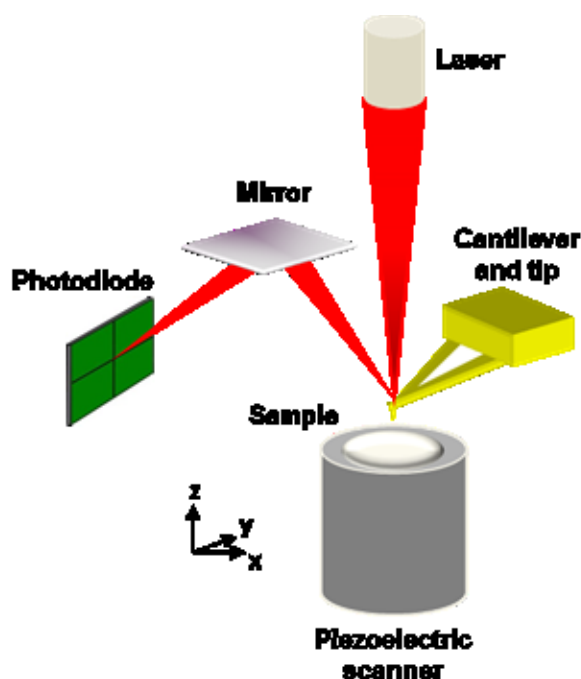


Figure 2.3: Operating sketch of AFM device

a. Contact mode

In contact mode the tip is in contact with the sample as it is shown on figure 4. This mode is the most precise, the tip does not vibrate and the movement of piezo in the z direction strictly reflects the sample topography. The feedback loop has to be fast enough to measure the changes in the topography of the sample, but slow enough to avoid system oscillation. That means that the force exerted on the sample by the tip can be high (in the case of the feedback loop is too slow). In this case the sample can be deteriorated by the tip, specifically if the sample contains fragile biological materials.

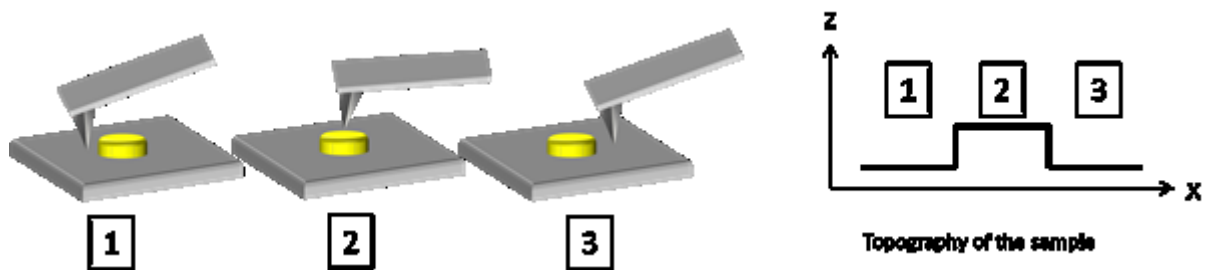


Figure 2.4: Contact mode to obtain topography of the sample and the corresponding cross section. Step 1 the cantilever is not deflected no variation of position of the laser beam is detected by the photodiode, step 2 the cantilever is deflected traducing by a variation in height; step 3, the laser beam returns to the initial position on the photodiode corresponding to $z = 0\text{nm}$.

b. Taping modeTM

In Tapping modeTM, the cantilever vibrates at its own resonance frequency and is in intermittent contact with the sample surface. The movement of the cantilever can be described with the harmonic oscillator model. In this model the position of the cantilever $Z(t)$ is the stationary part of the solution of the equation of an amortized harmonic oscillator and can be described by the following equation:

$$Z(t) = A(\nu) \cos(2\pi t + \Phi(\nu))$$

Equation 2.1: Position of the cantilever $Z(t)$, where: $A(\nu)$ is the reduced amplitude (amplitude of vibration that is maintains constant), and $\Phi(\nu)$ the shift of phase introduced by the interaction with the surrounding medium.

The half width of the amplitude curve $A(\nu)$ defines the quality factor Q ($Q = \nu/\Delta\nu$) of the cantilever. The higher this factor is, the more sensitive the system is. In air, the value of Q is typically 100, while, under ultrahigh vacuum this value may be greater than 1000 showing the influence of the surrounding medium on AFM measurements. When the tip approaches the surface the interaction between the tip and the surface (VdW forces) modifies the oscillation amplitude. The resonance

frequency shifts to a lower value on the effect of the gradient of attractive forces as shown on figure 5 C. The expression of the resulting frequency can be described by the following equation:

$$\nu'_0 = \nu_0 \left(1 - \frac{\partial F / \partial Z}{k}\right)^{-1/2}$$

Equation 2.2: Expression of the resonance frequency of the cantilever submitted to a gradient of attractive forces, where: ν_0 is the resonance frequency of the cantilever in free resonance, $\partial F / \partial Z$ is the gradient of attractive forces and k is the spring constant of the spring.

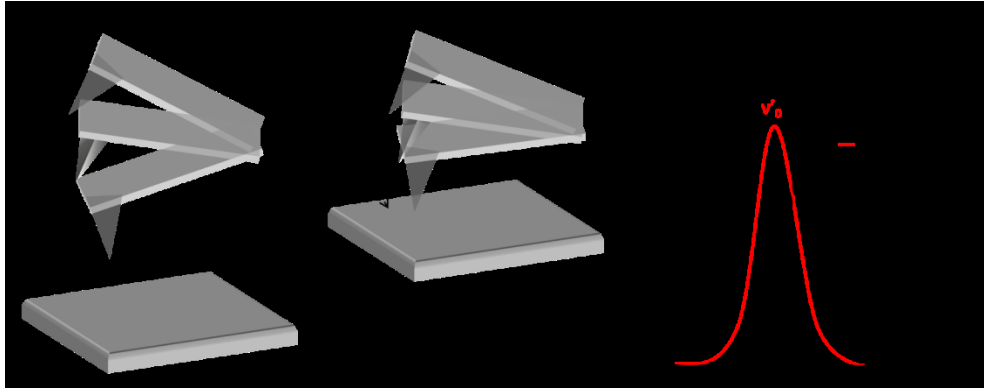


Figure 2.5: Vibration tips in tapping mode, case A free resonance mode, case B coupling resonance mode between tip and surface, C in black the spectra obtained far from the surface (no interaction forces) in red the spectra obtained near to the surface presenting a shift to lower frequency (with an increase in attractive forces).

AFM tapping mode allows to images surface with a high lateral resolution (1 to 5 nm), the applied forces are weak and cause less damage on the sample than in contact mode. The main negative point is the acquisition time which longer than in contact mode, depending on the quality factor Q and the resonance frequency of the cantilever.

c. Non-contact mode

In this mode the cantilever is excited in the same manner as in the intermittent mode, but the tip never touches the sample surface. The tip oscillates near the surface, at distances of the order of 10 Å. The non-contact mode operates in the same manner as the intermittent contact mode, exploiting the non-linear behavior of the oscillator model when the tip is near the surface. The measurement is made on the evolution of the resonance frequency and on the required intensity of the excitation to maintain a constant amplitude movement of the tip. The attractive forces are weak and difficult to quantify, leading to a low resolution of the analyzed sample image.

d. Peak force tapping mode (PFT)

In PFT mode the tip is in intermittent contact with the sample surface. On this mode the tip makes oscillations far below the resonance frequency of the cantilever as shown in figure 6. The resonance

frequency of the z-piezo is around 2 kHz (comparing to 10 kHz in oscillating mode) with an amplitude around 120 nm, providing a very fast approaching-retracting curves for each pixel of the image and leading to a reduction of acquisition time (comparing with the oscillating mode). The tip and sample proximity allows recording information without damaging the imaged surface. The obtained images possess a good lateral resolution (1 to 5 nm). In the present work, all topographic data were obtained using the PFT mode.

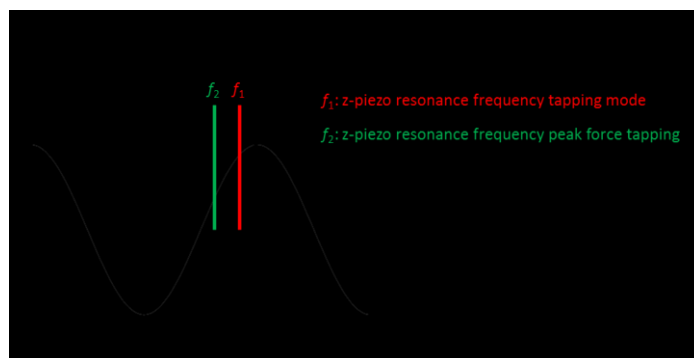


Figure 2.6: Resonance frequency of oscillation mode (tapping and peak force tapping). The curve represents the amplitude in function of the resonance frequency of the cantilever.

e. Force spectroscopy

AFM is not limited to surface imaging but allows also measuring physical properties and molecular interactions: this is the force spectroscopy. Force spectroscopy consists in a direct measurement of tip-sample force interaction. Figure 7 shows a typical force curve with the different steps during the approaching and retracting the tip on and from the sample surface. In the first step the tip is far away from the surface (10-100 microns) the cantilever is not deflected and, no force is measured. When the tip approaches the surface, the cantilever may jump due to repulsive forces (figure 7, step 2) this jump appears when the gradient of attractive forces between the tip and the sample is higher than the addition of spring constant and repulsive forces. When the force increases (figure 7, step3) the cantilever is deflected. A set point value is preselected, corresponding to the maximal force which will be applied by the tip on the surface. In step 3, the deflection of the cantilever increases until it reaches the set point values. Upon reaching the set point value, the time of residence of the tip on the surface sample can be modified: this is the surface delay. Typically an increasing of surface delay time increases the probability of interaction between the tip and the molecules on the ample surface. When the tip is retracted (figure 7, step 4) the force curve displays a hysteresis corresponding to the adhesion force. By measuring the value of the hysteresis it is possible to determine the adhesion force between the tip and the molecules on the sample surface. In the last

step, the tip returns to the initial position similar to step 1, the cantilever is not deflected. To measure a force quantitatively, the systems have to be calibrated. The relationship between the deflection of the tip and the variation of the signal on the photodiode has to be established, meaning to convert the vertical axis from the photodiode in Volts to Newton. The first step consists in measuring the deflection sensitivity of the tip on a reference surface, using the gradient of the withdrawal curve in the contact area between the tip and the sample to convert the vertical from unit of tension (V) to unit of length (nm). The second step consists in determining the spring constant of the cantilever. To do this, the “thermal tune application” of the AFM software is used: the tip is forced, to oscillate far from the surface in order to find the cantilever spring constant, by applying the Hooke’s law: $F = -k * d$ (where k is the cantilever spring constant), then the vertical axis has force unit (pN). Until the system calibrated, the force curve can be exploited.

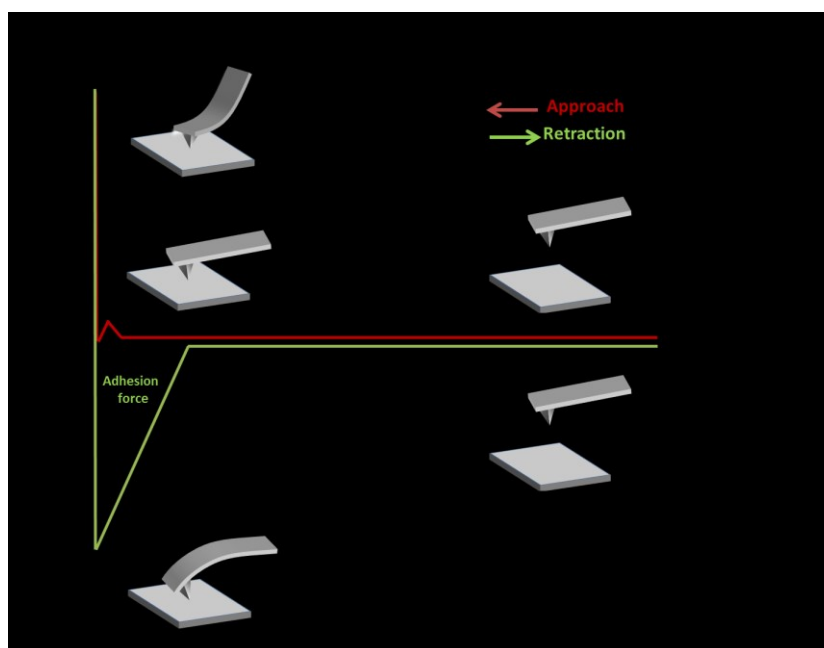


Figure 2.7: Representation of a typical force-distance curve. Steps 1 and 5 the tip is not in contact with the surface. Step 2, 3 and 4, the tip is in contact with the surface.

The force spectroscopy mode is adapted to study the conformation of biological elements such as adsorbed fibrillary proteins at physiological condition. By analyzing the curves, the size of fibrils and the supramolecular arrangement of adsorbed protein can be determined. Two parameters are important in this mode: the ramp-z (distance of retraction between the tip and the surface sample for each measurement) and the surface delay time. The ramp-z distances have to be higher than the size of the studied fibril, in order to record and detect all the rupture events on whole fibril size. Figure 8 illustrates the importance of the ramp-z distance in the case of two different conformations of an adsorbed fibrillar protein. In case A, the fibril forms a protein layer with high density due to a

high degree of fibrillation, a short ramp-z distance is sufficient. In case B, the degree of fibrillation is low and the size of fibrils (length) is large; in such as configuration, the ramp-z distance has to be large enough to measure the whole fibril. Surface delay allows determining whether the interaction between the tip and molecules on the surface is time dependent or not. For example, in the case of specific interactions between the tips and the molecules on the surface the probability of adhesion events will be more important for the longest interaction times.

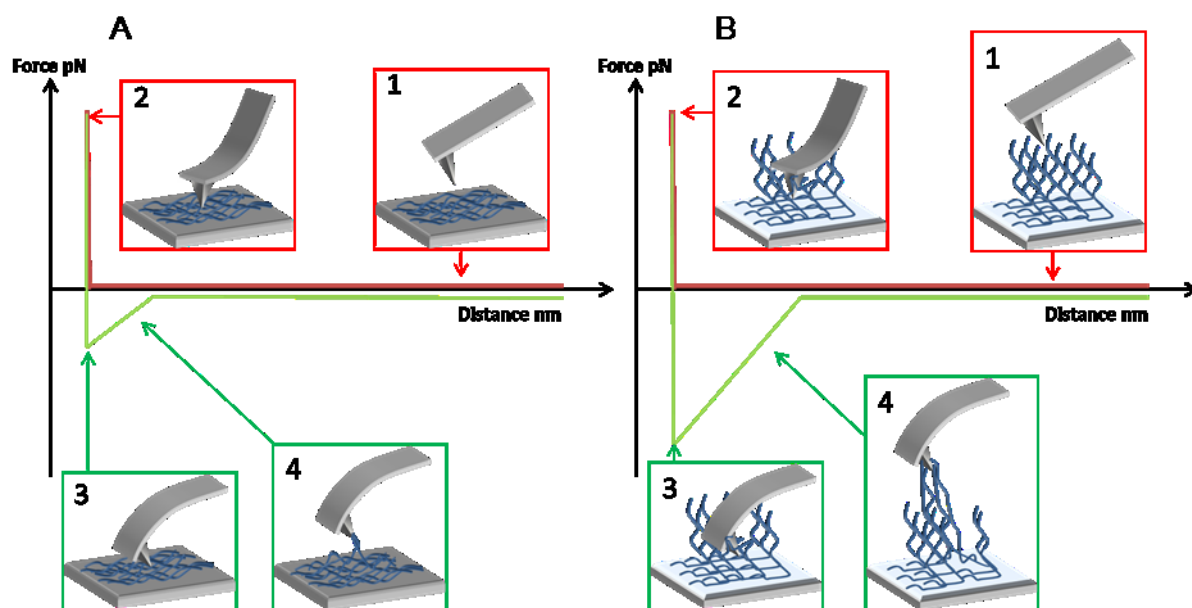


Figure 2.8: Schematic representation of interaction between protein brushes and AFM tip. Case A: Protein layer with high density presenting a low adhesion value and short sized fibril. Case B: Protein layer with low degree of fibrillation presenting high adhesion value and large fibril.

The adhesion forces or the fibril sizes are not the only information which can be provided by AFM force spectroscopy. In the case of fibrillar proteins the number of rupture events for one fibril gives information about degrees of fibrillation and supramolecular arrangement of protein on the surface. Figure 9 shows a typical force curve with the rupture event of fibrils “unzipping” during the retraction of the tip from the surface. The figure presents two adhesion peak corresponding to step 1 and step 3 when the cantilever is deflected. The step 2 represents the case where the fibril is unzipped, the cantilever returns to the initial position and the measured value for the force is equal to zero. At the end of step 3, the rupture event between the tip and the fibril occurred. The size of the measured fibril corresponds in this case (interaction between the tip and one fibril) to the addition of the d and d' distances.

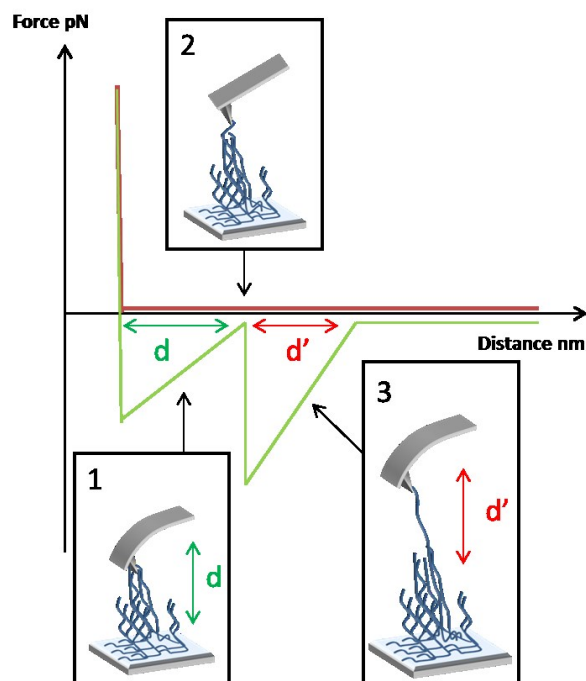


Figure 2.9: Schematic representation of rupture events. Step 1 the cantilever is deflected and a force is measured. Step 2 the cantilever is not deflected and the measured force is equal to zero. Step 3 the cantilever is deflected and a force is measured, then, the rupture event between the tip and the molecule occurs.

In order to make statistical analysis on adhesion percentage, fibril length and rupture events, an adhesion mapping of the sample is necessary: this is the “force-volume” mode. The force-Volume mode consists in measuring and recording for each pixel of the sample image the corresponding force curve as shown on figure 10. In this work all force volume measurements were realized in water with 256 pixels by image (meaning 256 curve forces by image).

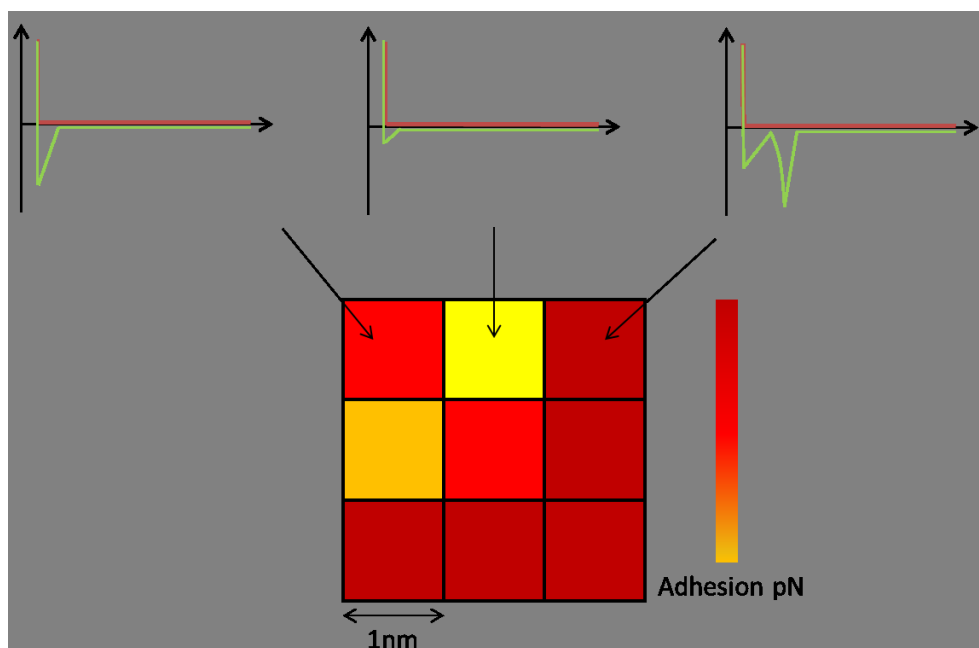


Figure 2.10: Representative schema of Force volume image. To each pixel corresponds one force curve, the obtained image is a mapping of the adhesion force with unit in pN, increasing from yellow to dark red.

f. Experimental conditions

AFM images were recorded using a commercial AFM (NanoScope VIII MultiMode AFM, Bruker Nano Inc- Nano Surfaces Division, Santa Barbara, CA.) equipped with a $150 \times 150 \times 5 \mu\text{m}$ scanner (J-scanner). Images were recorded either in air or in liquid phase (PBS buffer). For this purpose, a quartz fluid cell was used without the O-ring. The silicon wafers were fixed on a steel sample puck using adhesive tape. The mounted samples were immediately transferred into the AFM liquid cell taking care to avoid dewetting. Images were recorded in peak force tappingTM mode at room temperature ($\sim 22\text{-}24^\circ\text{C}$) using oxide-sharpened microfabricated Si_3N_4 cantilevers (Bruker Nano Inc- Nano Surfaces Division, Santa Barbara, CA.). The spring constants of the cantilevers were measured using the thermal noise method, yielding values ranging from 0.40 to 0.45 N/m (figure 11 A). The curvature radius of silicon nitride tips was about 3 nm (manufacturer specifications). All images shown in work are flattened raw data.

Force-distance curves were performed at room temperature ($\sim 22\text{-}24^\circ\text{C}$) in PBS using a Nanoscope VIII Multimode AFM from Bruker Corporation (Santa Barbara, CA) and microfabricated Si_3N_4 cantilevers (MSCT from Bruker Corporation, figure 11 B) with a nominal spring constant of $\sim 0.01 \text{ N/m}$ (as determined by the thermal noise method). The curvature radius of silicon nitride tips was about 30 nm (manufacturer specifications) All force curves were obtained using a maximum applied force of 400 pN and approach and retraction speeds of 1000 nm/s. Unless stated otherwise, a contact time (surface delay) of 500 ms was applied between tip approach and tip retraction, while keeping

constant the maximum applied force. Force-distance curves were acquired at least on three different areas of the sample, for each area ($4\ \mu\text{m} \times 4\ \mu\text{m}$), 256 curves were recorded with a scan rate of 3 Hz.

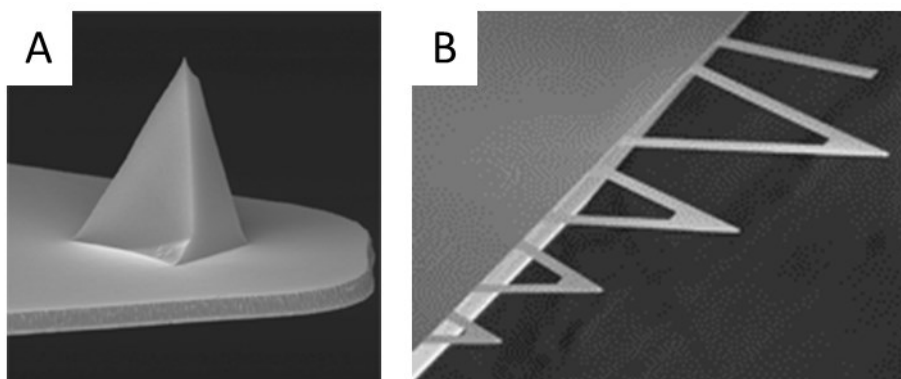


Figure 2.11: AFM probes. A: Tip used in PFT mode imagery. B: probes used in force volume measurement.

Appendix I

Spin coating of silicon wafers:

Solution for spin coating was obtained on dissolving polystyrene blocks in anhydrous toluene. Different tests were performed on temperature of dissolution and polymer concentration to obtain a homogeneous layer. Figure S1 shown the characterization by AFM of spin coated surface in liquid. Solution at 10g/L of PS was dissolved in anhydrous toluene during 5h at 50C°.

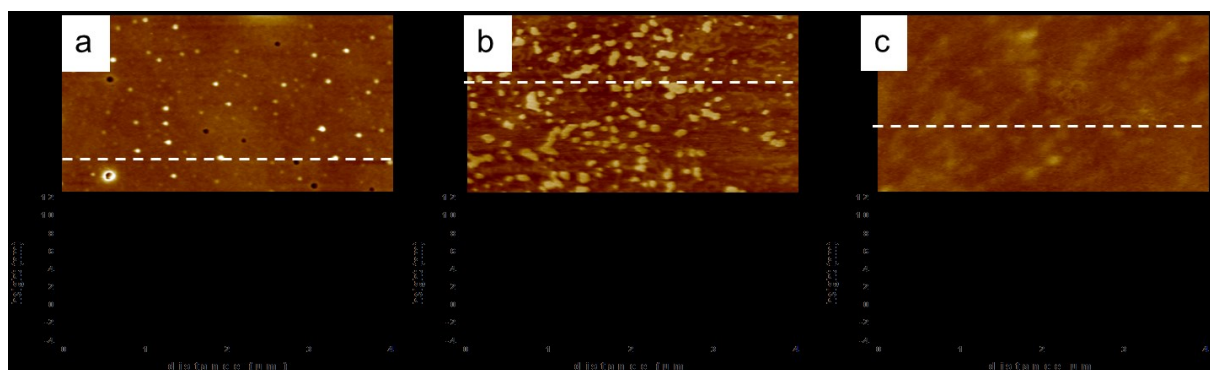


Figure S1: AFM image, PFT mode in water Mq, Zscale :-10/10 nm, image scale 4 μ m*2 μ m. (a) correspond to solution at 10g/L of PS dissolving in anhydrous toluene during 5h at ambient temperature, (b) correspond to solution at 20g/L of PS dissolving in anhydrous toluene during 5h at ambient temperature, (c) correspond to solution at 10g/L of PS dissolving in anhydrous toluene during 5h at 50C°. Cross sections were taken at the location indicated by dashed lines.

Appendix II

XPS device:

Figure S2 gives a schematic representation of the XPS device. The surface sample is submitted to an irradiation by X-ray flux. Then, the emitted photo-electrons from the surface sample are captured by a hemispherical electron energy analyzer. This last is composed by two hemispherical electrodes; electrons are linearly dispersed in function of their kinetic energy. The separation of electrons depends on the chosen E_{pass} . Low pass energy improves the resolution, but decreases the probability of electron transmission and consequently the signal-to-noise is deteriorated. The electrostatic lens in front of the analyzer collects and focuses the electrons.

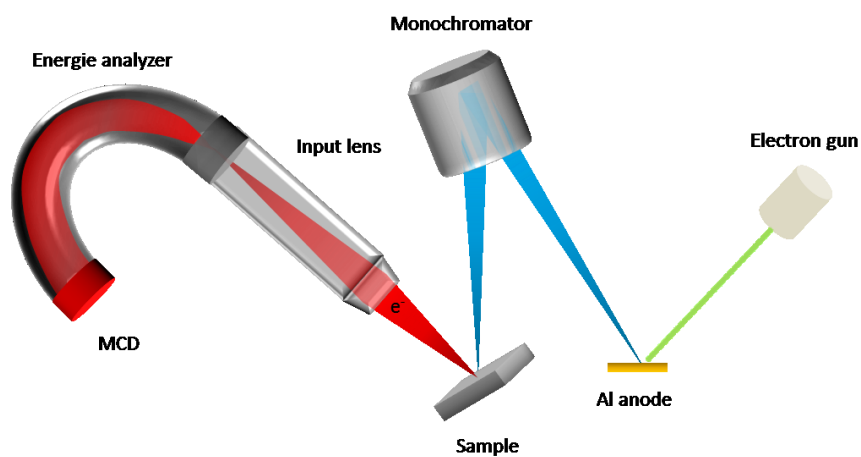


Figure S2: XPS instrumentation

Appendix III

ATR device:

Figure S3 gives a schematic representation of the liquid ATR device. IR beam is subjected to one or more reflections at the interface between a transparent material in the IR domain possessing a high refractive index (such as ZnSe), and the sample in contact with the ATR crystal (protein solution in this case). For angles superior at a critical angle the beam is totally reflected. At each reflection, an evanescent wave is generated at the interface; and penetrates slightly into the sample with a depth penetration (D_p) which depends on the refractive indices of the sample. The collected signal comes from the analyzed thickness, which can be described by the energy of the evanescent wave by the following equation: $E = E_0 \exp^{(-z/D_p)}$.

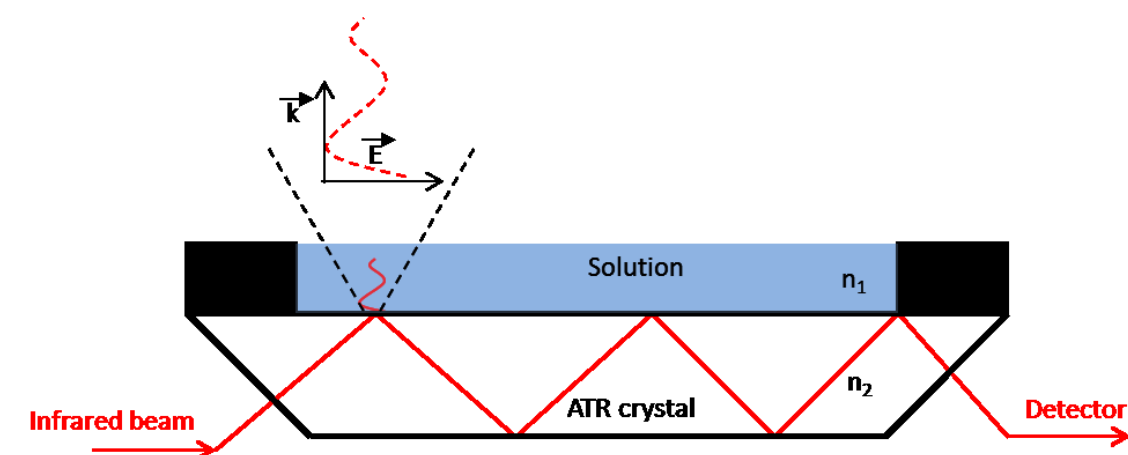


Figure S3: liquid ATR device

Appendix VI

UV absorption:

To measure the catalytic activity of TiO_2 NPs (formation of ROS species) a test consists of monitoring the bleaching of organic molecules (chromophores) such as the blue methylene (BM). Free radicals provide the reduction of blue methylene (BM), the solution goes from blue to uncolored. This effect is measured by UV absorption of the solution at 660 nm. Figure S4 shows the absorption spectrum of BM as well as the calibration curve of BM absorption.

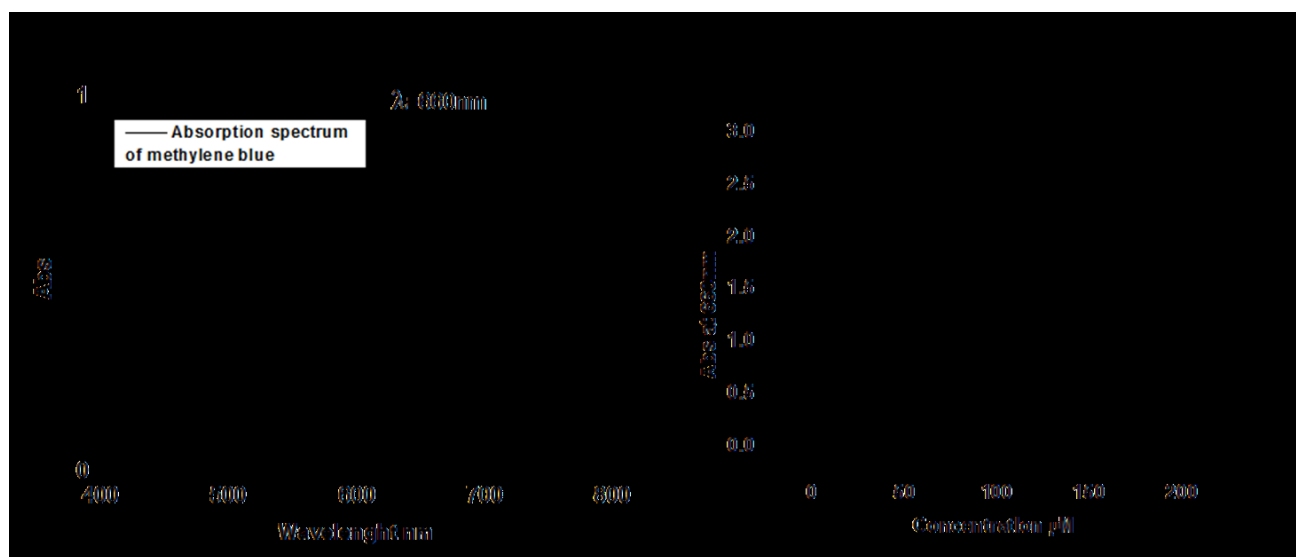


Figure S4: (A) Absorption spectrum of BM, (B) Evolution of the absorbance (at 660 nm) as a function of MB. In this work only absorbance corresponding to concentrations ranging from 0 to 50 mg/L were only considered (linear portion of the curve).

Chapter 3: Properties and fate of sphere and rod-shaped TiO₂ nano-crystals in buffer solutions simulating biological fluids: Mechanism of interaction with phosphate species

Table of contents

Chapter 3: Properties and fate of sphere and rod-shaped TiO₂ nano-crystals in buffer solutions simulating biological fluids: Mechanism of interaction with phosphate species.....	85
I. Introduction.....	87
II. Synthesis and characterization of the TiO ₂ NPs.....	89
III. Catalytic properties in phosphate buffer	94
IV. Behavior in aqueous media	96
V. Catalytic properties in phosphate buffer saline (PBS).....	102
VI. Behaviour in PBS	102
VII. Conclusion	104
VIII. References	105

I. Introduction

One of the key points to understand the protein-NPs interaction is to know what the proteins “sees” in solution. This chapter focuses on the behavior of titanium dioxide (TiO₂) NPs (NPs) in buffer solution especially on the NPs-NPs interaction in order to describe and explain the potential interaction with biomolecules at physiological condition of ionic strength and pH. In a first time, the synthesis of size-controlled TiO₂ NPs with spherical or rod-like shapes and various aspect ratios is described. These NPs are then used for the rest of the study, their main characteristics are investigated such as morphology and crystallinity. Their catalytic properties in solution were assessed in solutions simulating biological fluids, then, the effect of the particles shape on their aggregation and sedimentation was investigated in phosphate buffer solutions saline (PBS) and non-saline at different ionic strength and composition.

TiO₂ NPs have been used in a wide range of nanotechnology areas such as in packaging and paint industries, environmentally friendly energy, sensing devices, etc.¹. The wide use of these metal oxide materials is mainly due to their remarkable features, especially optical- and electronic-related^{1,3}. During the last decade, the fate and behavior of TiO₂ NPs in aqueous media have been the subject of a vast literature. The many papers published related to this issue can be roughly divided into three categories: (i) articles describing the behavior of TiO₂, among other metal oxide nanomaterials, in natural waters and examining the possible environmental impacts (see^{4,5} and references therein), (ii) articles reporting the toxic effects induced by TiO₂ NPs (sometimes polemical), with a particular attention to interactions with biological systems (cells and biomolecules)⁶, and (iii) papers presenting procedures for the elaboration and utilization of TiO₂ NPs in nanomedicine and biosensing applications⁷⁻⁹. Indeed, these nanomaterials have the ability to produce reactive oxygen species (ROS) under ultraviolet and ultrasound irradiations or under other special conditions¹⁰ and to easily cross biological barriers, including skin, lung, and intestine¹¹. Therefore, TiO₂ NPs may generate oxidant stress by disturbing specific functions of cells and may alter the structures of biomolecules, such as proteins and DNA¹². At the same time, these catalytic properties make TiO₂ NPs an efficient candidate for photodynamic cancer therapies¹³. All these studies persuaded the need to better understand the fate and transport of TiO₂ NPs in aqueous media with biological interest and their interaction with inorganic constituents of buffer solutions¹⁴⁻¹⁸.

Interestingly, the remarkable physical and chemical properties of TiO₂ do not only depend on the crystal phase (amorphous, anatase, rutile, brookite) and particle size, but they are also influenced by particle shape¹⁹. This parameter is in fact a useful tool to modulate electronic states²⁰, although with the possible consequences of affecting the behavior of the NPs in aqueous media, which is

recognized but almost neglected in research studies. Tuning the shape of TiO₂ NPs is therefore of key importance in the fabrication of new advanced materials with desired properties and functions. Over the past decades, there have been a number of synthetic routes for the preparation of TiO₂ NPs with tuned size and shapes. The most commonly methods include micelles and inverse micelles²¹, sol-gel²² and nonhydrolytic sol-gel^{23,24}. The main disadvantage of these methods lies in the need of a prolonged heat treatment (calcinations) to achieve crystallized states^{25,26}. In addition, some methods require the use of surfactants which are often toxic, and thus their utilization is significantly restricted in many applications. As an alternative, the solvothermal method is a one-step procedure not requiring the use of surfactants. This method is versatile and may lead to the synthesis of TiO₂ NPs with controlled size and shape²⁷.

The synthesized TiO₂ NPs with different shapes and aspect ratios were characterized by TEM and XRD in order to determine and characterize their morphology and crystallinity. Their chemical catalytic properties were investigated by UV absorption by monitoring the bleaching of methylene blue in the presence of peroxide hydrogen specie in water and PBS buffer. The behavior of NPs in aqueous solutions simulating biological fluids condition of pH and ionic strength was investigated. For this purpose, the effect of the particles shape on their mobility, aggregation and sedimentation was assessed in phosphate buffer solutions at different ionic strengths and composition by means of electrophoretic mobility measurements and light-scattering-based techniques. Then, regarding the obtained information in PBS and phosphate buffer a postulate on the chemical species on the particles surface has been provided in order to explain the different observed on dispersive effect on nano-rods and nano-sphere and to determine the process involved in particle-particle interactions.

II. Synthesis and characterization of the TiO₂ NPs

The non aqueous-solvothermal method used in this study for the synthesis of TiO₂ NPs is based on the “benzyl alcohol route” reported by Niederberger *et al.*^{28,29}, however, by performing slight modifications. The potentiality of the method to tune NP shape by varying the concentration molar ratios of the reagents, i.e., BzOH/TTIP and AA/BzOH, which is expected to control the rate of water in the reaction system, was assessed (Figure 1). Figure 1 shows the representative TEM images of the synthesized TiO₂ NPs and reveals the formation of nano-objects with different shapes and sizes dependent on the BzOH/TTIP and AA/BzOH molar concentration ratios. Spherical particles are formed in the absence of AA (Figures 1A and 1B), whereas in its presence rod-like particles start to be formed (Figures 1C-H). The length of the formed rods is dependent on the AA concentration; the increase of AA/BzOH molar ratio from 0.07 to 0.34 and maintaining a fixed BzOH/TTIP ratio (14.24) resulted in longer nanorods (*ca.* 11 and 18 nm, respectively; Figures 1C and 1D). Also, Ciccarella *et al.*³⁰ showed the effect of AA on the size and shape of TiO₂ NPs under milder conditions (180 °C, reaction time ~ 18 h).

Figure 2 shows the size distributions of NPs, which were determined from the TEM images by considering the diameter for sphere-shaped NPs, and both width (diameter) and length for rod-shaped NPs (Figures 2A and B). The produced nano-spheres have a narrow size distribution, with a mean of 7.6 ± 1.3 nm, whereas a slightly larger size distribution was obtained for the nano-rods: width of 7.8 ± 0.8 nm and length of 21.8 ± 2.6 nm.

The effect of the molar concentration of AA/BzOH on the length of the produced nano-rods (Figure 2C) is in fact noticeable; an increase of the aspect ratio from ~1 to ~3 is obtained when increasing the AA/BzOH molar concentration ratio from 0.07 to 0.45. Also the molar concentration ratio of BzOH/TTIP seems to affect the growth of the nano-rods since a decrease from 14.24 to 7.12 results in rods with length larger than 20 nm. However, the variations are not great enough to conclude about a clear effect of the BzOH/TTIP molar ratio. Interestingly, for all different reagents ratios the growth of the nano-rods occurs by keeping the cross-sectional area almost unchanged indicating a well-controlled synthesis of the nano-rods. This behavior is shown through the diameter and width size distributions in Figures 2A and 2B, respectively, and further evidenced by the evolution of the NP length at nearly fixed width, which is in fact similar with the diameter size of the sphere-shaped NPs (Figure 2C and D).

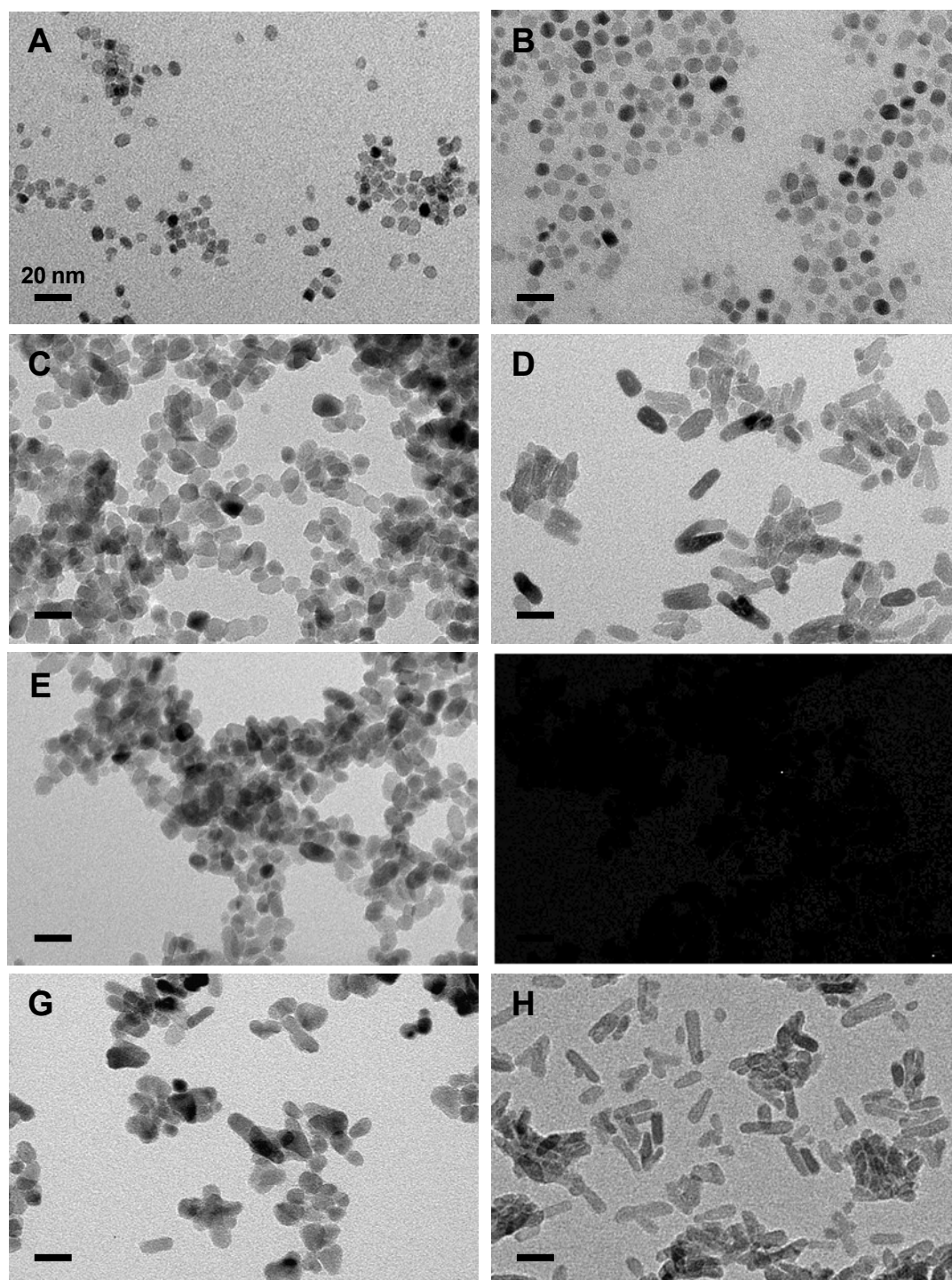


Figure 3.1: TEM micrographs of TiO₂ NPs synthesized (A-B) without AA using BzOH /TTIP molar concentration ratio of (A) 7.12; (B) 14.24; or (C-H) in the presence of AA using BzOH /TTIP ratios of (C, D) 14.24; (E, F) 11.42; (G, H) 7.12 and AA/BzOH molar concentration ratios of (C) 0.07; (D) 0.34; (E) 0.11; (F) 0.45; (G) 0.10; (H) 0.36.

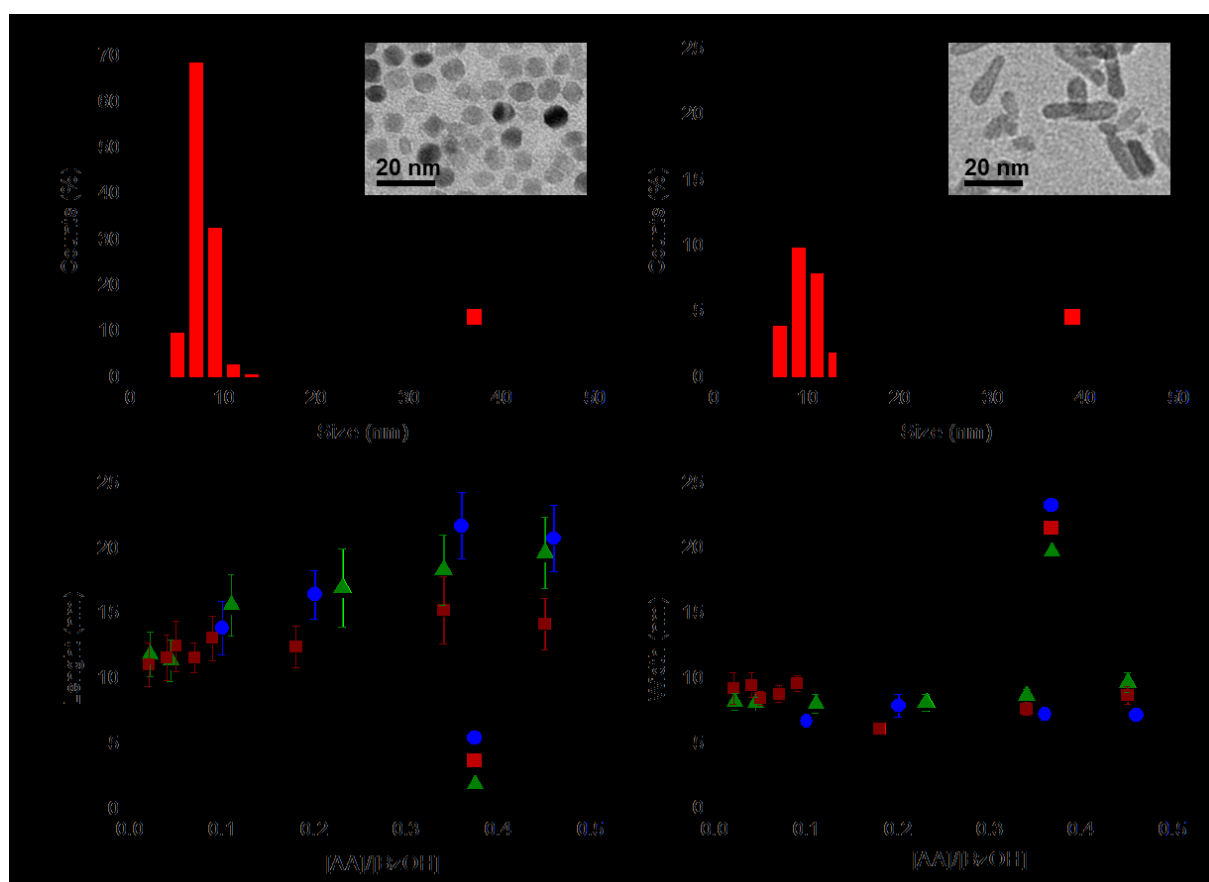


Figure 3.2: Size distributions of the (A) sphere- and (B) rod-shaped TiO₂ NPs determined from the TEM micrographs. (C) Evolution of the nano-rods length and (D) evolution of the nano-rods width as a function of the molar concentration ratio AA/BzOH at a BzOH/TTIP molar concentration ratio equal to 7.12; 11.42 or 14.24 (as indicated).

The crystallographic properties of the TiO₂ NPs with aspect ratio of ~1 (nano-spheres) and ~3 (nano-rods) were assessed by XRD (Figure 3). Both shapes of the TiO₂ NPs show well-defined peaks assigned to pure anatase, also suggesting a high crystallinity of the samples. Indeed, the peaks correspond to diffraction from the (101), (004), (103), (200), (105), and (211) planes of anatase with no other phases detected. The characteristic line broadening of the diffraction peaks is due to the nano-sized nature of the anatase crystals. In addition, the (004) diffraction peak of nano-rods is stronger and sharper than that of nano-spheres, reflecting the evolution along the [001] direction, c axis, of the anatase lattice.

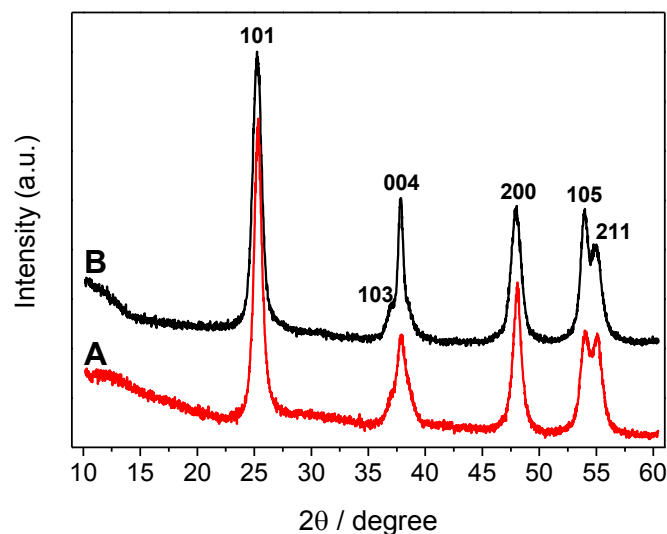


Figure 3.3: XRD patterns of TiO₂ (A) nano-spheres and (B) nano-rods.

Further crystallographic features of both TiO₂ shapes were obtained by HRTEM as shown on figures 4 and 5. Inter reticular distances were measured by two methods: (i) Fourier transforms of the high-resolution image, and (ii) intensity line profiles. The nano-spheres show lattice planes distancing by $d_{101} = 3.51 \text{ \AA}$ and $d_{004} = 2.37 \text{ \AA}$. For nano-rods it is observed that the growth occurs along the crystallographic *c* axis, which is indeed consistently shown by the plan [101], corresponding to a distance of 3.51 \AA , that is at an angle of 22° to the axis of the nanorods (Figure 5). This is in fact in accordance with a *c*-axis parallel to the nano-rod axis as illustrated by the elementary calculation: $\tan^{-1}(a/c) = 21.7^\circ$ (Figure S1, appendix). This is the most frequently analyzed configuration, because the [101] planes have the largest inter-reticular distances in this structure, and are, thus, easily highlighted by HRTEM. Though, it was also possible to analyze the [004] plans corresponding to 2.73 \AA inter reticular distance, which were found perpendicular to the rods axis. These findings are confirmed by other HRTEM micrographies (an example is given in Figure S2, appendix). It is worth noticing that the fact that the same d_{101} and d_{004} distances were found for both shapes, nano-spheres and nano-rods, confirms their identical structure. For nano-spheres, i.e. in the absence of AA, it appears that growth along the *c*-axis is not favored.

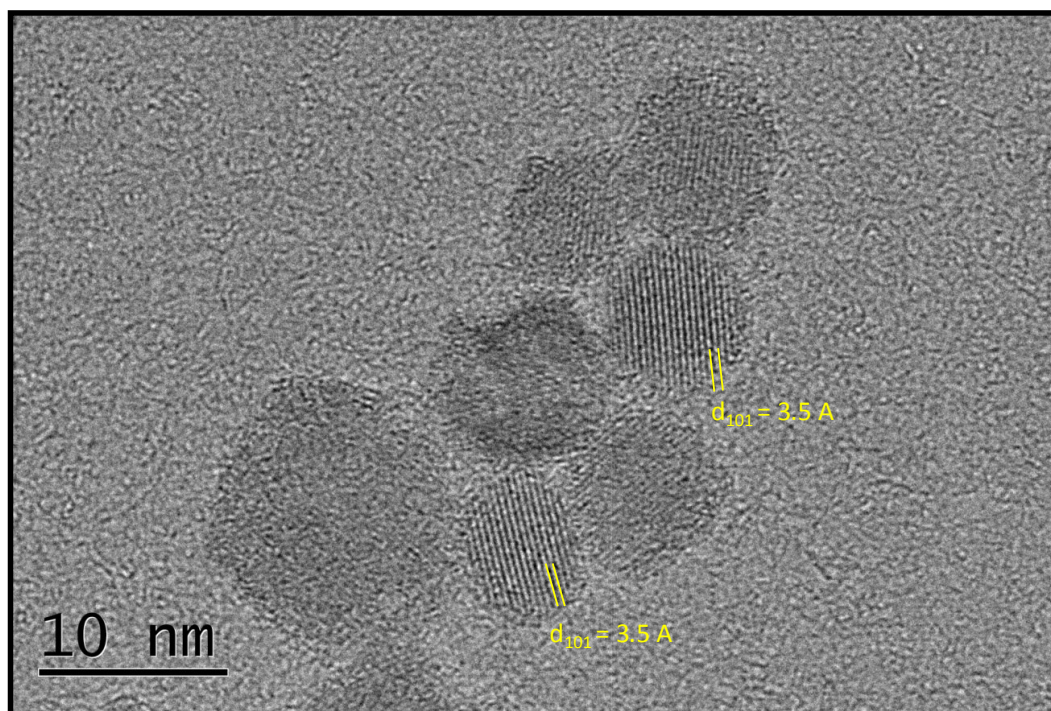


Figure 3.4: HRTEM micrograph of TiO₂ nano-spheres. Inter reticular distances were measured from FFT and line profile.

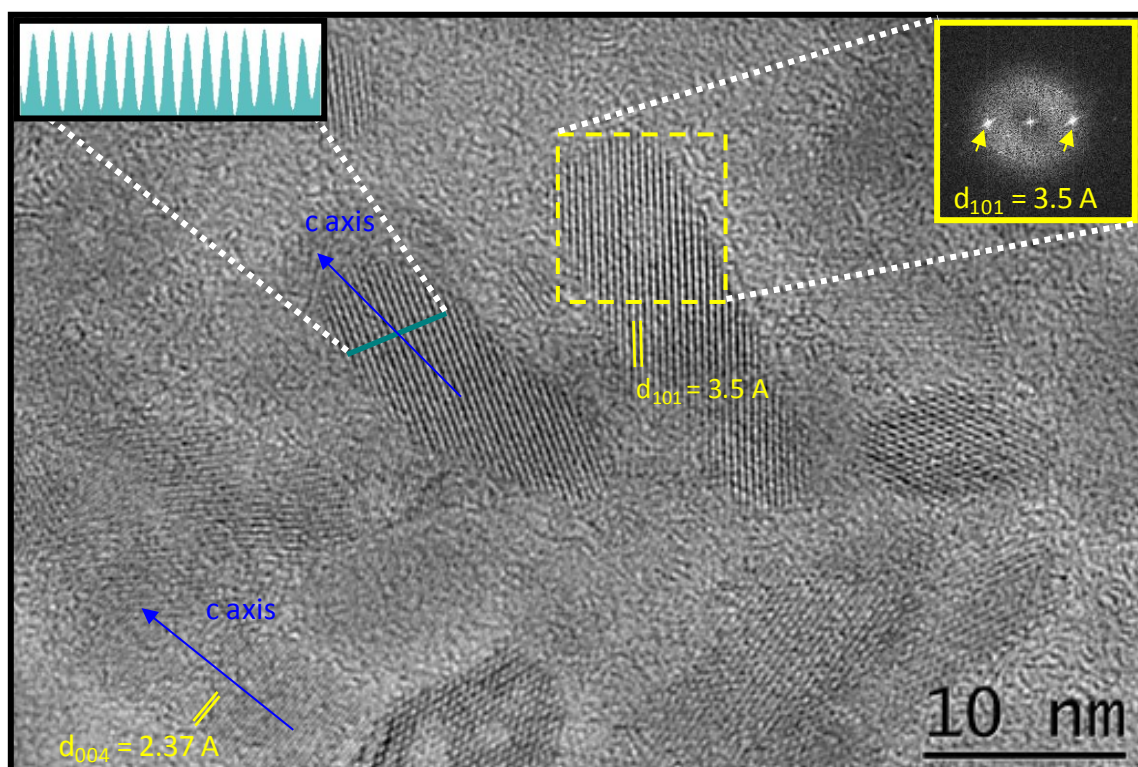


Figure 3.5: HRTEM micrograph of TiO₂ nano-rods. The orientation of crystallographic plans, identified by inter reticular distances measurements from FFT and line profile, is consistent with a growth along the c-axis.

The elongation of the TiO₂ NPs with increasing amount of AA is most probably due to the anisotropic crystal growth³⁰, which likely involves two main steps: (i) hydrolysis of the titanium precursors to produce unstable hydroxylalkoxides, and (ii) subsequent condensation reactions by means of oxolation to form Ti-O-Ti²⁴. As a consequence, solvent plays a key role since the chemical modification of titanium isopropoxide by the solvent molecules allows the control of the precursor reactivity enabling isotropic or anisotropic growth of the NPs. The rates of these two processes dramatically affect the shape of the final nano-objects. Therefore, the rate control of these growth processes is essential for tuning the shape evolution of the TiO₂ particles. In the system studied, the TiO₂ formation reaction, when TTIP is added to pure BzOH, is not strictly non-hydrolytic due to the presence of water from the etherification reaction between the alcohol molecules³⁰. The water produced promotes an alkoxide group exchange reaction forming terminal hydroxyl groups. Consequently, the formation of the Ti-O-Ti bridges occurs through the polycondensation reactions between alcoholic or hydroxyl ligands coordinated to two different titanium centers. When TTIP is added to a mixture of BzOH and AA another important process takes place that results in the production of water³. This process is the direct esterification reaction between BzOH and AA with the elimination of benzyl acetate, which is also able to confine the crystal growth.

These findings indicate the relevancy of the procedure used to elongate the sphere-shaped TiO₂ NPs in a well-defined crystallographic direction, resulting in the formation of highly crystalline rod-shaped particles with identical structure and cross-sectional area as nano-spheres. The studied system is thus suitable to exclusively investigate the shape effect of TiO₂ NPs on their properties and their behavior in aqueous media with biological interest.

III. Catalytic properties in phosphate buffer

The catalytic properties of both TiO₂ shapes were assessed through their ability to generate radicals in aqueous solutions containing hydrogen peroxide (H₂O₂) without any external UV irradiation. The generation of radicals was monitored by the bleaching of methylene blue (MB), in ultrapure water (MilliQ) or in phosphate buffer solutions (0 or 154 mM NaCl corresponding to the Sigma tablet concentration) containing 100 µg/mL of TiO₂ NPs and H₂O₂ (3%). Figure 6 shows the Evolution of the fraction of methylene blue bleaching in the presence of nano-spheres or nano-rods of TiO₂ in ultrapure water. When NPs are dispersed in ultrapure water a significant bleaching of MB is observed in the presence of both nano-spheres and nano-rods; yielding values around 0.3 (Figure 6). These results indicate the generation of a significant amount of radicals through the catalysis of H₂O₂

reaction reduction by TiO₂ NPs in a similar way as in a Fenton reaction¹⁰. The MB bleaching strongly depends on the concentration of NPs (higher bleaching with the increase of the particles concentration) regardless of the NP shape (sphere or rod). Moreover, an increase of the H₂O₂ concentration results in an enhanced MB bleaching, independently of the particles concentrations and shape (Figure S3, appendix).

The obtained effect with the increasing of the H₂O₂ or TiO₂ NPs concentrations, which are the reagent and the catalysts, respectively, is consistent with the prediction of chemical-catalyzed reactions, i.e., results in the generation of a higher amount of radicals, which validates the relevancy of this experimental procedure. It appears that no clear trend can be established regarding the reactivity of NPs as a function of their shapes. At the highest concentration of NPs (1.0 mg/ml), nano-spheres cause more MB bleaching than nano-rods, whereas at the lowest NP concentration (0.01 mg/ml) the tendency is inverted. Besides, at the intermediate concentration (0.1 mg/ml), both trends are observed, depending on the concentration of H₂O₂ in the solution (Figure S3, appendix).

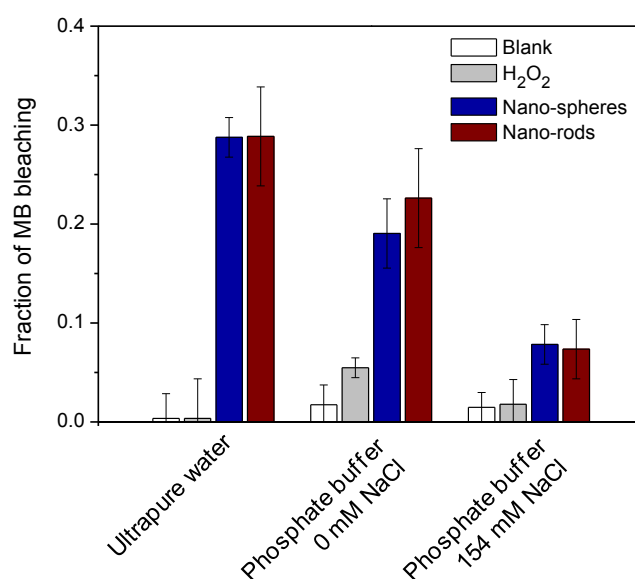


Figure 3.6: Evolution of the fraction of methylene blue (MB) bleaching for nano-spheres or nano-rods of TiO₂ dispersed in ultrapure water or in phosphate buffer solutions (30 mM NaH₂PO₄ + 70 mM Na₂HPO₄) in presence of different concentrations of NaCl (as indicated) at a concentration of 154 µg/ml and pH=7.2.

In phosphate buffer solution (30 mM NaH₂PO₄ + 70 mM Na₂HPO₄) without NaCl, a noticeable lowering of the catalytic activity of TiO₂ NPs is observed and the fraction of MB bleaching remains around 0.2 (Figure 6). The addition of NaCl (154 mM) to the phosphate buffer solution leads to a considerable decrease of the catalytic activity of both sphere and rod-shaped NPs. In the latter case, the fractions of MB bleaching are under 0.1. The effect observed in phosphate buffer solutions may be due to the adsorption of phosphate ions onto the TiO₂ surface blocking the electron transfer from MB, as also observed for photocatalytic properties (see appendix II figure S3).

IV. Behavior in phosphate buffer saline

In aqueous media, the homoaggregation of NPs strongly impacts their reactivity and fate³¹, and also the mechanism of interaction with the biological systems³². Although homoaggregation of TiO₂ NPs has been the subject of a large number of papers, their aggregation state remains difficult to be predicted since it can be affected by both intrinsic properties of the particles (size, shape, cristallinity, etc.) and external parameters related to the medium composition (type of ions, ionic strength, pH, etc.). In fact, the effect of particle morphology on their behavior is being almost neglected and a very limited number of articles can be found in the literature³³.

Figure 7 shows DLS measurements of the nano-spheres and nano-rods dispersed in phosphate buffer with different NaCl concentrations. A shape effect is evident with the increasing addition of the monovalent salt (NaCl); aggregates with lower sizes are formed for nano-spheres (*cf.* Figures 7A) comparing to nano-rods (*cf.* Figures 7B). For example, in presence of the highest NaCl concentration the nano-spheres aggregates have a mean size of 68 nm whereas the nano-rods form aggregates with mean values of 164 nm. Indeed, the nano-spheres show stronger ionic strength ($I = \frac{1}{2} \sum C_i z_i^2$) dependence than nano-rods. The nano-spheres aggregate sizes decrease from 531 nm in absence of NaCl ($I = 240$ mM) to 68 nm in presence of 154 mM NaCl ($I = 394$ mM), whereas a decrease of 178 nm was obtained for the nano-rods under the same conditions of ionic strength and composition. This I dependence was also observed by Zhou and Keller for nearly spherical ZnO NPs, while a mixture of slab-like and rod-shaped ZnO NPs showed minimal influence of I (0.1 to 750 mM NaCl)³³. In the present work, the remarkable effect is the decrease of the mean diameter of the aggregates with the increase of the I by maintaining the phosphate concentration constant (i.e., increasing the NaCl concentration).

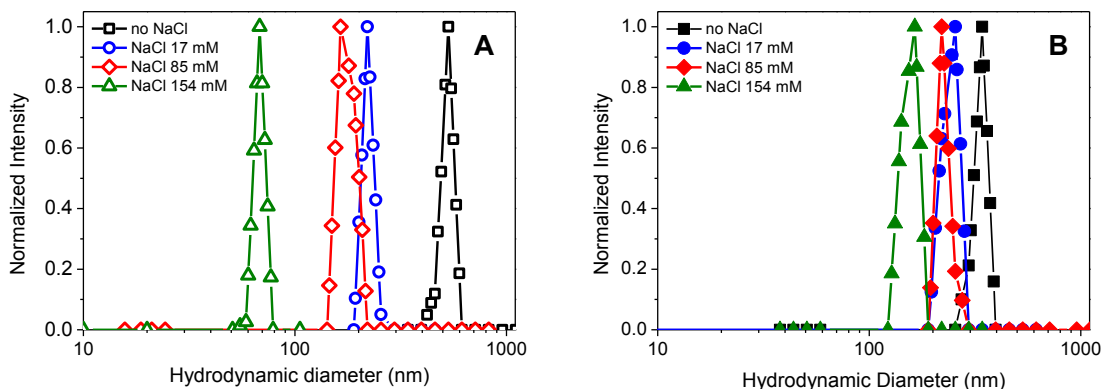


Figure 3.7: Intensity-normalized particle size distributions obtained from DLS measurements performed for 0.1 mg/mL of TiO₂ (A) nano-spheres and (B) nano-rods dispersed in phosphate buffer solutions (30 mM NaH₂PO₄ +

70 mM Na₂HPO₄) in presence of different concentrations of NaCl (as indicated). Measurements were performed after 24 h of exposure at room temperature in dark conditions.

Sedimentation tests show that both nano-spheres and nano-rods start to sediment in few minutes independently of the NaCl concentration (Figure 8). However, sedimentation is in fact slightly more pronounced for nano-rods suspensions than for nano-spheres, independently of the absence or presence of the monovalent salt. Indeed, the nano-rods aggregates are larger than the nano-spheres aggregates when in presence of the NaCl (Figure 7). The increase of I by addition of NaCl results in a decrease of the sedimentation rate, which is more pronounced for the nano-spheres (within the experimental error; Figure 8), in agreement with the DLS data obtained (Figure 7). It is worth reminding that the sedimentation phenomenon occurs due to the fact that gravitational forces related to aggregates are prevalent regarding the buoyancy forces. The rate of sedimentation depends on the cross-sectional area and/or the density of the aggregates in solution.

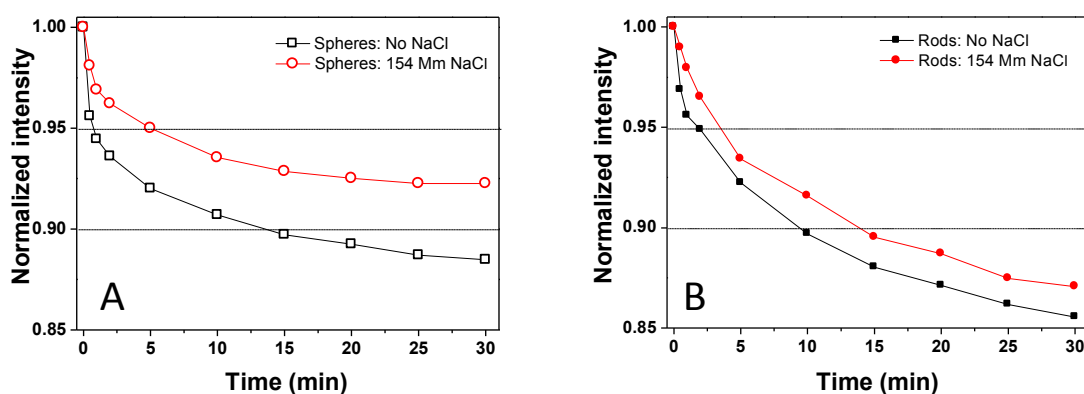


Figure 3.8: Sedimentation plots of 1 mg/mL suspensions of TiO₂ (A) nano-spheres 0mM NaCl and 154mM NaCl (B) nano-rods 0mM NaCl and 154mM NaCl, freshly dispersed in phosphate buffer solutions (30 mM NaH₂PO₄ + 70 mM Na₂HPO₄).

TEM images recorded on TiO₂ NPs after their dispersion in buffer solutions also show an efficient dispersion of the nano-spheres with the increase of NaCl concentration (Figures 9A to 9D), whereas for nano-rods only a slight dispersion effect was observed (Figures 9E to 9H). These observations are in fact in accordance with the DLS and the sedimentation data (*cf.* Figure 7 and Figure 9; larger sedimentation and aggregate sizes for nano-rods and larger I effect for nano-spheres).

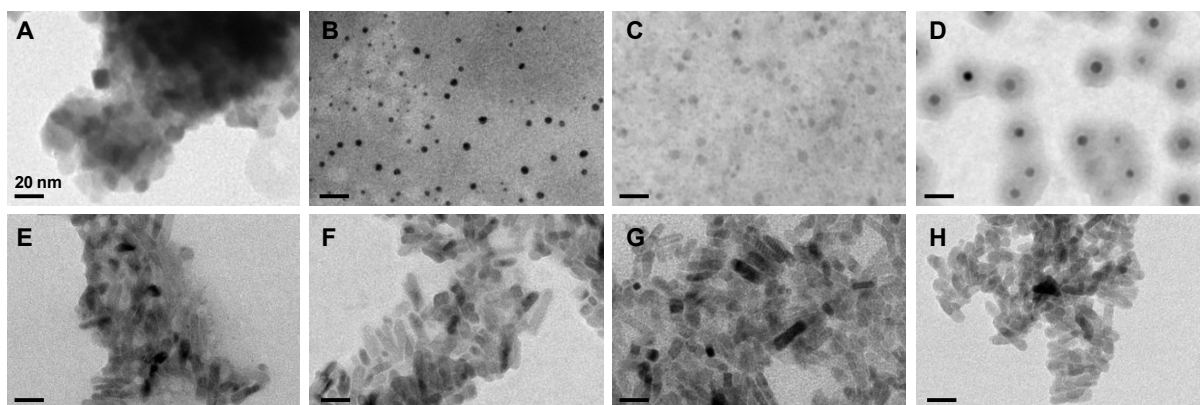


Figure 3.9: TEM micrographs of TiO₂ (A-D) nano-spheres and (E-H) nano-rod after dispersion and further equilibration for 24 h in the phosphate buffer solutions (30 mM NaH₂PO₄ + 70 mM Na₂HPO₄) containing NaCl concentrations of (A, E) 0, (B, F) 17, (C, G) 85 and (D, H) 154 mM.

Particle electrophoretic measurements (EPM) shows less negative values with the increasing of NaCl amount in the phosphate buffer for both TiO₂ shapes (red and blue symbols of Figure 10), in accordance with the postulate that an increase in ionic strength leads to a charge shielding of approaching particles and reduces the effectiveness of the Coulombic repulsion, thus enhancing aggregation in disagreement with the DLS data obtained.

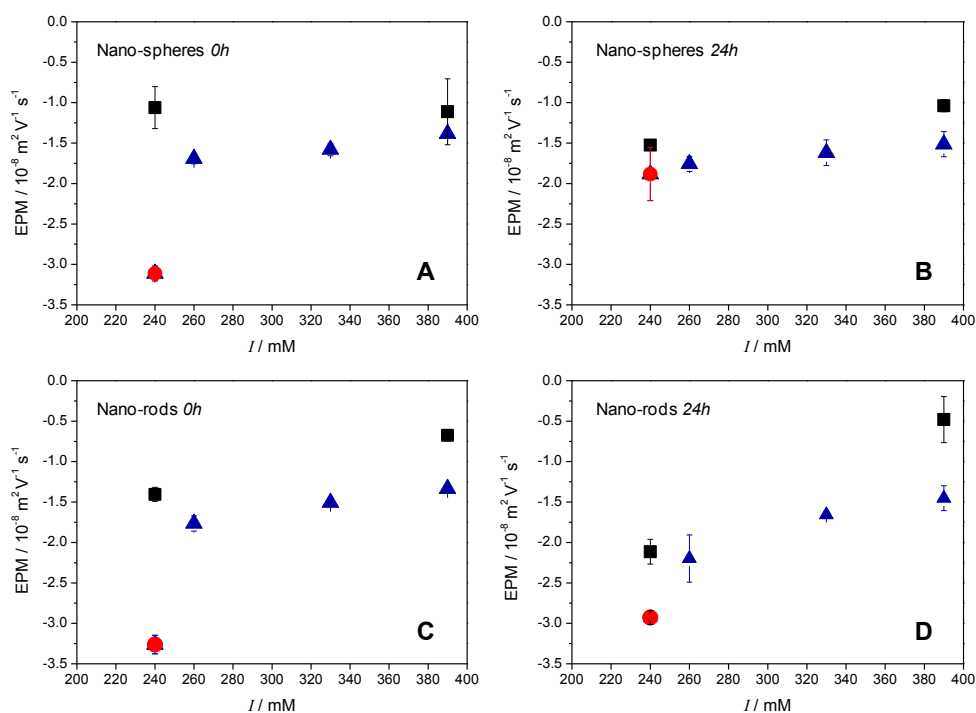


Figure 3.10: Electrophoretic mobilities of the spheres (A, B) and rods (C, D) TiO₂ NPs (0.1 mg/mL) as a function of the ionic strength of the solution at pH 7.4 (± 0.2) immediately after the dispersion in an electrolyte solution (ca. 2-3 min; 0h A, C) or after 24 h of exposure (B, D). The electrolyte solutions used were: (■) NaCl, (●) (30

mM) NaH₂PO₄ + (70 mM) Na₂HPO₄, and (▲) (30 mM) NaH₂PO₄ + (70 mM) Na₂HPO₄ + (17, 85 and 154 mM) NaCl.

These findings point out the complexity of the TiO₂ NPs behavior in these synthetic relevant biological fluids, only containing inorganic constituents, which includes (i) a NaCl effect in the dispersion of the particles in a phosphate buffer, and (ii) a shape effect on the aggregation/sedimentation of the particles. In phosphate buffer, the effect of the ionic strength observed by DLS is opposite to the general trend reported in the literature that postulates an increase of the aggregation with the increase of the ionic strength¹⁵. Generally, the electrostatic stabilization of metal oxide NP suspensions is achieved by increasing the ionic strength, which is consistent with the DLVO theory predictions based on the fact that the aggregation of NPs is governed by van der Waals attractive forces and electrostatic repulsive forces^{34, 35}. Therefore, it should be expected that the addition of NaCl in the medium would result in a decrease of the repulsion forces, due to a compression of the electrical double layer leading to their aggregation. The presence of other components can in fact change this tendency. It was shown, for example, that the adsorption of a fulvic acid on TiO₂ NPs prevents particles approaching through a steric repulsion even when increasing the ionic strength³⁶. In this study, the unexpected effect of ionic strength in phosphate buffer solutions is most probably explained by the adsorption of anionic sodium-phosphate species on the surface of TiO₂ NPs. In fact, VisualMinteq³⁷ calculations show that the increase of NaCl concentration to the phosphate buffer results in a significant increase of the NaHPO₄⁻ specie from 27.4 to 39.0 % (Table 1). Increased NaHPO₄⁻ adsorption did not lead to significantly greater electrostatic repulsion (Figure 10) among the TiO₂ NPs. Therefore, the increased stability of the NPs at high ionic strength is attributed to a greater adsorption of the NaHPO₄⁻ on the TiO₂ resulting from the compression of the diffusive layer around the particles. The adsorption of these polyatomic anions onto the surface of the metal oxide NPs results in an increase of the electrostatic repulsive forces between the particles preventing them from approaching through a steric repulsion and resulting in lower aggregation (Figure 7). The behavioral difference between both shapes, namely the larger aggregation and sedimentation shown by the nano-rods, can be explained by the lower surface to volume ratio of the nano-rods (4× lower than for the nano-spheres) resulting in a decrease of the polyatomic anion adsorption and less size stabilized dispersions. In fact, more negative EPM values were found for rods than for spheres in absence of NaCl (red symbols in Figures 10B and 10D; *cf.* $(-2.93 \pm 0.09) \cdot 10^{-8} \text{ m}^2 \text{ V}^{-1} \text{ s}^{-1}$ for spheres and $(-1.9 \pm 0.3) \cdot 10^{-8} \text{ m}^2 \text{ V}^{-1} \text{ s}^{-1}$ for rods), also resulting in a higher repulsion between the particles and the polyatomic anions. This effect is also observed in the DLS data, where rods in absence of NaCl have lower aggregates sizes

than spheres (*cf.* around 342 nm for rods and 531 nm for spheres). The possible adsorption of these polyatomic atoms was also shown by Zhang *et al.*³⁸ and Erhayem and Sohn³⁹. In fact, Domingos *et al.*⁴⁰ have shown that the electrophoretic mobilities of spherical TiO₂ NPs at pH below or above the pH of the zero point charge become more negative in presence of 1 mM phosphate, indicating the strong adsorption of phosphates onto the particles surface. A similar effect has been reported by Chen *et al.*⁴¹ showing that phosphate adsorption promotes the transportability of TiO₂ NPs in porous sand. The strong adsorption of phosphate was also found for flat TiO₂ surfaces⁴². Despite the importance of phosphate and phosphate salts on the behavior and fate of TiO₂ NPs in ecosystems and in biological fluids, the mode of interaction of these species is still not clearly understood. In the present study, X-ray photoelectron spectroscopy (XPS) analysis performed on TiO₂ NPs prior to and after dispersion in phosphate buffer solutions (0 or 154 mM) and further rinsing with ultrapure water reveal the presence of phosphor in a significant amount. The P 2p peak shows a characteristic contribution due to phosphate species (Figure S4, appendix). This result suggests a strong interaction between phosphate species and the surface of TiO₂ NPs, in agreement with previous findings reported on flat TiO₂ substrate. However, no noticeable differences in the molar concentration of phosphor are observed as a function of the amount of NaCl in the medium (0 or 154 mM).

To our knowledge, in physiological conditions, i.e., pH ~7 (slightly higher than the expected pH_{zpc} of TiO₂ NPs) and higher ionic strengths, a systematic study on the effect of adsorption of phosphate species on the surface of TiO₂ NPs and their impact on the particle aggregation/sedimentation has never been reported. The size stabilization of the TiO₂ NPs with increasing the NaCl concentration in presence of phosphate, according to DLS, sedimentation and TEM analyses, suggests an important synergetic effect between phosphate and Na⁺ species. This effect can also be evaluated by considering the evolution of the Debye layer thickness, κ^{-1} , which strongly depends on the type of electrolyte (valence of ions) and its concentration according to the following equation:

$$\kappa^{-1} = \sqrt{\frac{\epsilon_r \epsilon_0 k_B T}{e^2 \sum n_i z_i^2}} \quad \text{Eq. 1}$$

where n_i and z_i are the number and valence of ions i in the aqueous solution, respectively. The Debye layer thickness should decrease from 3.1 nm at an ionic strength of 10 mM to 0.8 nm at 154 mM. The effect is thus significant on the electric double layer and should cause a decrease of the repulsive electrostatic interaction between particles leading to an increase of the aggregates size³⁶. However, this transformation process is completely inversed by the presence of the polyatomic NaHPO₄⁻ species.

Specie (%)	Phosphate	Phosphate + 17 mM NaCl	Phosphate + 85 mM NaCl	Phosphate + 154 mM NaCl
HPO ₄ ²⁻ + H ₂ PO ₄ ⁻	69.0	67.0	60.1	54.3
NaHPO ₄ ⁻	27.4	29.0	34.6	39.0

Table 3.1: Percentage of ionic species containing phosphate in the buffers used to disperse the TiO₂ NPs obtained by VisualMinteq.

The results suggest that in buffers simulating biological fluids, the effect of ionic strength on the state of aggregation of TiO₂ NPs may involve two antagonist processes that can differ in magnitude depending on the shape of the NPs as depicted in Figure 11. (i) Guarantee of the charge shielding of the TiO₂ surfaces, i.e. a decrease of the Debye layer thickness, and thus a decrease of the repulsion between approaching particles. (ii) Enhancement of the interaction with other constituents of the buffer, namely polyatomic anions (in this study represented by the sodium-phosphate salts), which switch the former process.

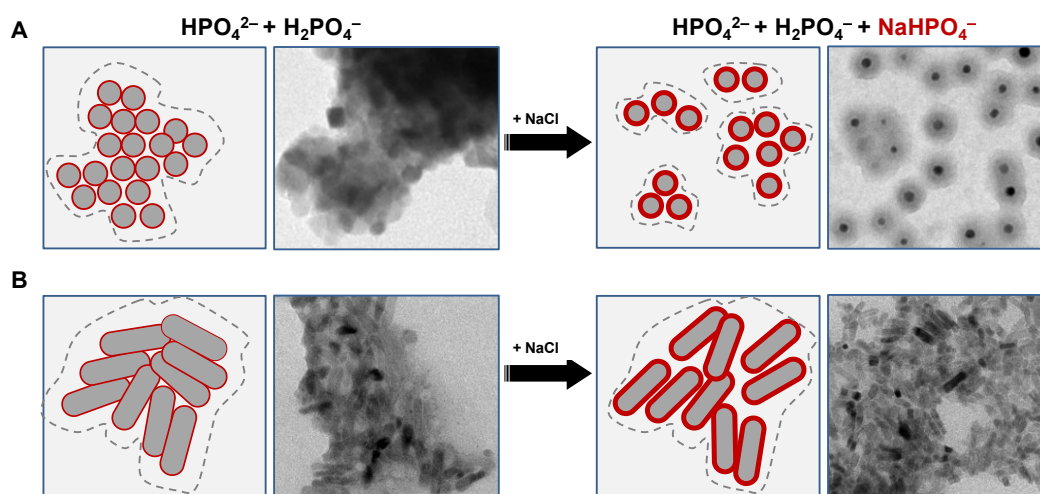


Figure 3.11: Schematic representation showing the state of aggregation of (A) nano-spheres and (B) nano-rods in phosphate buffer in absence and presence of NaCl. The thicker contours around the particles illustrate the presence of NaHPO₄⁻ species resulting in the repulsion between the particles.

The mechanism by which NaHPO₄⁻ specie enhances the repulsion between approaching particles may be either through direct adsorption on the TiO₂ NP surface or due to the fact that these negatively charged species remain around NPs, i.e., located in the electric double layer, and thus enhancing NP repulsion. TEM images reveal the presence of core-shell-like structure for nano-spheres after exposure to the phosphate buffer containing the highest concentration of NaCl (Figure 9D). This

corona may be attributed to the anionic phosphate-sodium complex which is present in the vicinity of NPs surfaces and precipitate upon drying. It is also in agreement with the detection of adsorbed phosphate species by XPS in a significant amount, thus supporting the pivotal role of this species in the dispersion of NPs.

V. Catalytic properties in phosphate buffer saline (PBS)

In PBS solution from Sigma tablet the catalytic properties of TiO₂ nanoparticle presents a similar activity comparing to phosphate buffer with 154mM NaCl such as in figure 6. As previously, the generation of radicals was monitored by the bleaching of MB, the experiments were provided with the same percentage of hydrogen peroxide and without any external UV irradiation in ultrapure water and PBS. Contrary to the previous results in ultrapure water, the bleaching of MB is not increased by the concentrations of TiO₂ NPs (data not shown).

VI. Behaviour in PBS

In order to compare the behavior in aqueous medium and in PBS solution, DLS measurements were provided for the nano-spheres and the nano-rods in PBS solution. Moreover, the effect of temperature (room temperature or 37 °C) was investigated to provide information for the future experiment in the presence of proteins. The observed behavior correspond to behavior of NPs in phosphate buffer for 154 mM of NaCl, no influence of NPs shape is observed (figures 12A and 12B). The data shows that when the NPs are dispersed in PBS solution these last undergo aggregation, with a mean value of 130 and 120 nm for nano-spheres and nano-rods, respectively (at room temperature). A slight variation is observed at the highest temperature (37C°) indicating a negligible effect of the incubation temperature on NPs aggregation.

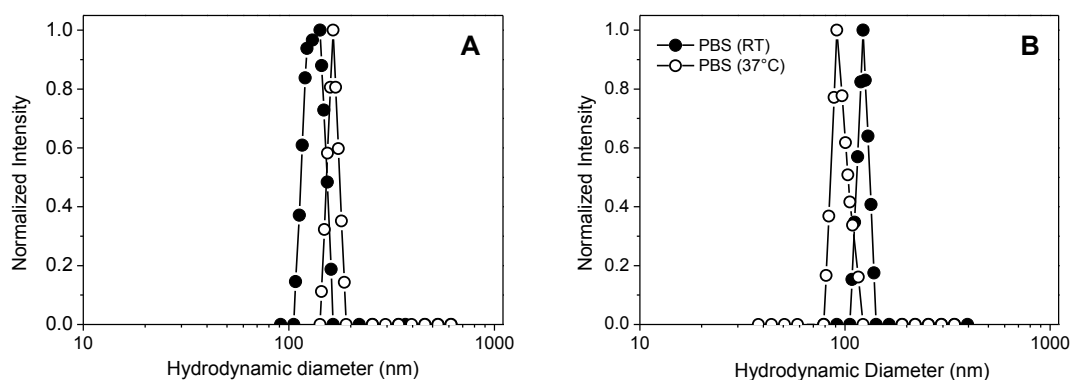


Figure 3.12: Intensity-normalized particle size distributions obtained from DLS measurements performed for 0.1 mg/mL of TiO₂ nano-spheres (A) and nano-rods (B) dispersed in PBS at room temperature (RT) or at 37° (measurements performed after 24 h of exposure).

A lower sedimentation rate is observed in PBS compared to phosphate solution with the highest concentration of NaCl (154 mM) for rods and spheres (figure 13). Therefore, the same trend is observed on the sedimentation rate of nano-rods which is always higher compared to nano-spheres. Suggesting that the aggregates generated by nano-rods are either larger or denser than those formed in nano-spheres suspensions. Such as in phosphate solution the observed difference between nano-rods and nano-spheres may explain by their modality of association during the formation of aggregates.

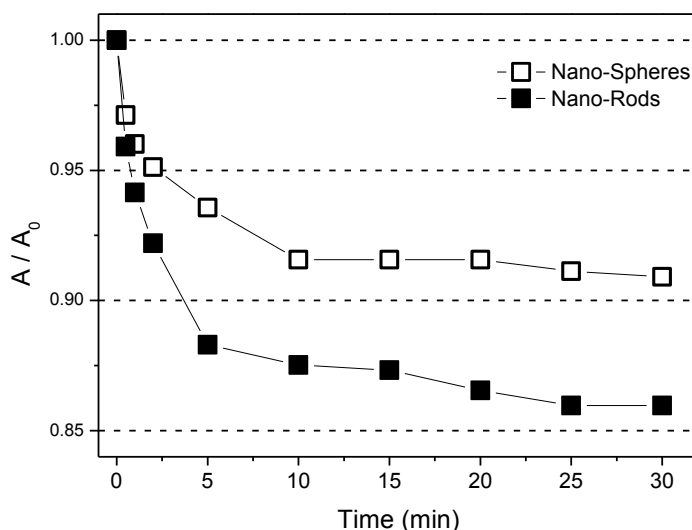


Figure 3.13: Sedimentation plots of 0.1 mg/mL suspensions of TiO₂ nano-spheres (open symbols) and nano-rods (closed symbols) prepared in PBS

VII. Conclusion

In this chapter we explored a one-step solvothermal method to synthesize and tune the size and shape of TiO₂ NPs that allowed to obtain highly crystalline sphere and rod-shaped NPs with aspect ratios ranging from ~1 to ~3 with identical structure and cross-sectional area. This strategy aimed to better understand the shape effect of NPs on their behavior in aqueous solutions simulating biological fluids when inorganic constituents play a major role.

The obtained data showed an unexpected dispersive effect of the TiO₂ NPs (opposite to the general trend reported in the literature) in phosphate buffer (pH ~7.4) when increasing the ionic strength (modulated by the addition of NaCl at constant phosphate concentration). Chemical speciation calculations revealed the existence of a synergetic effect between phosphate and Na⁺ ions through the formation of NaHPO₄⁻ species, which greatly influence the aggregation state of NPs that is dependent on their shape (sphere vs. rod).

The complexity of the mechanisms of aggregation-sedimentation of TiO₂ NPs in aqueous solutions with biological interest is inherent to the multiplicity of parameters influencing this process. Although other parameters, such as the temperature and the presence of proteins are also relevant, our results provide practical information for the optimization of conditions in *in vitro* tests using TiO₂ NPs. For instance, the sedimentation data shows the relevancy/limitation of short-term exposures in ecotoxicological studies in the presence/absence of polyatomic anions that need to also include sediment dwellers, which is factually accepted but so far mostly neglected, these results provide practical information to optimize and understand the interaction protein- TiO₂ NPs in the next chapters.

VIII. References

1. X. Chen, S.S. Mao, Titanium Dioxide Nanomaterials: Synthesis, Properties, Modifications, and Applications, *Chemical Reviews*, 107 (2007) 2891-2959.
2. M. Xu, Y. Gao, E.M. Moreno, M. Kunst, M. Muhler, Y. Wang, H. Idriss, C. Wöll, Photocatalytic Activity of Bulk Anatase and Rutile Single Crystals Using Infrared Absorption Spectroscopy, *Physical Review Letters*, 106 (2011) 138302.
3. L. De Marco, M. Manca, R. Giannuzzi, F. Malara, G. Melcarne, G. Ciccarella, I. Zama, R. Cingolani, G. Gigli, Novel Preparation Method of TiO₂-Nanorod-Based Photoelectrodes for Dye-Sensitized Solar Cells with Improved Light-Harvesting Efficiency, *The Journal of Physical Chemistry C*, 114 (2010) 4228-4236.
4. A.R. Petosa, D.P. Jaisi, I.R. Quevedo, M. Elimelech, N. Tufenkji, Aggregation and Deposition of Engineered Nanomaterials in Aquatic Environments: Role of Physicochemical Interactions, *Environmental Science & Technology*, 44 (2010) 6532-6549.
5. A. Philippe, G.E. Schaumann, Interactions of Dissolved Organic Matter with Natural and Engineered Inorganic Colloids: A Review, *Environmental Science & Technology*, 48 (2014) 8946-8962.
6. H. Shi, R. Magaye, V. Castranova, J. Zhao, Titanium dioxide NPs: a review of current toxicological data, *Particle and Fibre Toxicology*, 10 (2013).
7. K. Ninomiya, C. Ogino, S. Oshima, S. Sonoke, S.-i. Kuroda, N. Shimizu, Targeted sonodynamic therapy using protein-modified TiO₂ NPs, *Ultrasonics - Sonochemistry*, 19 (2012) 607-614.
8. A. Sette, J. Spadavecchia, J. Landoulsi, S. Casale, B. Haye, O. Crociani, A. Arcangeli, Development of novel anti-Kv 11.1 antibody-conjugated PEG–TiO₂ NPs for targeting pancreatic ductal adenocarcinoma cells, *J Nanopart Res*, 15 (2013) 1-11.
9. J. Spadavecchia, S. Boujday, J. Landoulsi, C.M. Pradier, nPEG-TiO₂ NPs: A Facile Route to Elaborate Nanostructured Surfaces for Biological Applications, *ACS Applied Materials & Interfaces*, 3 (2011) 2637-2642.
10. M. Jafarpour, M. Ghahramaninezhad, A. Rezaeifard, Synthesis, characterization and catalytic activity of oleic acid-coated TiO₂ NPs carrying MoO₂ (acac)₂ in the oxidation of olefins and sulfides using economical peroxides, *New Journal of Chemistry*, 38 (2014) 2917-2926.
11. Matthieu Fisichella, Frederic Berenguer, Gerard Steinmetz, Melanie Auffan, Jerome Rose, O. Prat, Intestinal toxicity evaluation of TiO₂ degraded surface-treated NPs: a combined physico-chemical and toxicogenomics approach in caco-2 cells, *Particle and Fibre Toxicology*, 9 (2012).

12. T. Ashikaga, M. Wada, H. Kobayashi, M. Mori, Y. Katsumura, H. Fukui, S. Kato, M. Yamaguchi, T. Takamatsu, Effect of the photocatalytic activity of TiO₂ on plasmid DNA1, Mutation Research/Genetic Toxicology and Environmental Mutagenesis, 466 (2000) 1-7.
13. S. Yamaguchi, H. Kobayashi, T. Narita, K. Kanehira, S. Sonezaki, N. Kudo, Y. Kubota, S. Terasaka, K. Houkin, Sonodynamic therapy using water-dispersed TiO₂-polyethylene glycol compound on glioma cells: Comparison of cytotoxic mechanism with photodynamic therapy, Ultrasonics Sonochemistry, 18 (2011) 1197-1204.
14. R.A. French, A.R. Jacobson, B. Kim, S.L. Isley, R.L. Penn, P.C. Baveye, Influence of Ionic Strength, pH, and Cation Valence on Aggregation Kinetics of Titanium Dioxide NPs, Environmental Science & Technology, 43 (2009) 1354-1359.
15. J. Jiang, G. Oberdörster, P. Biswas, Characterization of size, surface charge, and agglomeration state of nanoparticle dispersions for toxicological studies, J Nanopart Res, 11 (2009) 77-89.
16. K.A. Dunphy Guzman, M.P. Finnegan, J.F. Banfield, Influence of Surface Potential on Aggregation and Transport of Titania NPs, Environmental Science & Technology, 40 (2006) 7688-7693.
17. D. Lin, S. Ma, K. Zhou, F. Wu, K. Yang, The effect of water chemistry on homoaggregations of various NPs: Specific role of Cl⁻ ions, Journal of Colloid and Interface Science, 450 (2015) 272-278.
18. X. Liu, G. Chen, C. Su, Effects of material properties on sedimentation and aggregation of titanium dioxide NPs of anatase and rutile in the aqueous phase, Journal of Colloid and Interface Science, 363 (2011) 84-91.
19. H.G. Yang, G. Liu, S.Z. Qiao, C.H. Sun, Y.G. Jin, S.C. Smith, J. Zou, H.M. Cheng, G.Q. Lu, Solvothermal Synthesis and Photoreactivity of Anatase TiO₂ Nanosheets with Dominant {001} Facets, Journal of the American Chemical Society, 131 (2009) 4078-4083.
20. X. Wang, Q. Peng, Y. Li, Interface-Mediated Growth of Monodispersed Nanostructures, Accounts of Chemical Research, 40 (2007) 635-643.
21. P.D. Cozzoli, A. Kornowski, H. Weller, Low-Temperature Synthesis of Soluble and Processable Organic-Capped Anatase TiO₂ Nanorods, Journal of the American Chemical Society, 125 (2003) 14539-14548.
22. Claudia Carlucci, Barbara Federica Scremin, Teresa Sibillano, Cinzia Giannini, Emanuela Filippo, Patrizia Perulli, Agostina Lina Capodilupo, Giuseppina Anna Corrente, G. Ciccarella,

- Microwave-Assisted Synthesis of Boron-Modified TiO₂ Nanocrystals, *Inorganics* 2(2014) 264-277.
23. S. Mugundan, B. Rajamannan, G. Viruthagiri, N. Shanmugam, R. Gobi, P. Praveen, Synthesis and characterization of undoped and cobalt-doped TiO₂ NPs via sol–gel technique, *Appl Nanosci*, 5 (2015) 449-456.
 24. R. Parra, M.S. Góes, M.S. Castro, E. Longo, P.R. Bueno, J.A. Varela, Reaction Pathway to the Synthesis of Anatase via the Chemical Modification of Titanium Isopropoxide with Acetic Acid, *Chemistry of Materials*, 20 (2008) 143-150.
 25. P. Wen, H. Itoh, W. Tang, Q. Feng, Single Nanocrystals of Anatase-Type TiO₂ Prepared from Layered Titanate Nanosheets: Formation Mechanism and Characterization of Surface Properties, *Langmuir*, 23 (2007) 11782-11790.
 26. B. Wu, C. Guo, N. Zheng, Z. Xie, G.D. Stucky, Nonaqueous Production of Nanostructured Anatase with High-Energy Facets, *Journal of the American Chemical Society*, 130 (2008) 17563-17567.
 27. C.-T. Dinh, T.-D. Nguyen, F. Kleitz, T.-O. Do, Shape-Controlled Synthesis of Highly Crystalline Titania Nanocrystals, *ACS Nano*, 3 (2009) 3737-3743.
 28. M. Niederberger, N. Pinna, J. Polleux, M. Antonietti, A General Soft-Chemistry Route to Perovskites and Related Materials: Synthesis of BaTiO₃, BaZrO₃, and LiNbO₃ NPs, *Angewandte Chemie International Edition*, 43 (2004) 2270-2273.
 29. M. Niederberger, G. Garnweitner, N. Pinna, M. Antonietti, Nonaqueous and Halide-Free Route to Crystalline BaTiO₃, SrTiO₃, and (Ba,Sr)TiO₃ NPs via a Mechanism Involving C–C Bond Formation, *Journal of the American Chemical Society*, 126 (2004) 9120-9126.
 30. G. Ciccarella, R. Cingolani, L. De Marco, G. Gigli, G. Melcarne, F. Martina, F. Matteucci, J. Spadavecchia, Process for the preparation of titanium dioxide with nanometric dimensions and controlled shape, *World Patent* 2009/101640, 2010.
 31. Y.-H. Tseng, H.-Y. Lin, C.-S. Kuo, Y.-Y. Li, C.-P. Huang, Thermostability of Nano-TiO₂ and its photocatalytic activity *React Kinet Catal Lett*, 89 (2006) 63-69.
 32. V.H. Grassian, A. Adamcakova-Dodd, J.M. Pettibone, P.I. O'shaughnessy, P.S. Thorne, Inflammatory response of mice to manufactured titanium dioxide NPs: Comparison of size effects through different exposure routes, *Nanotoxicology*, 1 (2007) 211-226.
 33. D. Zhou, A.A. Keller, Role of morphology in the aggregation kinetics of ZnO NPs, *Water Research*, 44 (2010) 2948-2956.

34. Derjaguin BV, L. LD, Theory of the stability of strongly charged lyophobic sols and of the adhesion of strongly charged particles in solutions of electrolytes., *Acta Physicochim URSS*, 14 (1941) 733-762.
35. Verwey EJW, O. JTG, Theory of the stability of lyophobic colloids., Elsevier, Amsterdam, 1948.
36. R.F. Domingos, N. Tufenkji, K.J. Wilkinson, Aggregation of Titanium Dioxide NPs: Role of a Fulvic Acid, *Environmental Science & Technology*, 43 (2009) 1282-1286.
37. D.S. Brown, J.D. Allison., MINTEQA1. An equilibrium metal speciation model. User's manual EPA/600/3-87/012. , US Environmental Protection Agency, Athens, GA. , 1987.
38. W. Zhang, Y. Li, Y. Su, K. Mao, Q. Wang, Effect of water composition on TiO₂ photocatalytic removal of endocrine disrupting compounds (EDCs) and estrogenic activity from secondary effluent, *Journal of Hazardous Materials*, 215–216 (2012) 252-258.
39. M. Erhayem, M. Sohn, Stability studies for titanium dioxide NPs upon adsorption of Suwannee River humic and fulvic acids and natural organic matter, *Science of The Total Environment*, 468–469 (2014) 249-257.
40. Rute F. Domingos, Caroline Peyrot, K.J. Wilkinson, Aggregation of titanium dioxide NPs: role of calcium and phosphate, *Environ. Chem.* ,, 7 (2010) 61.
41. M. Chen, N. Xu, X. Cao, K. Zhou, Z. Chen, Y. Wang, C. Liu, Facilitated transport of anatase titanium dioxides NPs in the presence of phosphate in saturated sands, *Journal of Colloid and Interface Science*, 451 (2015) 134-143.
42. P.A. Connor, A.J. McQuillan, Phosphate Adsorption onto TiO₂ from Aqueous Solutions: An in Situ Internal Reflection Infrared Spectroscopic Study, *Langmuir*, 15 (1999) 2916-2921.

Appendix I

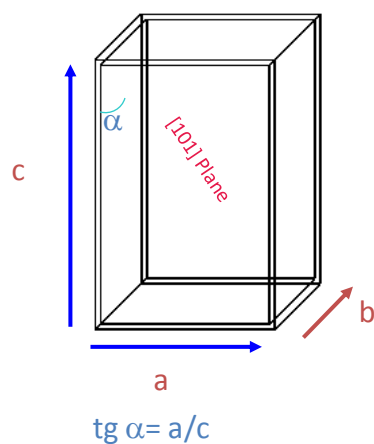


Figure S1. Schematic representation of the crystalline structure showing the [101] plane.

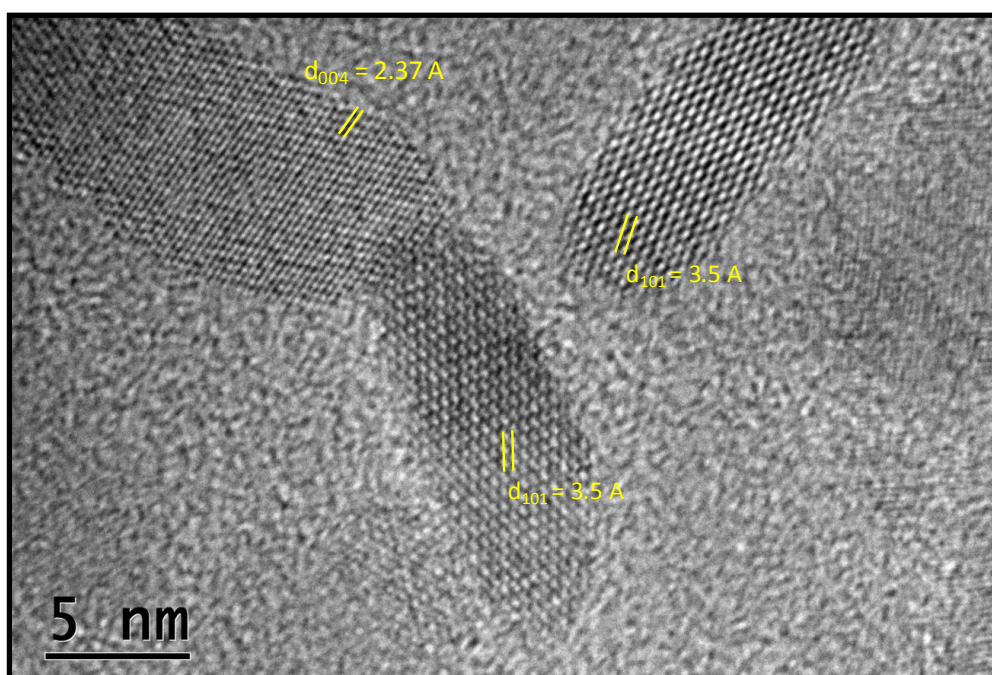


Figure S2. Additional HRTEM microphy of TD12 sample. The orientation of crystallographic plans [101] and [004], identified by Inter reticular distances measurement form FFT and line profile, is consistent with a growth along the c-axis.

Appendix II

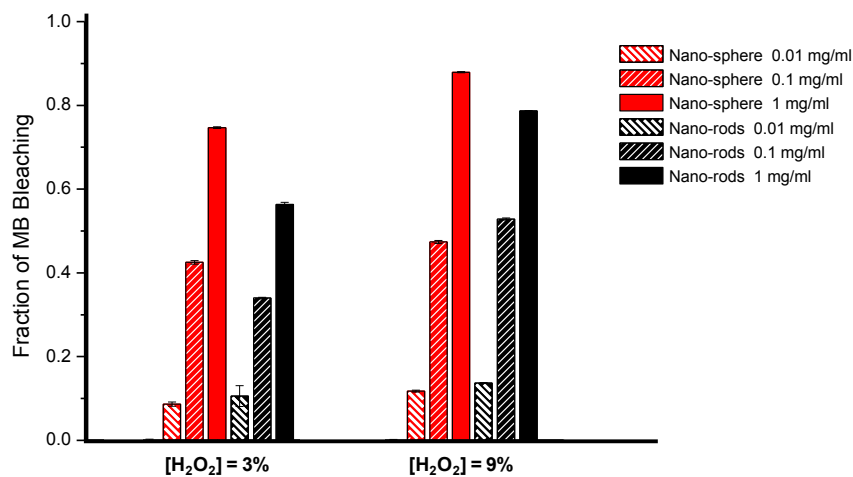


Figure S3. Evolution of the fraction of methylene blue (MB) bleaching for nano-spheres or nano-rods of TiO₂ dispersed in ultrapure water in presence of different concentrations of H₂O₂ (as indicated). Values are calculated from 3 measurements

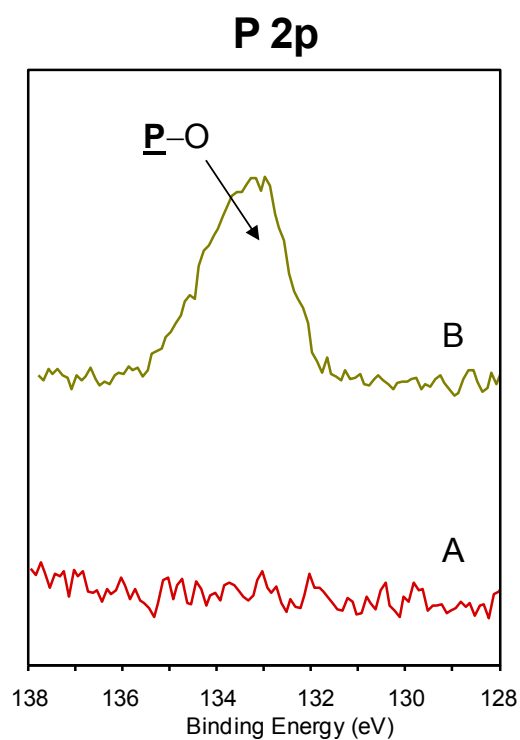


Figure S4. XPS peaks of phosphor (P 2p) recorded on TiO₂ NPs (A) prior to and (B) after dispersion in phosphate buffer (100 mM) for 24h and subsequent rinsi

**Chapter 4: Evidences of supramolecular
structural changes of type I collagen upon
interaction with sphere and rod-shaped TiO₂ NPs**

Table of contents

Chapter 4: Evidences of supramolecular structural changes of type I collagen upon interaction with sphere and rod-shaped TiO₂ NPs	113
I. Introduction	115
II. Organization of the collagen layer in the dried state	117
III. Organization of the collagen layer in the hydrated state	121
IV. Mechanism of collagen-TiO₂ NPs interaction	125
V. Conclusion	133
VI. Bibliography	134

I. Introduction

As described previously on the bibliographic part the collagen is the most abundant fibrillary protein of the extracellular matrix¹. This protein constitutes the connective tissue like skin, bone, tendon, cartilage and ligament². There are various types of collagen amongst which the most common is collagen type I. Monomer collagen I presents helical structure made of three chains twisted between them with a molar size of 300kg/mol and 300nm length for 1,5nm diameter³, the triple-helix binding domains consist of linear sequences along the helix. Each monomer is constructed by repetition of the same amino acid sequence Glycine-X-Y where X and Y can be any amino acid (generally X: proline, Y: hydroxyproline⁴). The type I collagen is a right-handed helix composed of three polypeptide chains with non-helical ends (telopeptides). Monomers are able to associate between them to form fibers by cross-linking via the amino acids lysine and hydroxyl lysine present in the telopeptide regions, this leads to the formation of periodic structures along the fibril length with a periodicity of 67nm.

In vivo, collagen molecules have an outstanding ability to self-assemble and to interact with other entities to form elegant nanostructured architectures as in ECM or in hard biomineralized tissues^{5,6}.

In vitro, nanostructured collagen layers may be obtained by adjusting the adsorption procedure, the characteristic of the medium (pH, T °C, composition and ionic strength), collagen conformation (native or denatured), etc^{7,8}. However, *in vitro*, the tridimensional structure of collagen may be altered, at a different extent, when the protein is subject to heating, irradiation, etc. Collagen denaturation by heating involves the rupture of hydrogen bonds and the rearrangement of the triple helix into random coils. This process is generally initiated in a so-called thermally labile domain where the concentration of hydroxyproline is low⁹.

In contrast to some proteins (called “soft protein”), collagen is not expected to undergo conformation changes upon adsorption on solid surfaces, the driving force being an entropy gain due to the liberation of water molecules. However, the situation may be different if the interaction is performed with nanostructured materials rather than flat substrates. In particular, the interaction of proteins with NPs (NPs) involves multiple processes which are not observed on flat substrate (made with the same material), such as conformation changes depending on the particle size¹⁰ and formation of protein corona¹¹.

The behavior of collagen in aqueous media in the presence of TiO₂ NPs has attracted a little interest, compared to other proteins. Yet, the effect of these NPs on the collagen properties is with primary importance, owing to the extensive use of TiO₂ in cosmetics and other derived products, in food industry, packaging, etc.

The aim of this study is to probe the interaction of type I collagen with sphere or rod-shaped TiO₂ NPs in buffer solution and to evaluate its impact on the ability of the protein to self-assemble and self-organize in the adsorbed phase. This strategy offers many advantages. First, it explores the high sensitivity of supramolecular organization of collagen on solid surfaces to the regard of the intrinsic properties of the protein and its environment. Second, it consists in using surface science techniques, in particular atomic force microscopy (AFM) which is recognized to be a powerful tool to unravel the organization of macromolecules at interfaces¹². Third, it benefits of the significant understanding achieved during the last decade regarding the mechanism of adsorption and organization of collagen on solid surfaces. A particular attention is dedicated to the mechanism by which TiO₂ NPs may interact with collagen in the aqueous medium as a function of their shape (sphere vs rod). The adsorption of collagen was performed on either silicon wafer or on PS substrate from (i) solution of collagen (called “Col”), (ii) a suspension containing a mixture of collagen and sphere-shaped TiO₂ NPs (called “Col-Nano_S”), or (iii) a suspension containing a mixture of collagen and rod-shaped TiO₂ NPs (called “Col-Nano_R”). Sphere and rod-shaped TiO₂ NPs with highly controlled size and morphology were obtained and used in adsorption tests (Figure 1). The obtained collagen layers were characterized both in the dried state, by mean of AFM imaging and XPS, and in the hydrated state using AFM force spectroscopy.

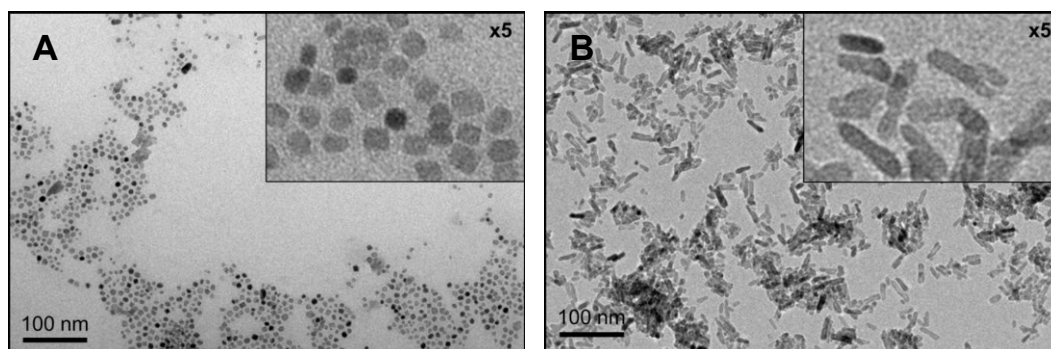


Figure 4.1: TEM micrographs of TiO₂ NPs: (A) nano-spheres (Nano_S) and (B) nano-rods (Nano_R).

II. Organization of the collagen layer in the dried state

Col, Col-Nano_S and Col-Nano_R solutions were pre-incubated either at RT or at 37 °C during 20 min. AFM images of the collagen layers obtained after adsorption on PS substrate and drying are presented in Figure 2. The adsorbed layers appear to be discontinuous in all cases. In Col solution, the obtained layers resemble to a network, independently of the temperature of pre-incubation. In the presence of NPs in the pre-incubation solution, the adsorbed layers show two hierarchical level of organization (Figure 2B and C). The larger ones appear as dendrite-like structures (Figure 2 B, Col-Nano_S) or dot-like structures (Figure 2C, Col-Nano_R), while the smaller ones appear as a dense net. Cross-sections reveal that the height of the latter nanostructures is ranging from 1.7 to 6.4 nm (Figure 2 D), while the former show a height of about 10.6 nm. When the pre-incubation was performed at 37 °C in the sphere-shaped NPs, the two level of organization remain visible in the presence of nano-spheres (Figure 2 F). However, the morphology of the adsorbed layer obtained in the presence of nano-rods is radically different showing only one level of large structures with an average height of 10.6 nm (Figure G and H), i.e. identical to the large segments observed at RT (Figure 2 C).

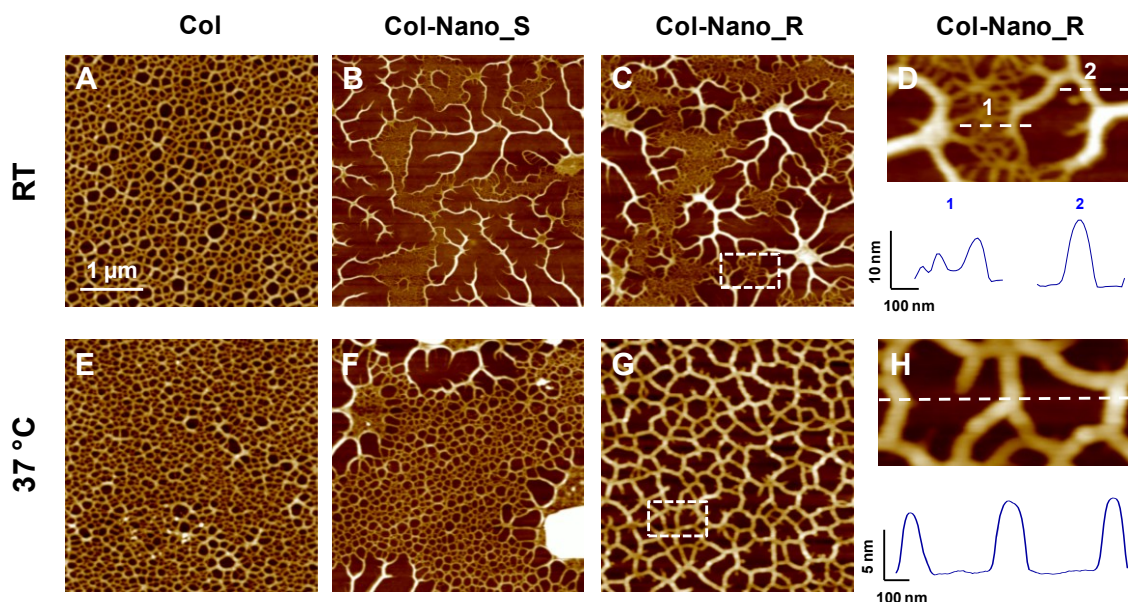


Figure 4.2: Representative AFM height images ($4 \times 4 \mu\text{m}^2$, Peak Force Tapping mode, in air, z-scale 20 nm) recorded on PS substrate after incubation at RT in A, at 37°C in E collagen solution (Col) or a mixture of collagen and either TiO₂ (B, F) nano-spheres (Col-Nano_S) or (C, G) nano-rods (Col-Nano_R) and subsequent drying. Images (D) and (H) are zooms recorded at the area demarcated by a rectangle in images (C) and (G), respectively. Pre-incubation of collagen and TiO₂ NPs was performed during 20 min at (A, B, C, D) RT or (E, F, G, H) 37 °C. Cross sections were taken at the locations indicated by dashed lines and numbered.

The pre-incubation of Col, Col-Nano_S and Col-Nano_R solutions was also performed during 24h instead of 20 min. Results given in Figure S1 (appendix), reveal a smooth and continuous layer when the adsorption was performed in Col solution at RT (Figure S1 A, appendix). The presence of nano-spheres in the solution (Col-Nano_S) leads to the appearance of a dense layer of filamentous structures which present an average height of 1.6 nm and may thus correspond to collagen monomers (Figure S1B, appendix). In both cases (Col and Col-Nano_S), the surface roughness is significantly lower to that observed at 20 min pre-incubation (Table 1). The presence of nano-rods instead of nano-spheres radically changes the morphology of the adsorbed layer showing the formation of large dendritic structures (Figure S1 C, appendix). This leads to an appreciable decrease of the surface roughness (Table 1). At 37°C, a discontinuous layer is obtained with Col solution with frequent presence of holes (Figure S1D, appendix). The discontinuity of the layer becomes more and more pronounced in the presence of sphere and rod-shaped TiO₂ NPs (Figure S1E and F, appendix). Cross-sections reveal that the average depth of holes present on the collagen layer increases markedly: 6.0, 7.5, and 10.3 nm for Col, Col-Nano_S and Col-Nano_R solutions, respectively.

High resolution AFM images provide more details regarding the morphology of the adsorbed layers obtained after incubating PS substrate in a mixture of collagen and TiO₂ NPs and subsequent drying (Figure 3). The images show a variety of patterns made with collagen nanostructures with different size, shape and distribution along the surface. Some nanostructures have a dimension close to that of a collagen fibril which is obtained by the adjacent association of five triple helical molecules. However, the presence of collagen fibers is not observed in any case, as verified in AFM deflection images (Figure 3E-H). The latter hierarchical structure consists in a bundle of collagen molecules showing a periodic band pattern (D-periodicity ~67 nm) and may be revealed by AFM deflection images⁷.

In addition, based on high resolution AFM images, it appears that the nanostructured and discontinuous patterns are formed on the PS substrate and no underlined collagen layer can be visible (see deflection images, Figure 3). This information is with primary importance as it may help to decipher the mechanism of self-assembly and self-organization of collagen upon adsorption on PS substrate and subsequent drying (for more details see discussion in section II.C)

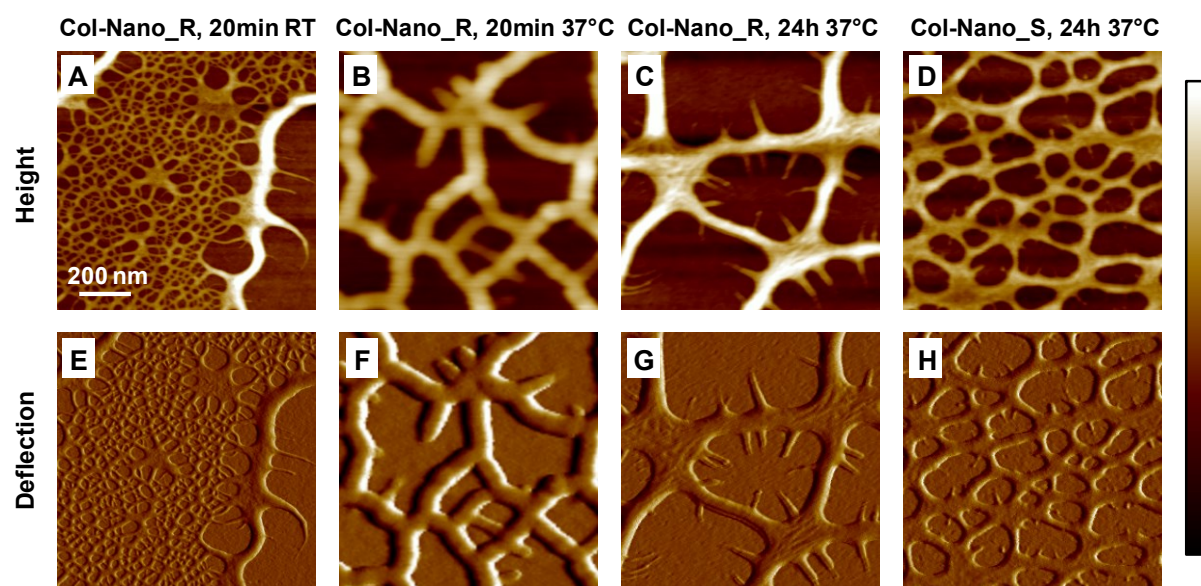


Figure 4.3: High resolution AFM (A-D) height and the corresponding (E-H) deflection images ($1 \times 1 \mu\text{m}^2$, Peak Force Tapping mode, in air, z-scale 20 nm) recorded on PS substrate after incubation at RT in a mixture of collagen and TiO₂ (A-C; E-G) nano-rods (Col-Nano_R) or (D, H) nano-spheres (Col-Nano_S). Pre-incubation of collagen and TiO₂ NPs was performed during 20 min or 24h at RT or 37 °C, as indicated.

AFM images obtained after collagen adsorption on silicon wafer (pre-incubation time of 20 min) and drying are shown in Figure 4. The morphology of collagen layers is completely different compared to that on PS. The dimensions of the observed nanostructures appear appreciably lower compared to those formed on PS substrate. Accordingly, AFM images of $1 \times 1 \mu\text{m}^2$ are shown to gain a more detailed view of morphological changes of the adsorbed layers. The adsorbed layer of collagen (Col solution) exhibits small filamentous structures with almost uniform heights (Figure 4 A). At 37°C larger nanostructures are observed, suggesting that the increase of temperature is favorable to the formation of fibrillar structures. Moreover, this trend seems to be more pronounced in the presence of rod-shaped NPs (Figure 4 F).

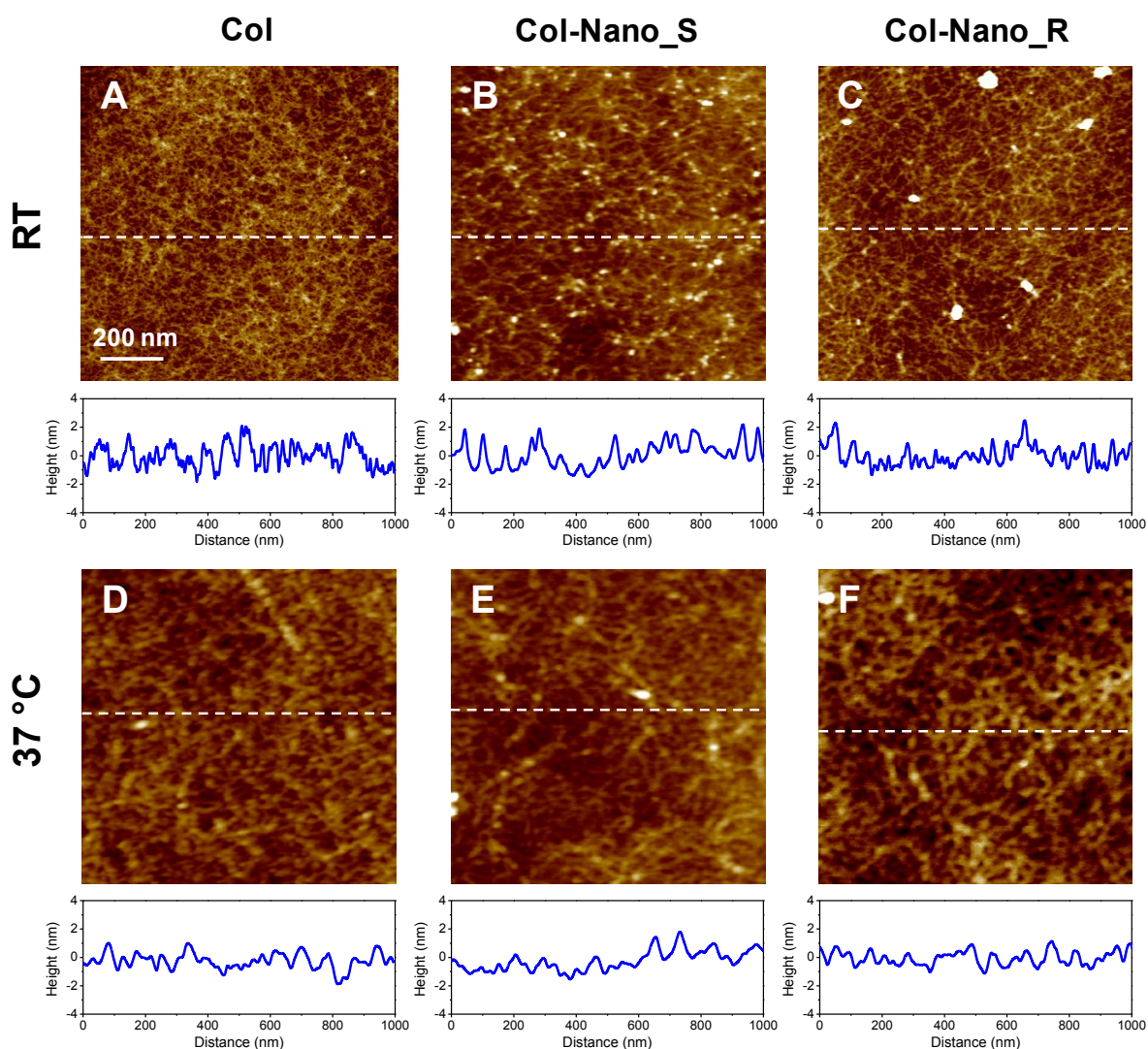


Figure 4.4: Representative AFM height images ($1 \times 1 \mu\text{m}^2$, Peak Force Tapping mode, in air, z-scale 8 nm) recorded on silicon substrate after incubation at RT (A) at 37 °C (D) in, collagen solution (Col) or a mixture of collagen and either TiO₂ (B, E) nano-spheres (Col-Nano_S) or (C, F) nano-rods (Col-Nano_R) and subsequent drying. Pre-incubation of collagen and TiO₂ NPs was performed during 20 min at (A, B, C) RT or (D, E, F) 37 °C. Cross sections were taken at the locations indicated by dashed lines.

After a pre-incubation time of 24 h at RT, the evolution of the layer morphology is obvious in the presence of TiO₂ NPs. Indeed, the addition of nano-spheres or nano-rods leads to the formation of evident filamentous structures. By contrast, the adsorbed layer appears almost unchanged at 37 °C (Figure S2, appendix). It exhibits a discontinuous film with a recurrent occurrence of holes and occasional presence of fibrillar nanostructures. Moreover, the film seems to be unstable under drying or under the action of the AFM tip (Figures S2 D-F). In all cases, the roughness of the collagen layer adsorbed on silicon wafer does not change significantly and remains relatively low (in the range of

0.6 to 0.8 nm, Table 1). This may be explained by the low thickness of the adsorbed layer and the small size of collagen nanostructures.

R_{rms} (nm)	20min / RT	20min / 37 °C	24h / RT	24h / 37 °C
Silicon				
Col	0.7±0.05	0.8±0.04	0.8±0.03	0.9±0.06
Col-Nano_S	0.9±0.05	0.6±0.04	0.7±0.04	0.7±0.02
Col-Nano_R	0.7±0.3	0.8±0.06	0.7±0.05	0.8±0.03
PS				
Col	3.8±0.3	3.4±0.1	0.9±0.03	2.5±0.3
Col-Nano_S	2.6±0.1	3.0±0.2	1.2±0.07	3.3±0.2
Col-Nano_R	3.3±0.4	4.0±0.2	3.9±0.02	4.4±0.1

Table 4.1: Root-mean-square roughness (R_{rms}) measured on AFM images ($4 \times 4 \mu\text{m}^2$) recorded in air. Standard deviations correspond to three independent values taken at different location of the sample.

III. Organization of the collagen layer in the hydrated state

Another approach to probe the supramolecular organization of collagen in the adsorbed phase is to explore its ability to interact with AFM tip in the liquid phase. This approach may bring complementary information to the one described above in which collagen adsorbed layers were submitted to drying. It is worth reminding that the main reasons that AFM imaging in liquid was not explored here is due the peculiar configuration that adsorbed collagen molecules may adopt. Indeed, on hydrophobic substrate, collagen segments protrude in the solution and form a highly hydrated and viscoelastic layer¹³. As a consequence, imaging collagen layers in this condition would be extremely dependent on the ability of the proteins to interact with and to be moved by the AFM tip during scanning. The strategy followed in the present study consists in approaching the AFM tip, maintaining it in contact with the surface at a certain time (surface delay) to insure to collagen molecules to interact with the tip, then retracting the tip up to break the collagen-tip link. The force-distance curves recorded during these events provide three relevant parameters. The first parameter is the probability of adhesion which corresponds to the number of occurrence of collagen-tip interaction; the second is the force corresponding to the rupture of collagen-tip link, and the third one is the rupture length.

The organization of adsorbed collagen adopted on the hydrophobic PS substrate or in the hydrophilic silicon wafer would thus influence subsequent interaction with the AFM tip during force-distance

recording as depicted in Figure 5A. Examples of force-distance curves are presented in Figure 5B showing single or multiple pull-off events at different distance from the surface. On bare PS substrate the force curve do not show any adhesion events (Figure 5 B), while on silicon wafer a high adhesion force of 2.5 nN was observed (data not shown). In the presence of adsorbed collagen the mean adhesion forces are ranging from about 130 to about 220 pN (Figure 5 C and S5-7, appendix) were observed on PS and silicon substrates, suggesting that the adhesion events are due to collagen-tip interaction.

The influence of the surface delay on the probability of adhesion events was investigated on collagen layer adsorbed on silicon wafer. Results give in Figure S3 (appendix) show that this parameter has a little effect on the occurrence of adhesion events, indicating that the interaction between adsorbed collagen and the AFM tip is rapid, as expected. Increasing the surface delayer in the range of few seconds may lead to significant drifts of the scanner. A surface delay of 500 ms was thus used in all the experiments

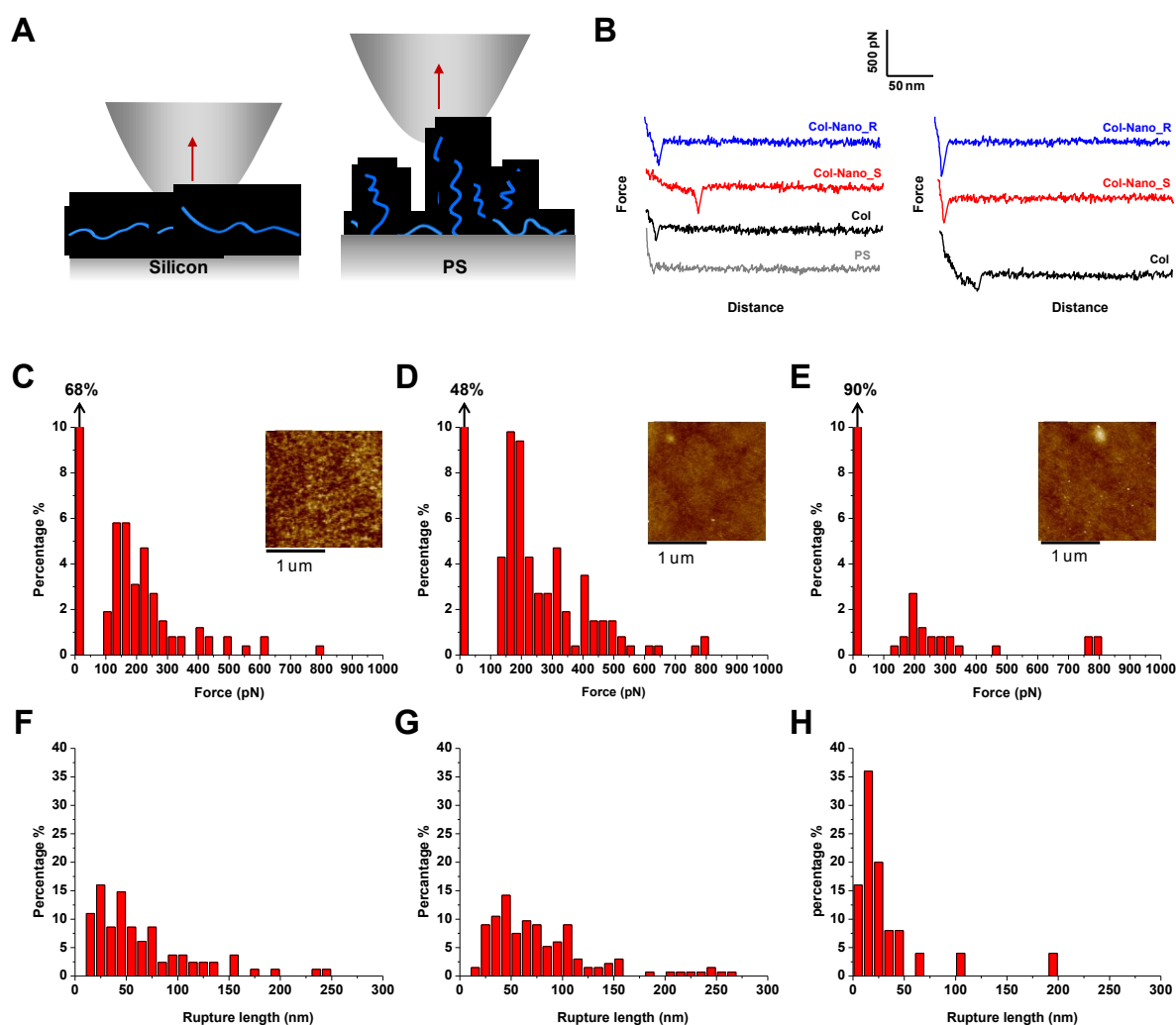


Figure 4.5: AFM force spectroscopy. (A) AFM tip-collagen interaction on PS substrate or silicon wafer. (B) Representative force-distance curves recorded in PBS buffer between the AFM tip and adsorbed collagen. (C-E) Adhesion force histograms and (F-H) rupture length histograms obtained by recording force-distance curve on PS substrate after incubation at RT in (C, F) collagen solution (Col) or a mixture of collagen and either TiO₂ (D, G) nano-spheres (Col-Nano_S) or (E, H) nano-rods (Col-Nano_R) and subsequent rinsing with PBS. Pre-incubation of collagen and TiO₂ NPs was performed during 24h at RT. The data shown correspond to 768 force-distance curves obtained from three independent experiments. Inset: Representative AFM height images recorded in PBS.

Significant variations are observed in the probability of adhesion occurrence as a function of the pre-incubated solution (Col; Col-Nano_S and Col-Nano_R). The tendency is more pronounced on PS substrate. Indeed, the percentage of non-adhesive events increases markedly in the presence of nano-rods from 68 and 48% in Col and Col-Nano_S solutions, respectively, to 90% in Col-Nano_R (Figure 5 C-E). The same trend is also observed when the pre-incubation was performed during 20 min (Figure S4, appendix). By contrast, on silicon wafer, the occurrence of non-adhesive events remains almost unchanged at a pre-incubation time of 20 min (Figure S6 A-C, appendix) and decreases markedly in Col-Nano_R solution after 24h of pre-incubation (Figure S7 A-C, appendix).

These variations may be associated with the organization adopted by adsorbed collagen molecules and, therefore, their accessibility and ability to interact with the AFM tip.

The meaning and the relevancy of these adhesion events appear more clearly if the surface area probed by the AFM tip is evaluated. A rough estimation of the contact area may be determined via the JKR model which is reasonably adapted to the experimental parameters used in this study¹⁴. According to this model, the radius of the contact area, a , may be computed as follows:

$$a = \left[\frac{3R}{4K} \left(F + 3\pi R W_{ad} + \sqrt{6\pi R W_{ad} F + (3\pi R W_{ad})^2} \right) \right]^{\frac{1}{3}}$$

where R is the tip radius, K the elasticity modulus of the adsorbed layer, F the loading force and W_{ad} the work of adhesion which may be deduced from measured adhesion force (F_{ad}) according to the following relation:

$$W_{ad} = -\frac{2}{3\pi R} F_{ad}$$

By taking an elastic K ranging from 0.2 to 5 GPa^{15, 16}, a tip radius of 30 nm and a loading force $F = 400$ pN, a contact radius ranging from 1.5 to 4.5 nm is obtained. Accordingly, a contact area between the AFM tip and the adsorbed collagen layer is in the range of about 7 to 60 nm². Therefore, it is very likely that the adhesion observed in the force-distance curves do not correspond to single pull-off events, owing to the presence of collagen nanostructures at different scales. Furthermore, the entanglement of adsorbed collagen nanostructures and the protrusion of molecular segments favor the involvement of multi-interaction with the AFM tip. This behavior is indeed observed in many force curves showing multiple force peaks (Figure 6).

The adhesion force histograms (Figures 4 and S4-S6, appendix) show that the mean adhesion force varies in the range of 130 to 220 pN, depending on the pre-incubation conditions and whether the adsorption was performed on PS or silicon substrate. This force corresponds to the pull-off of collagen segments from the AFM tip. The rupture length also appears to be influenced by the pre-incubation conditions and the nature of the substrate. After a pre-incubation at RT on PS substrate, the rupture length is in the same order (around 50 nm) for Col and Col-Nano_S solution but it decreases for Col-Nano_R solution (Figure 5F-H). When the pre-incubation is performed on silicon wafer during 20 min, the rupture length seems to be independent on the presence of NPs (Figure S5 and S6), while after 24h it increases in the presence of sphere or rod-shaped NPs.

The presence of multiple peaks in a substantial proportion of force-distance curves is observed both on PS substrate and silicon wafer (Figure 6). This adhesion feature may include at least two processes

with different nature: (i) the interaction of multiple collagen segments and the AFM tip, leading to the appearance of multiple pull-off events at different distance from the substrate, and (ii) the stretching of collagen molecular segments which is characterized by the presence of a sawtooth pattern. To decipher the overlapping of adhesion features in the force-distance curves the distances between rupture events can be explored, as reported by Gutsman et al.¹⁷ showing the repetition of two periodic rupture events distances around 23 and 77 nm. In the present study, the histograms of distances between successive ruptures are shown in Figure 6, revealing a mean distance around 20 nm. This distance was attributed to weak interaction between collagen molecules of the fibrils¹⁷. It appears that the presence of NPs did not influence this repeating rupture patterns, but the question clearly deserve further investigations.

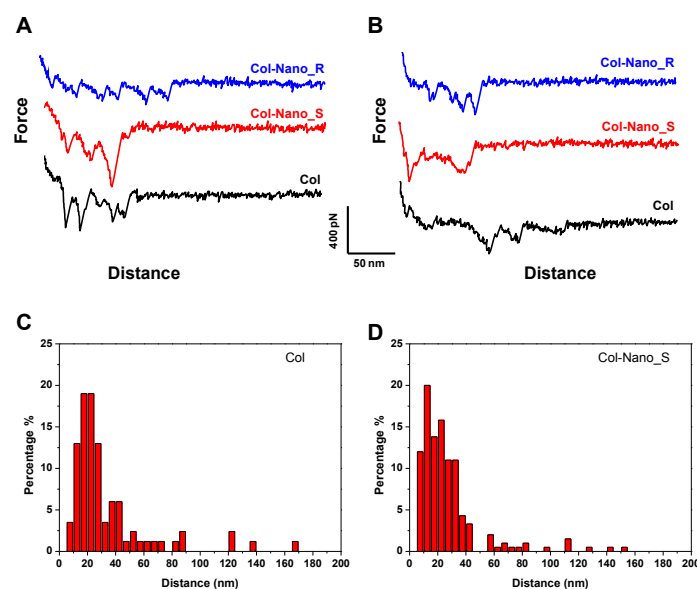


Figure 4.6: (A, B) Representative force-distance curves showing multiple adhesion peaks recorded in PBS on (A) PS or (B) silicon wafer after incubation at RT in collagen solution or a mixture of collagen and either TiO₂ nano-spheres (Col-Nano_S) or nano-rods (Col-Nano_R), as indicated, and subsequent rinsing with PBS. (C, D) Histograms of the distances between rupture events.

IV. Mechanism of collagen-TiO₂ NPs interaction

The above findings, regarding the organization of adsorbed collagen in the dried and the hydrated phase, clearly indicate that the addition of sphere or rod-shaped TiO₂ NPs in the pre-incubated solution of collagen provokes significant morphological changes. This behavior is observed at different conditions (temperature and duration) of the pre-incubation step as well as the nature of the substrate used in the incubation step. It is worth reminding that the nanoscale organization of

adsorbed collagen may results from different processes which have been recently reviewed by Dupont-Gillain¹⁸. Collagen assembly mainly occurs at the interface and does not result in the adsorption of aggregates formed in solution. On a hydrophobic substrate such as PS the assembly of collagen molecules is strongly favored. This may be explained by the configuration adopted by adsorbed collagen which attaches to the surface through molecular segments and leaves “free” the remaining part, the latter being able to be involved in assembly with other adsorbed collagen molecules. By contrast, on hydrophilic surface, such as silicon wafer, the collagen-substrate interaction is stronger leading to the formation of smoother layers in which collagen molecules are in a closer contact the substrate.

The structural changes observed in the present suggest the possibility of different mechanisms by which the presence of NPs influence the collagen organization in the adsorbed phase.

Mechanism (1). A direct action of TiO₂ NPs during the incubation step resulting in the co-adsorption of collagen and NPs (to our knowledge no available data from the literature). This suggests that NPs are present in a significant amount on the substrate and may disturb the adsorption behavior of collagen (adsorption, mobility, self-assembly, etc). In the experimental conditions used in this study, TiO₂ NPs are expected to predominate in the aggregate state (see chapter 3 II. E), but the presence of TiO₂ aggregates is not obvious in AFM images. This requires a fine chemical analysis.

Mechanism (2). An indirect action of TiO₂ NPs during the pre-incubation step via there catalytic properties to produce radicals, which may influence the tridimensional structure of collagen in solution. Indeed, the conformation of collagen is among the main factors influencing its organization in the adsorbed phase⁷.

Mechanism (3). An indirect action of TiO₂ NPs during the pre-incubation step by modifying the properties of collagen solution (probably the viscosity) which may influence (i) the adsorption behavior of collagen at the interface and (ii) the dewetting process, as the adsorbed layers were probed by AFM after drying. Indeed, Jacquemart et al. have obtained different morphologies of collagen layers by varying the amount of adsorbed collagen (modulated by the incubation time) and the velocity of drying¹⁹. The authors suggest that the nanostructured patterns of collagen obtained by adsorption and drying result in the dewetting of a liquid phase on a solid substrate. As drying is performed after rinsing, the liquid phase involved in the dewetting should be the buffer solution (PBS) and the solid substrate is either PS or silicon wafer modified by collagen layers, which is expected to modify the wetting properties of the underlined substrate.

On the basis of AFM data detailed above, it is not easy to clarify the mechanism(s) by which sphere and rod-shaped TiO₂ NPs influence the morphology of collagen layers.

The possible co-adsorption of TiO₂ NPs (*"Mechanism (1)"*) was investigated by means of XPS, owing to the outstanding capacity of these techniques to probe thin (bio)-organic adsorbed layers and its detection sensitivity²⁰. XPS analyses were performed on both PS and silicon substrates after adsorption of collagen from the different solution. Examples of C 1s peaks obtained are given in Figure 7. On PS substrate, the main component at 284.8 eV is due to carbon bound only to carbon and hydrogen C-(C,H), while the component present for PS at about 291.7 eV is due to an energy loss attributed to $\pi \rightarrow \pi^*$ transitions of the aromatic rings (shake-up). After collagen adsorption (from Col_Nano_R solutions) the shake-up component at 291.5 eV is still visible, suggesting that the adsorbed collagen layer does not completely screen the PS substrate. This is in agreement with AFM image showing a discontinuous layer which left uncovered zones of the substrate (Figure 2C and G). At 24h of pre-incubation at RT, the shake-up contribution is no longer visible and two new components were observed, one at ~286.3 eV due to carbon singly bound to oxygen or nitrogen C-(O,N) and one at ~288.0 eV due to carbon of the peptidic link N-C=O. The intensity of these components varies as a function of the pre-incubation conditions and the nature of the substrate (Figure 7). More importantly, the presence of titanium was not detected by XPS, regardless of the amount of adsorbed collagen and the substrate used (PS or silicon wafer) for adsorption. These results reveal that TiO₂ NPs do not co-adsorb in a significant amount (at the detection limit of XPS 0.1eV). However, their presence could not be totally ruled out, as particles may be, for instance, coated with collagen molecules.

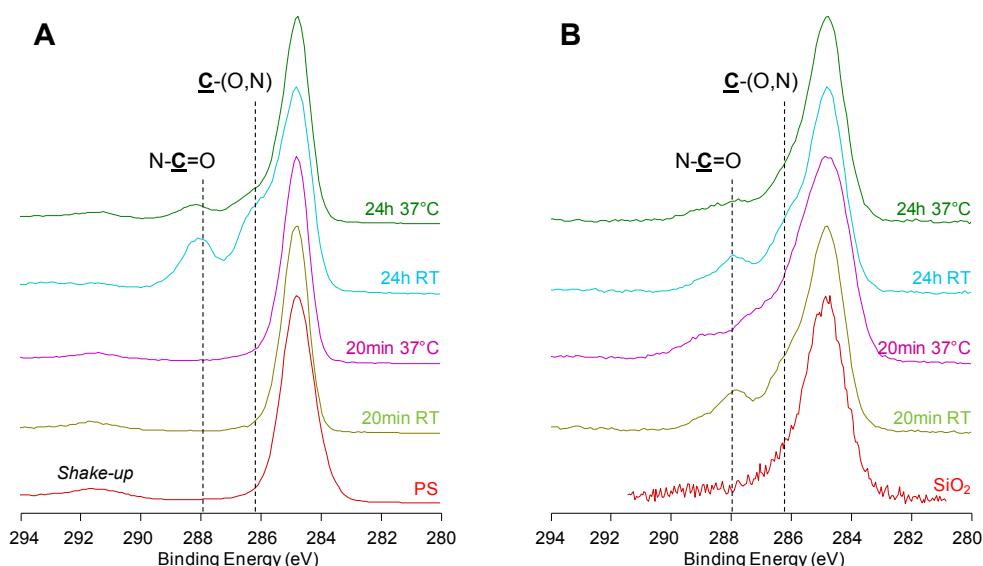


Figure 4.7: Representative C 1s and N 1s peaks recorded by XPS on (A) PS substrates and (B) silicon wafers prior to and after incubation in collagen solution (Col) or a mixture of collagen and TiO₂ nano-rods (Col-Nano_R). Pre-incubation of collagen and TiO₂ NPs was performed either during 20 min or 24h at RT or at 37 °C (as indicated).

The suggested *Mechanism (2)* which is related to the ability of TiO₂ NPs to produce radicals is expected to induce alteration in the tridimensional structure of collagen, i.e. conformational changes, and/or in its ability to self-assemble at the interface. Indeed, TiO₂ NPs are known to exhibit chemical or photo-catalytic properties which depend on their intrinsic properties (size, shape, cristallinity) and the properties of the surrounding medium²¹. In the present study, this mechanism was investigated by amplifying the chemical or the photo-catalytic activity of TiO₂ with the aim to evaluate its impact on the morphology of the adsorbed layer after drying. For this purpose, the pre-incubation step was performed either in the presence of H₂O₂ (3%) during 24h, or under UV irradiation during 20 min. AFM images show that the presence of H₂O₂ leads to the formation of dense collagen layer with the presence of filamentous structures (Figure 8A-D). This morphology was observed whatever H₂O₂ was added in the presence of TiO₂ NPs or not. Even, it appears that the presence of collagen fibrils is more pronounced in the presence of NPs (Figure 8A-D), a detailed analysis of several AFM images did not allow to conclude about a clear trend. This suggests that the presence of fibrillar structures in the adsorbed layers is mainly due to the presence of H₂O₂ itself, rather than the catalytic reaction it may induce in the presence of TiO₂ NPs.

The effect of UV irradiation of the pre-incubated solution was also investigated. AFM images (Figure 8E-H) show an evolution of the layer morphology; especially in the presence of TiO₂ nano-spheres (Figure 8G) which exhibit a net-like structure. This evolution was also observed without NPs (Figure 8F) but it was less pronounced. Furthermore, the filamentous morphology is observed in all cases except in the presence of nano-rods (Figure 8H). It is worth noting, that despite the changes observed in the adsorbed layers in the presence of H₂O₂ or under UV irradiation, the productions of radicals in these conditions was not detected using a protocol of degradation of methylene blue (MB) (see chapter 3. II. B).

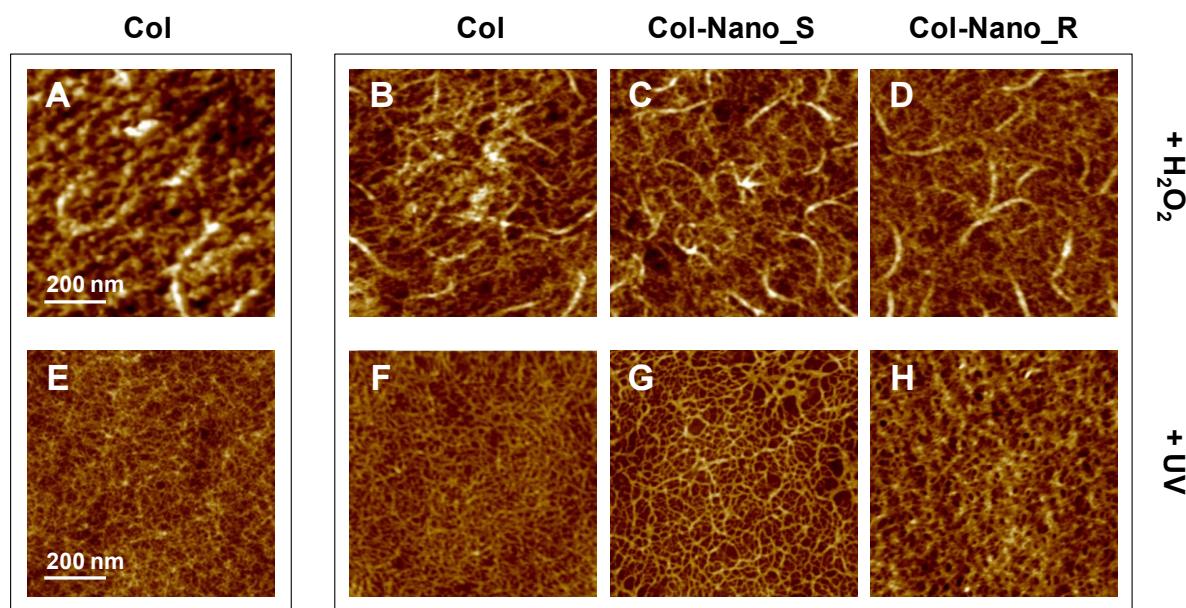


Figure 4.8: Representative AFM height images ($1 \times 1 \mu\text{m}^2$, Peak Force Tapping mode, in air, z-scale 8 nm) recorded on silicon substrate after incubation at RT in (A) collagen solution (Col), or (B-D) in solutions containing H₂O₂ (3%): (B) collagen solution, or a mixture of collagen and either TiO₂ (C) nano-spheres (Col-Nano_S) or (D) nano-rods (Col-Nano_R). The pre-incubation was performed during 24h at RT. (E-F) Images (with the same characteristics) recorded on silicon wafer after incubation at RT in (A) collagen solution (Col), or (B-D) in solutions subjected to UV irradiation of (B) collagen solution, or a mixture of collagen and either TiO₂ (C) nano-spheres (Col-Nano_S) or (D) nano-rods (Col-Nano_R). The pre-incubation was performed during 20 min at RT under UV irradiation.

At this stage, the main question is to know if the presumable catalytic properties of TiO₂ NPs alter the conformation of collagen monomers in solution. A tentative of answer may be provided by ATR-IR analysis performed directly in collagen solutions. Results given in Figure 9 show the presence of the characteristic bands of collagen. The bands at about 1556 and 1653 cm⁻¹ are attributed to amide II and amide I, respectively. The band at 1456 cm⁻¹ may be attributed to $\delta(\text{CH}_2)$ and the one at about 1406 cm⁻¹ to the symmetric stretching of carboxylate residues. When the pre-incubation was performed at RT (Figure 9 A-B), IR-ATR spectra do not show noticeable changes in the characteristic vibrational features of collagen, except that the relative intensity of amide I band may slightly vary to the respect of the amide II band in the presence of TiO₂ nano-rods. These results suggest that the presence of TiO₂ NPs does not induce important conformational changes which may alter the tridimensional structure of collagen. At 37°C of pre-incubation, IR-ATR spectra show the appearance of a band at 1742 cm⁻¹ which may be attributed to $\nu(\text{C=O})$ (Figure 9 C). Interestingly, this band is only observed in the presence of TiO₂ nano-spheres and nano-rods.

For sake of comparison, IR-ATR spectra were also recorded on collagen solution pre-incubated under UV irradiation or in the presence of H₂O₂ following the procedure described above. Results given in

Figure S7 (appendix) reveal that UV irradiation has no noticeable influence on the characteristic bands. By contrasts, the presence of H₂O₂ leads to the appearance of large broadening in the range of 1300 to 1500 cm⁻¹ and the band at 1742 cm⁻¹ due to $\nu(\text{C=O})$, as observed in Figure 9C. This evolution may be associated with collagen aggregation in solution, as observed in a collagen solution left in PBS at RT for 48h (Figure S7, Col + ageing).

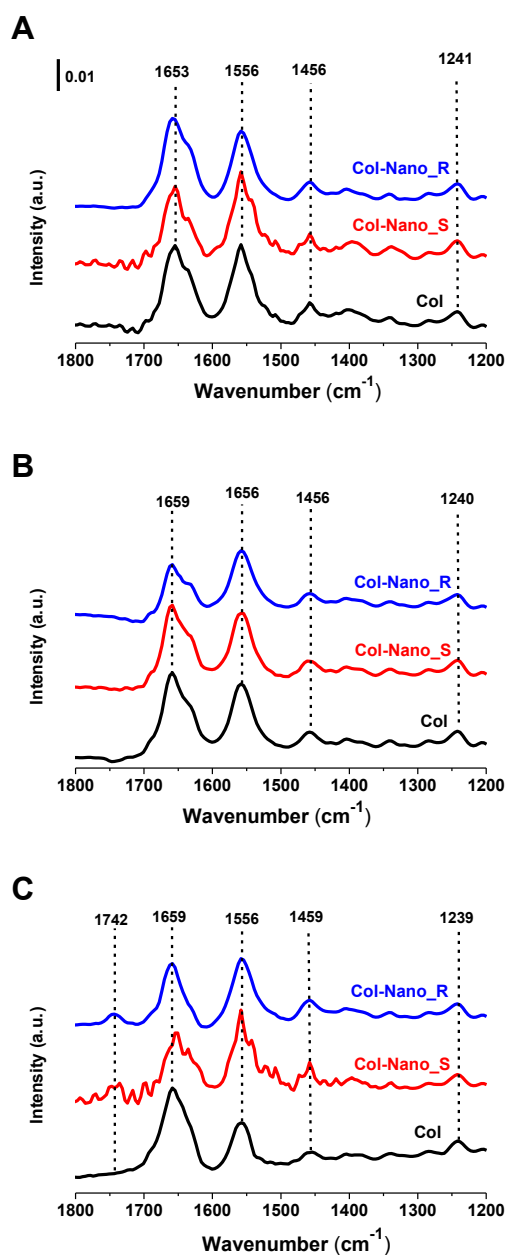


Figure 4.9: IR-ATR analyses of collagen solution (Col) or a mixture of collagen and either TiO₂ nano-spheres (Col-Nano_S) or nano-rods (Col-Nano_R) after a pre-incubation at RT during (A) 20 min or (B) 24h or at (C) 37 °C during 20 min.

Regarding the mechanism of dewetting (*“Mechanism (3)”*), further experiments, similar to those reported by Jacquemart et al.¹⁹, were conducted by varying the velocity of drying. In the present study, the adsorption was performed both on PS and silicon wafer substrates using solutions containing either collagen (Col) or a mixture of collagen and TiO₂ nano-spheres (Col-Nano_S). Furthermore, more than two velocities of drying were used with the aim to deduce a clear trend regarding the presumable dewetting process. Fast drying of about 3, 10 and 40 s was obtained by flashing the samples with nitrogen gas while modulating its flow. Slow drying was obtained by placing the samples, after rinsing, in Petri dishes and letting the liquid evaporating at RT for about 5h. AFM images recorded on the different samples are given in Figure 10. Results clearly show that the morphology of the adsorbed layers is strongly influenced by the velocity of drying. More importantly, the evolution is altered by the presence of nano-spheres in the solution. On PS substrate, the effect of drying may be roughly considered to favor the formation of more continuous layers. On silicon wafer, the evolution is also clear when increasing the velocity of drying, leading to the formation of more rough surfaces with the presence of fibrillar structures. The trend is less pronounced in the presence of TiO₂ nano-spheres. It is worth noting that at the faster drying (~3s), the reproducibility of the results is poor, showing continuous or net-like structure (Figure 10 A, data not shown on silicon wafers).

These findings are different from those reported by Jacquemart et al.¹⁹, as a slow drying on PS substrate leads to a more continuous layer (Figure 10A). This is certainly due to the high sensitivity of the adsorption behavior and organization of collagen to the experimental conditions (procedure of adsorption, rinsing, drying, storing, etc). Whatever the discrepancies with previous findings, our results confirm that drying is an important process influencing the morphology of collagen layers. The addition of TiO₂ nano-spheres seems to do not change the trend, i.e. a faster drying leads to a more continuous layer on PS substrate and a rougher and more filamentous layer on silicon wafer (Figure 10). However, the morphologies obtained in the presence of NPs are radically different.

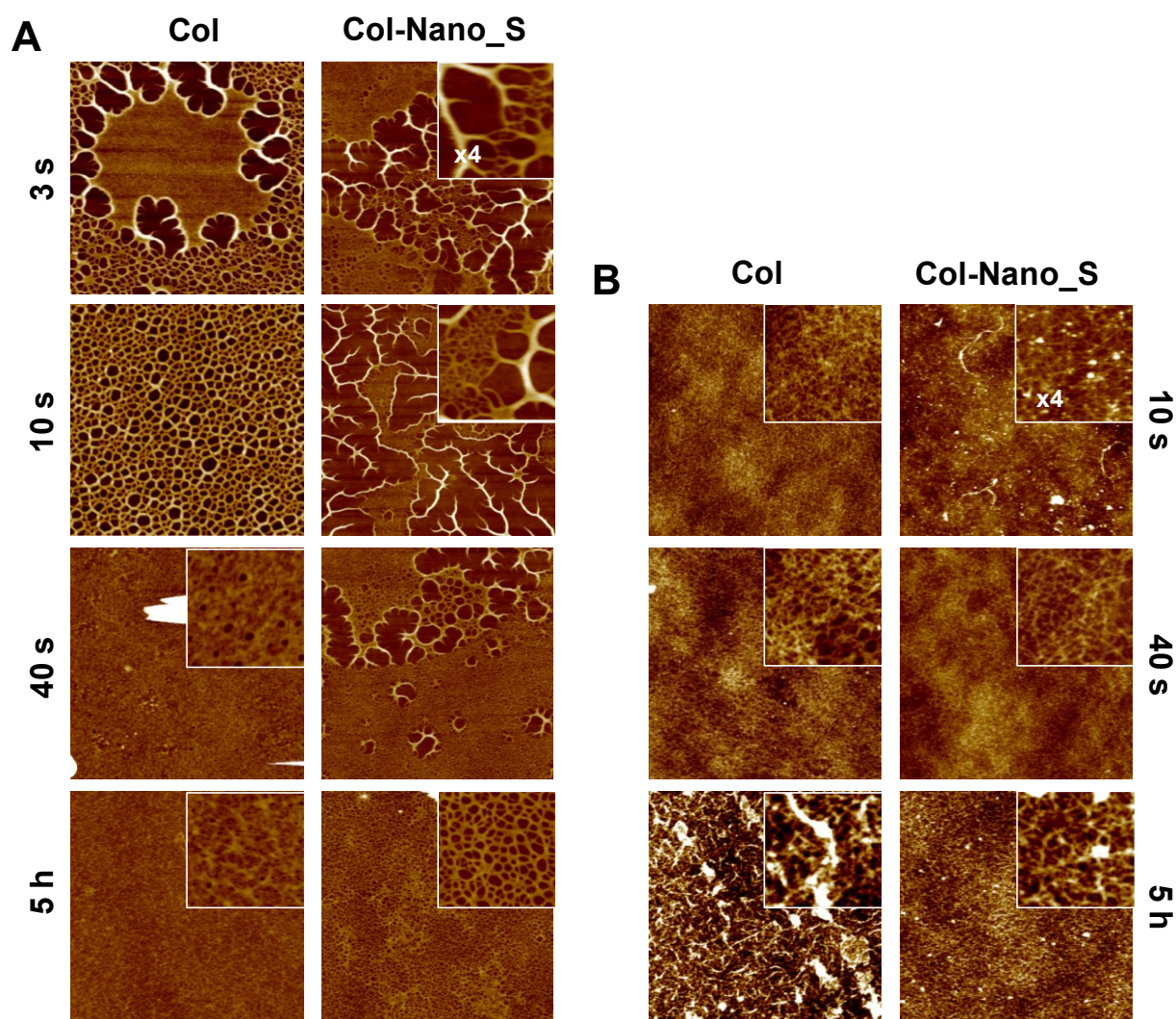


Figure 4.10: Representative AFM height images (4x4 μm², Peak Force Tapping mode, in air, z-scale 20 nm) recorded on (A) PS or (B) silicon substrate after incubation at RT in collagen solution (Col) or a mixture of collagen and TiO₂ nano-spheres (Col-Nano_S) and subsequent drying with different rates, as indicated (duration of drying are approximately: 3s; 10s; 40s and 5h). Insets are zooms of the corresponding images. Pre-incubation of collagen and TiO₂ NPs was performed during 20 min RT.

V. Conclusion

In this work, supramolecular structural changes of collagen in the adsorbed phase were evidenced upon its interaction with TiO₂ NPs in PBS buffer solution. To this end, highly crystalline sphere (6 nm of diameter) and rod-shaped NPs (aspect ratio of about 3) were used. First, collagen was pre-incubated with NPs in PBS either at RT or at 37°C during 20 min or 24h. This solution was then used for adsorption tests; a hydrophobic PS substrate or hydrophilic silicon wafer was incubated at RT during 2h. This strategy aimed to probe supramolecular organization of collagen in the adsorbed phase (dried or hydrated) to identify the possible influence of TiO₂ NPs on the protein structure.

AFM images showed a remarkable effect of the presence of nano-spheres and nano-rods in the pre-incubation solution on the morphology of collagen layer after drying. Moreover, AFM force spectroscopy experiments revealed that adsorbed collagen interact differently whether it was pre-incubated with or without NPs.

It appears that NPs does not co-adsorb with collagen on the substrate. They may influence the dewetting process upon drying, leading to the formation of dried phases with different morphologies. However, our results indicate that dewetting is not solely responsible of the presumable structural changes. The ability of NPs to produce reactive species, which may alter the collagen structure, could not be ruled out. Undoubtedly, the question deserves further investigations.

The complexity of the interaction is inherent in the multiplicity of the parameters influencing this process. Although other parameters such as the conformation of collagen (native vs denatured), the concentration of NPs, incubation time and temperature are also relevant, our results provide new insights regarding the mechanism by which small sized nano-crystals may interact with large-sized proteins. Moreover, this study provides a practical information which may open new routes to elaborate nanostructured bio-interfaces. Indeed, the study can be extended to sensitive polyelectrolytes or other macromolecules with biological interest, including proteins and DNA.

VI. Bibliography

1. Gelse, K., Pöschl, E. & Aigner, T. Collagens - Structure, function, and biosynthesis. *Adv. Drug Deliv. Rev.* **55**, 1531–1546 (2003).
2. Olsen, D. *et al.* Recombinant collagen and gelatin for drug delivery. *Adv. Drug Deliv. Rev.* **55**, 1547–1567 (2003).
3. Persikov, A. V., Ramshaw, J. a M., Kirkpatrick, A. & Brodsky, B. Electrostatic interactions involving lysine make major contributions to collagen triple-helix stability. *Biochemistry* **44**, 1414–1422 (2005).
4. Persikov, A. V., Ramshaw, J. a M., Kirkpatrick, A. & Brodsky, B. Triple-helix propensity of hydroxyproline and fluoroproline: Comparison of host-guest and repeating tripeptide collagen models. *J. Am. Chem. Soc.* **125**, 11500–11501 (2003).
5. Noebe, R. Review of: ' Biomimetic Materials Chemistry ' Edited by Stephen Mann. *Mater. Manuf. Process.* **11**, 893–895 (1996).
6. Weiner, S. & Dove, P. M. An overview of biomineralization processes and the problem of the vital effect. *Rev. Mineral. ...* **54**, 1–29 (2003).
7. Gurdak, E., Rouxhet, P. G. & Dupont-Gillain, C. C. Factors and mechanisms determining the formation of fibrillar collagen structures in adsorbed phases. *Colloids Surfaces B Biointerfaces* **52**, 76–88 (2006).
8. Cisneros, D. a., Friedrichs, J., Taubenberger, A., Franz, C. M. & Muller, D. J. Creating ultrathin nanoscopic collagen matrices for biological and biotechnological applications. *Small* **3**, 956–963 (2007).
9. Miles, C. a. & Bailey, a. J. Thermally labile domains in the collagen molecule. *Micron* **32**, 325–332 (2001).
10. Roach, P., Farrar, D. & Perry, C. C. Surface tailoring for controlled protein adsorption: Effect of topography at the nanometer scale and chemistry. *J. Am. Chem. Soc.* **128**, 3939–3945 (2006).
11. Lundqvist, M. *et al.* Nanoparticle size and surface properties determine the protein corona with possible implications for biological impacts. *Proc. Natl. Acad. Sci. U. S. A.* **105**, 14265–14270 (2008).
12. Mauquoy, S. *et al.* Biointerfaces Designed Through Directed Collagen Assembly. *Journal of Bionanoscience* **8**, 407–418

13. Gurdak, E., Dupont-Gillain, C. C., Booth, J., Roberts, C. J. & Rouxhet, P. G. Resolution of the vertical and horizontal heterogeneity of adsorbed collagen layers by combination of QCM-D and AFM. *Langmuir* **21**, 10684–10692 (2005).
14. Caballero, L., Mena, J., Morales-alvarez, A., Kogan, M. J. & Melo, F. Assessment of the Nature Interactions of β - Amyloid Protein by a Nanoprobe Method. (2015).
15. Gautieri, A., Vesentini, S., Redaelli, A. & Buehler, M. J. Hierarchical structure and nanomechanics of collagen microfibrils from the atomistic scale up. *Nano Lett.* **11**, 757–766 (2011).
16. Ramesh Kumar, M., Merschrod S., E. F. & Poduska, K. M. Correlating mechanical properties with aggregation processes in electrochemically fabricated collagen membranes. *Biomacromolecules* **10**, 1970–1975 (2009).
17. Gutsman, T. *et al.* Force spectroscopy of collagen fibers to investigate their mechanical properties and structural organization. *Biophys. J.* **86**, 3186–3193 (2004).
18. Dupont-Gillain, C. C. Understanding and controlling type I collagen adsorption and assembly at interfaces, and application to cell engineering. *Colloids Surf. B. Biointerfaces* **124**, 87–96 (2014).
19. Jacquemart, I., Pamula, E., De Cupere, V. M., Rouxhet, P. G. & Dupont-Gillain, C. C. Nanostructured collagen layers obtained by adsorption and drying. *J. Colloid Interface Sci.* **278**, 63–70 (2004).
20. Maachou, H., Genet, M. J., Aliouche, D., Dupont-Gillain, C. C. & Rouxhet, P. G. XPS analysis of chitosan–hydroxyapatite biomaterials: from elements to compounds. *Surf. Interface Anal.* **45**, 1088–1097 (2013).
21. Uchino, T., Tokunaga, H., Ando, M. & Utsumi, H. Quantitative determination of OH radical generation and its cytotoxicity induced by TiO₂-UVA treatment. *Toxicol. Vitro.* **16**, 629–635 (2002).

Appendix I

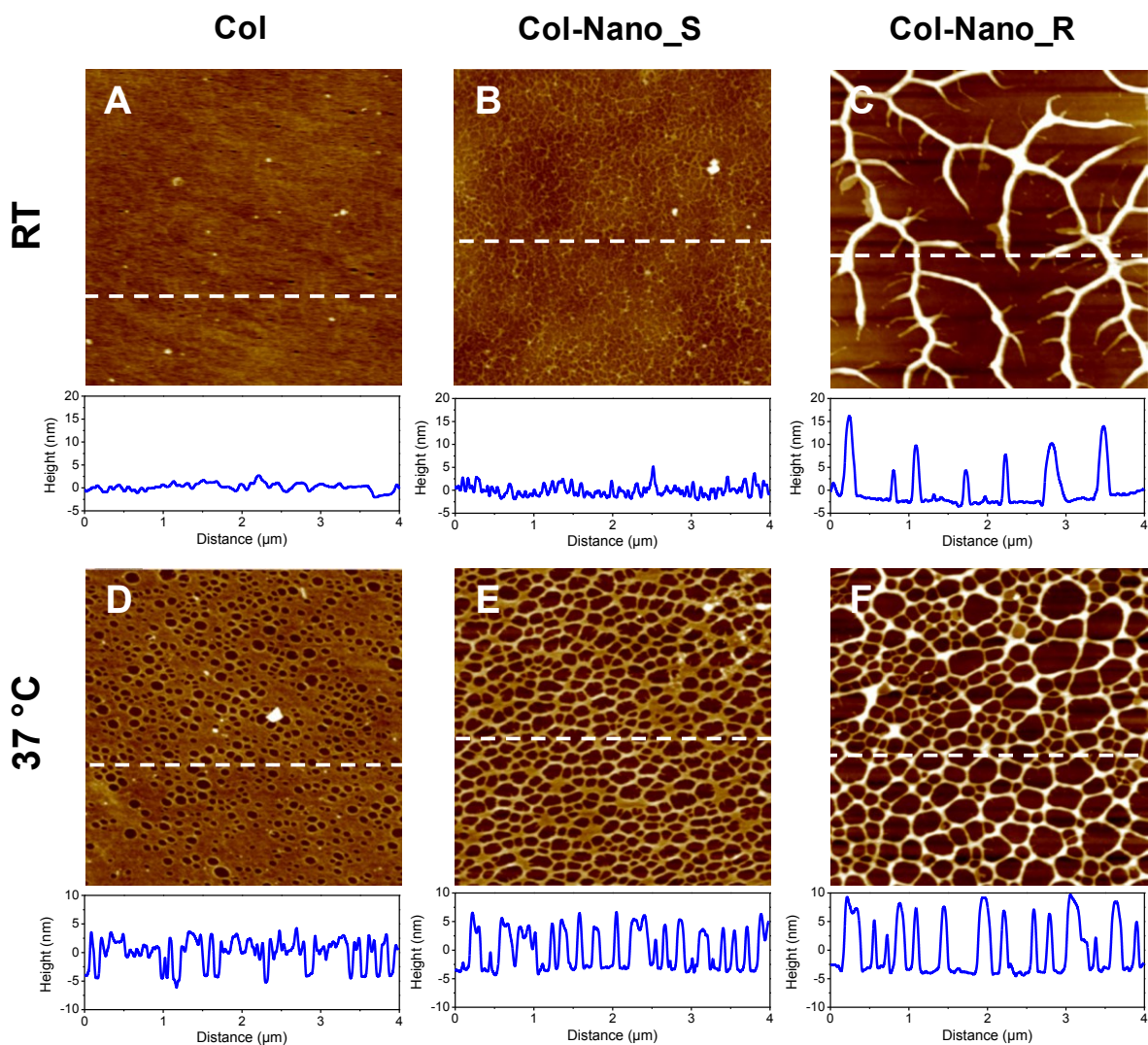


Figure S1. Representative AFM height images (1×1 μm², Peak Force Tapping mode, in air, z-scale 20 nm) recorded on PS substrate after incubation at RT (A) at 37 °C (D) in collagen solution (Col) or a mixture of collagen and either TiO₂ (B, E) nano-spheres (Col-Nano_S) or (C, F) nano-rods (Col-Nano_R) and subsequent drying. Pre-incubation of collagen and TiO₂ NPs was performed during 24h at (A, B, C) RT or (D, E, F) 37 °C. Cross sections were taken at the locations indicated by dashed lines.

Appendix II

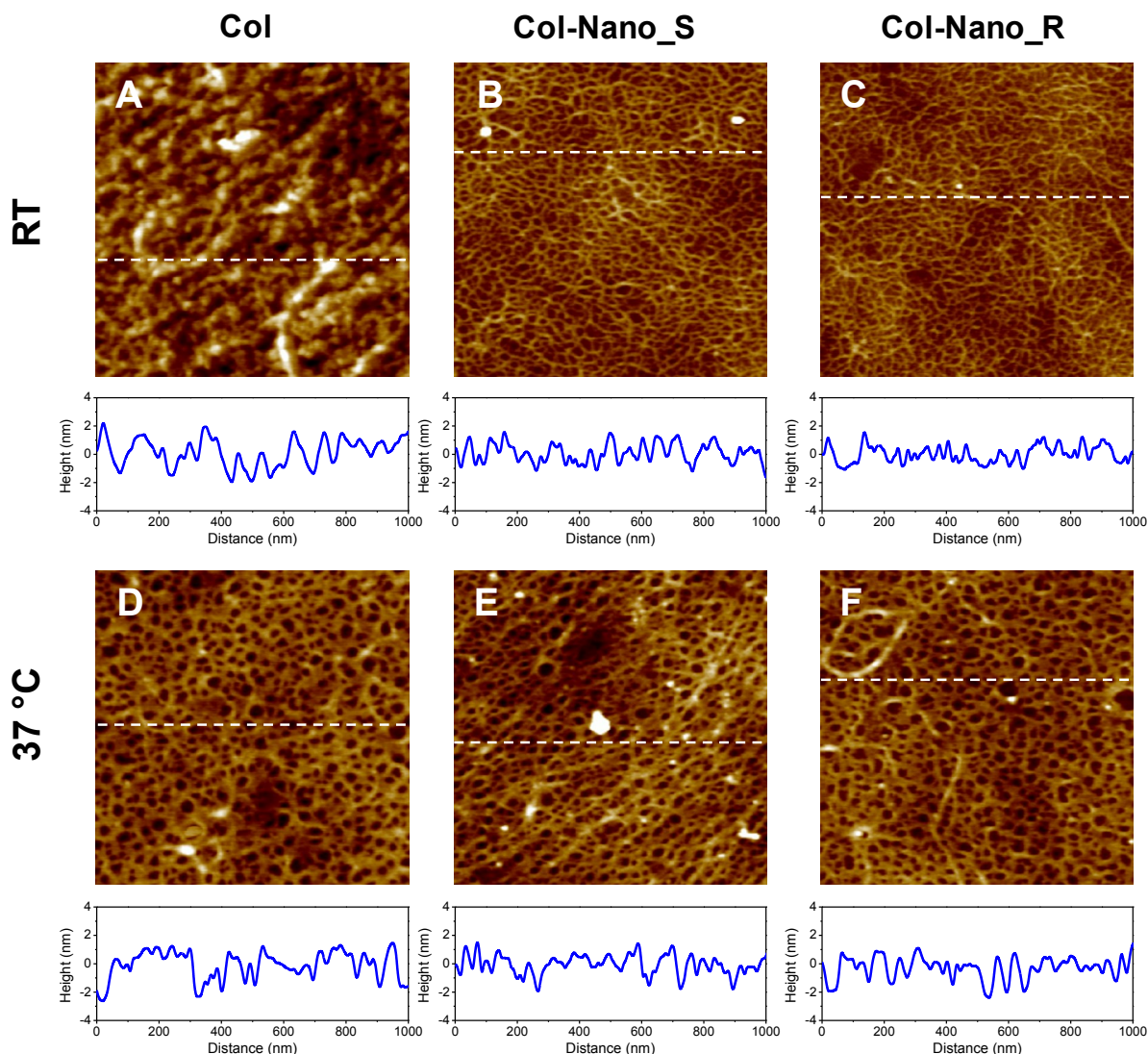


Figure S2. Representative AFM height images (1×1 μm², Peak Force Tapping mode, in air, z-scale 8 nm) recorded on silicon substrate after incubation at RT (A) at 37°C (D) in collagen solution (Col) or a mixture of collagen and either TiO₂ (B, E) nano-spheres (Col-Nano_S) or (C, F) nano-rods (Col-Nano_R) and subsequent drying. Pre-incubation of collagen and TiO₂ NPs was performed during 24h at (A, B, C) RT or (D, E, F) 37 °C. Cross sections were taken at the locations indicated by dashed lines.

Appendix III

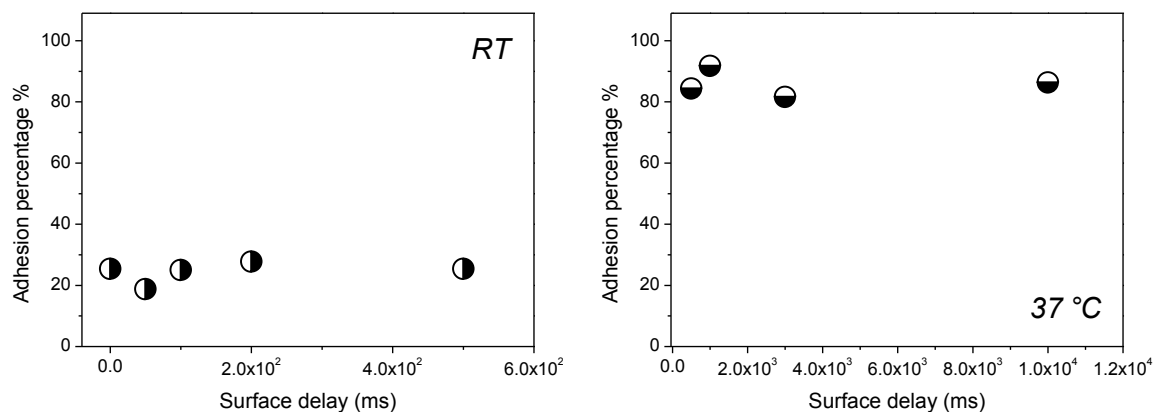


Figure S3. Evolution of the percentage of adhesion (probability of occurrence of adhesion events) as a function of surface delay (residence time) recorded on silicon wafer after the adsorption of collagen (Col solution). The pre-incubation was performed at RT (left) or at 37°C (right).

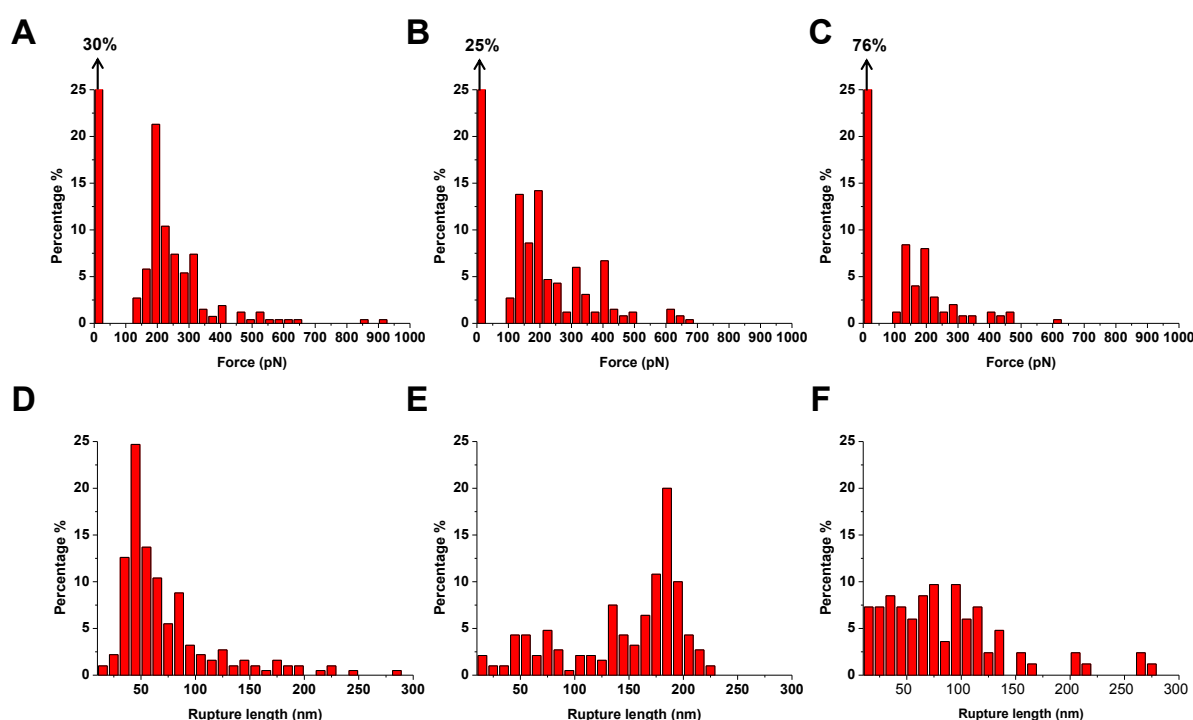


Figure S4. (A-C) Adhesion force histograms and (D-F) rupture length histograms obtained by recording force-distance curve **on PS substrate** after incubation at RT in (A, D) collagen solution (Col) or a mixture of collagen and either TiO₂ (B, E) nano-spheres (Col-Nano_S) or (C, F) nano-rods (Col-Nano_R) and subsequent rinsing with PBS. Pre-incubation of collagen and TiO₂ NPs was performed during 20 min at RT. The data shown correspond to 768 force-distance curves obtained from three independent experiments.

Appendix IV

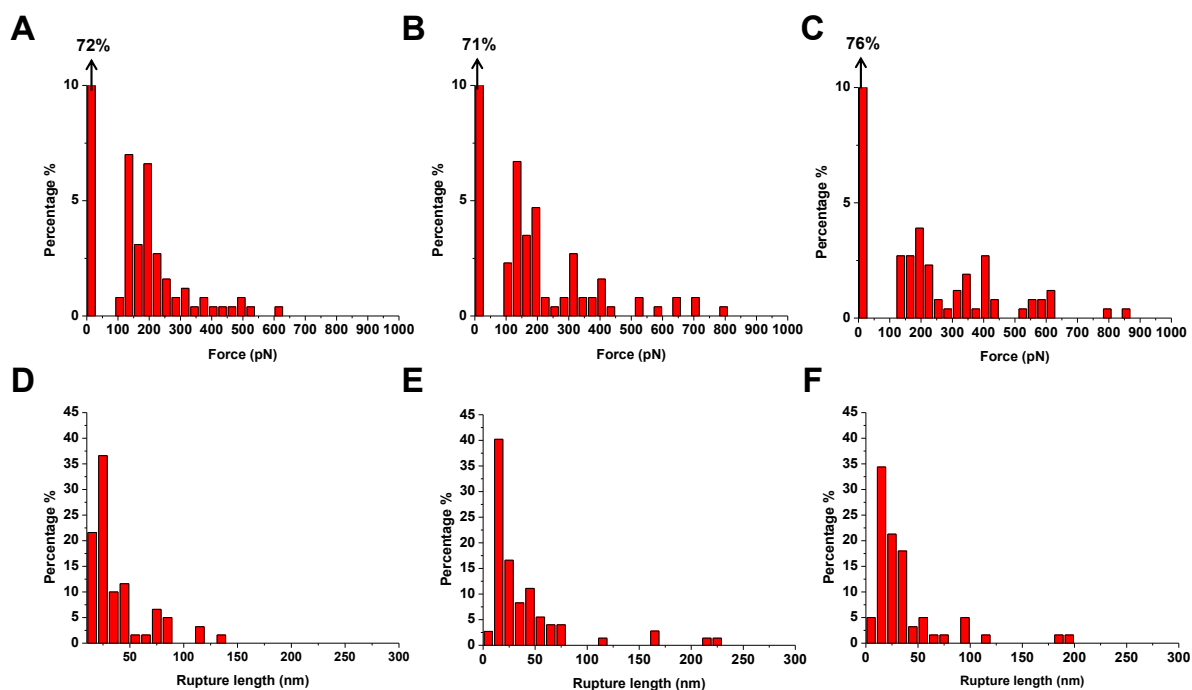


Figure S5. (A-C) Adhesion force histograms and (D-F) rupture length histograms obtained by recording force-distance curve **on silicon wafer** after incubation at RT in (A, D) collagen solution (Col) or a mixture of collagen and either TiO₂ (B, E) nano-spheres (Col-Nano_S) or (C, F) nano-rods (Col-Nano_R) and subsequent rinsing with PBS. Pre-incubation of collagen and TiO₂ NPs was performed during 20 min at RT. The data shown correspond to 768 force-distance curves obtained from three independent experiments.

Appendix V

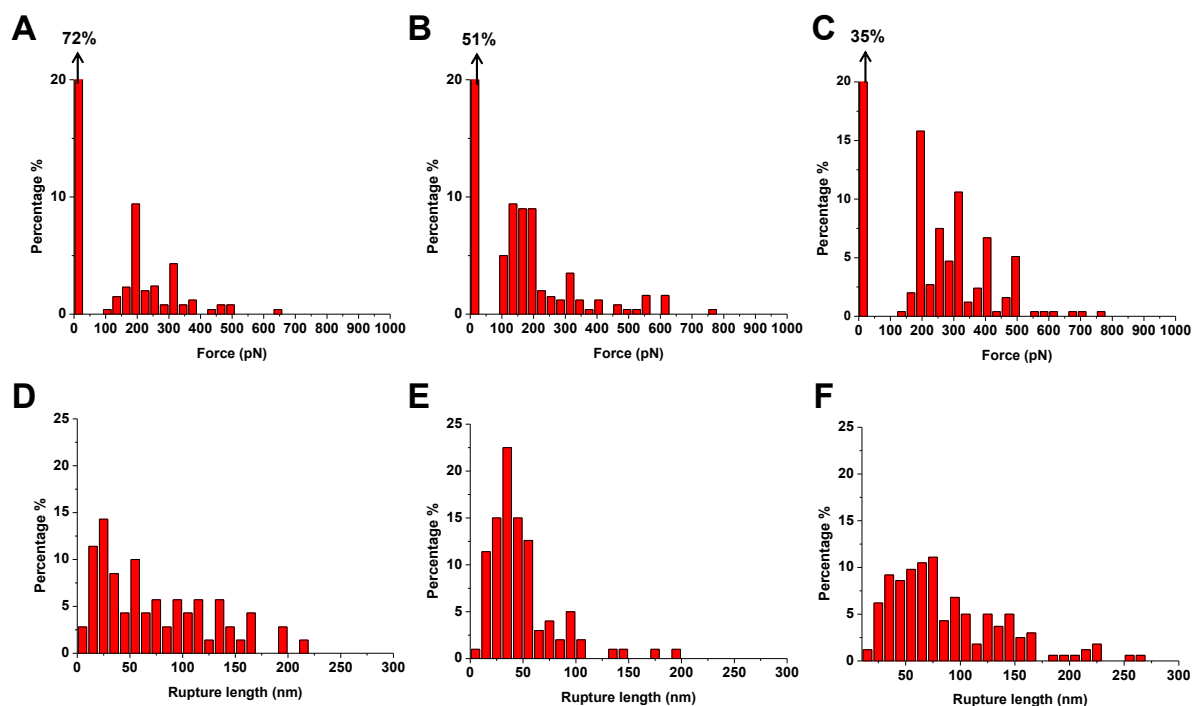


Figure S6. (A-C) Adhesion force histograms and (D-F) rupture length histograms obtained by recording force-distance curve **on silicon wafer** after incubation at RT in (A, D) collagen solution (Col) or a mixture of collagen and either TiO₂ (B, E) nano-spheres (Col-Nano_S) or (C, F) nano-rods (Col-Nano_R) and subsequent rinsing with PBS. Pre-incubation of collagen and TiO₂ NPs was performed during 24h at RT. The data shown correspond to 768 force-distance curves obtained from three independent experiments.

Appendix VI

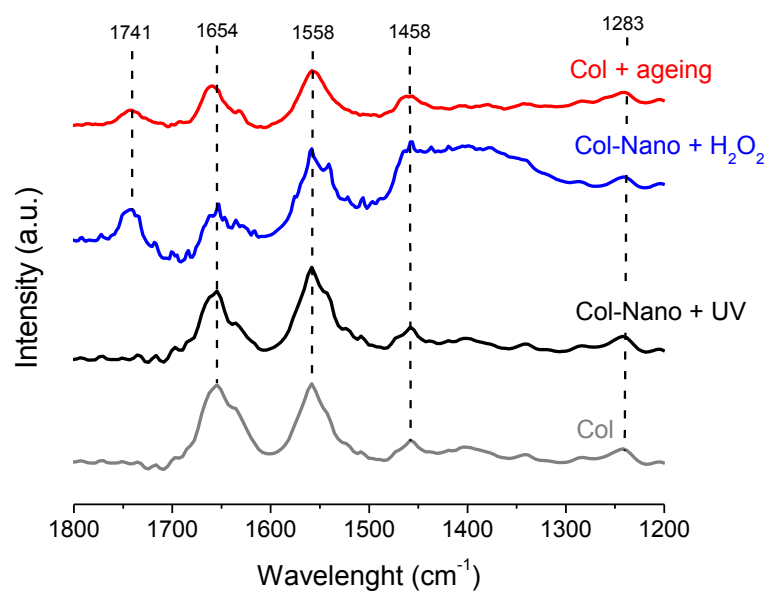


Figure S7. IR-ATR analyses of collagen solution (Col) or modified collagen (ageing) with or without TiO₂ nano-spheres (Col-Nano) at RT during 24h under different conditions.

Chapter 5: Interaction of TiO₂ NPs with HSA and fibrinogen proteins in solution and in the adsorbed phase

Table of contents

Chapter 5: Interaction of TiO₂ NPs with HSA and fibrinogen proteins in solution and in the adsorbed phase	143
I. Introduction	145
II. Interaction process in liquid phase	147
A. Organization of the protein layer in the hydrated state	147
B. Characterization of the protein-nanoparticle interaction in solution.....	151
III. Interaction process in the adsorbed dried phase	153
A. XPS measurements on adsorbed protein layer in dried phase	153
B. Organization of the protein layer in dried state.....	156
IV. Events in liquid phase	159
A. Mechanism of fibrinogen-TiO ₂ NPs interaction in solution.....	159
B. Mechanism of HSA-TiO ₂ NPs interaction in solution	160
V. Events in the adsorbed phase	161
A. Mechanism of fibrinogen-TiO ₂ NPs interaction in dried state.....	162
B. Mechanism of HSA-TiO ₂ NPs interaction in dried state.....	162
VI. Conclusion	162
VII. Bibliography.....	164

I. Introduction

The formation of the protein corona has a considerable influence on the physiochemical properties of NPs such as bio-distribution or internalization. Some studies have focused on the interaction of TiO₂ NPs and plasmatic proteins^{1,2}, therefore, the relationship between the protein nanoparticle interaction in solution and the resulting behavior of adsorbed protein is not clear. The parameters of NPs³ (size, shape, and surface area) determine the interaction with the proteins and may influence the adsorbed protein.

The aim of this work is to probe the interaction process between two plasmatic proteins, the human serum albumin (HSA) and the fibrinogen (Fg) with sphere or rod-shaped TiO₂ NPs in a buffer solution (PBS) and to evaluate the resulting consequences on the ability of the proteins to self-assemble and self-organize in the adsorbed phase. HSA is the most abundant plasmatic proteins (50-60% of all blood proteins), though HSA has no cell receptor for its recognition, it is interesting to investigate HSA adsorption on a surface, indeed, Keogh et al., found that the surface will be passivated against clotting⁴. HSA is a soft protein⁵ possessing a low internal stability, which undergoes denaturation and easy adsorption. The equilibrium state adsorption of HSA on a surface takes place in the first min, depending on pH and ionic strength. At physiological pH, HSA has a negative net charge surface, and the adsorption processes by electrostatic interaction by a complex series of adsorption and displacement⁶. Although fibrinogen represents around 5% of blood proteins, it is the most abundant protein involved in the coagulation. Once fibrinogen is polymerized, it results a fibrin clot which induces cell adhesion⁷. Fibrinogen is a molecule with high surface affinity⁸, possessing a negative net charge at pH 7.4. Comparing Fg and HSA, Fg molecule has the smallest diffusion constant, but the biggest mass⁹, while HSA has the highest diffusion constant and lowest mass. Resulting of these differences in size and diffusion constant, HSA is known to have a reversible adsorbed process contrary to Fg¹⁰, especially in dry and adsorbed phase fibrinogen interacts more with the hydrophilic surface than HSA¹¹.

A particular attention is dedicated to the two different adsorption procedures (see chapter 2 section: II F and G). Interaction in solution was investigated after pre-incubation of protein-TiO₂ NPs at room temperature (RT) or at 37 °C for 20 min or 24h by liquid ATR. In liquid investigations of adsorbed proteins were performed after immersion of silicon wafers in the pre-incubated suspension (procedure I), while, investigations in air adsorbed phase were provided after consecutive incubation of silicon wafer in protein solution and NPs suspension respectively (procedure II). This strategy offers many advantages. First, one observes the sensitivity of the supramolecular organization of proteins on solid surfaces to their various physicochemical properties and their environment.

Second, the use of AFM allows imaging adsorbed proteins on surfaces under aqueous and at physiological conditions, with a molecular resolution especially when the substrate is a flat surface (such as silicon wafer). AFM images give information on the structure and structural rearrangement of the adsorbed protein layers. The dimension and conformation of individual fibrinogen and HSA molecules has already been examined by AFM on a variety of surfaces, including SiO₂ and TiO₂ substrate^{12,13}. Third, the structural change of proteins in solution in the presence of TiO₂ NPs is characterized by liquid ATR. Raman spectroscopy is a suitable method to investigate the conformation of the proteins in aqueous solution, providing information on the involved mechanism by which TiO₂ NPs may interact with proteins. Then, the adsorbed protein layer was investigated by XPS. XPS is used to analyze the amount of proteins adsorbed onto silicon substrate, by analyzing the atomic percentage it is possible to have an estimation of protein density and coverage of the adsorbed protein film¹⁴.

II. Interaction process in liquid phase

A. Organization of the protein layer in the hydrated state

Surfaces were analyzed using peak force tapping (PFT) mode AFM liquid and air. Figure 1 (B) shows the PFT mode AFM liquid topographic image of a 2 μm^2 area and cross section of the SiO₂ substrate before protein adsorption. The sample is generally slightly roughened at the nanometer scale as it is shown in the cross section profile of Figure 1. The interaction between the tip and the sample changes in liquid and causes different morphologies in air and in water (figure1: A and B), roughness value in air is around 0.3nm whereas the roughness value in liquid is around 0.45 nm (values for 2*2 μm area).

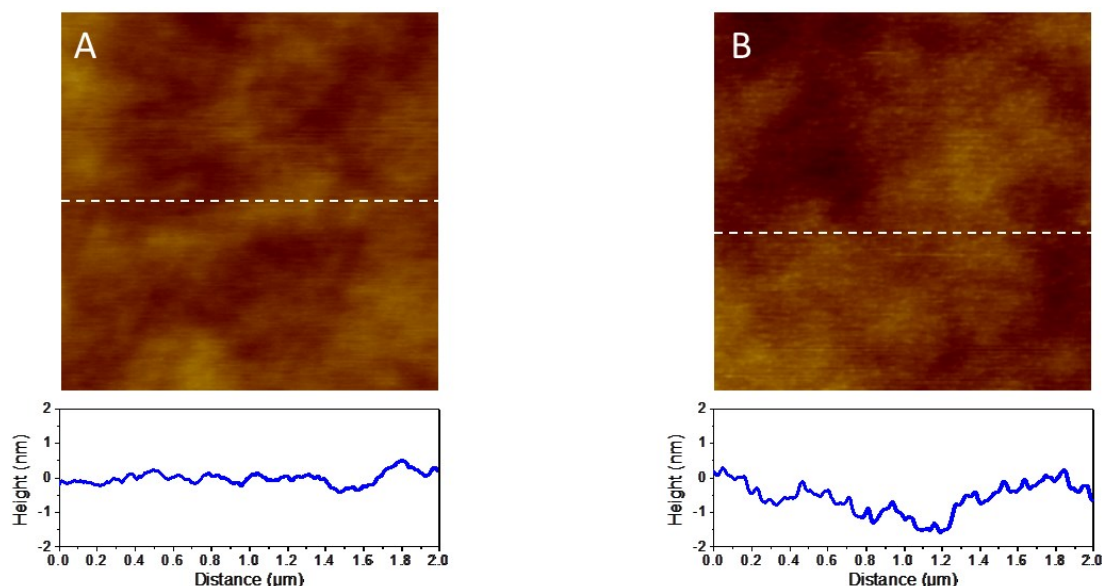


Figure 5.1: AFM images (2 $\mu\text{m} \times 2 \mu\text{m}$) of a clean SiO₂ substrate surface, z-scale -4/4nm: (A) topography image PFT mode in air, (B) topography image PFT mode in liquid. Cross section were taken at the location indicated by dashed lines

Proteins and NPs were pre-incubated either at RT or at 37°C during 20 min or 24h in PBS solution, then, silicon wafer was immersed in the suspension. Figure 2 and 3 show topographical AFM images of adsorbed HSA and fibrinogen onto silicon substrate. Surface covered by the proteins showed an increase of the roughness and different pattern compared to without proteins, confirming the formation of adsorbed protein films.

a. Organization of HSA layer in the hydrated state

In the case of HSA without NPs the greatest roughness value is obtained for the long incubation time and higher temperature (0.86 nm). A first observation is that the roughness value increases in the presence of NPs whatever the experimental condition. More interestingly, in the presence of NPs the roughness value seems to depend only on the incubation temperature, the more important roughnesses are obtained for 37°C of incubation temperature with TiO₂ NPs. This is traduced by the appearance of aggregates in the presence of NPs as shown on figure 2 at 20 min and 37°C and on figure S1 (appendix I). The cross sections suggest the formation of aggregates with similar height (5 nm) and forms on the surface (figure 2: E and F). For these experimental conditions in the presence of nano-spheres, the aggregates seem larger on the surface than in the presence of nano-rods, this observation is to relativize and may be due to an artefact effect of the AFM probe. For 20min of incubation time at 20°C in the presence of NPs images shows a relatively flat protein film as shown on figure 2: A and B and on the corresponding cross section. For these experimental conditions very few aggregates are observed, therefore, the protein film seems altered compared to without NPs and presents the apparition of holes with a depth around 2.5 nm suggesting an adsorbed monolayers of proteins. For the two temperatures of pre-incubation no effect of particle shapes is observed.

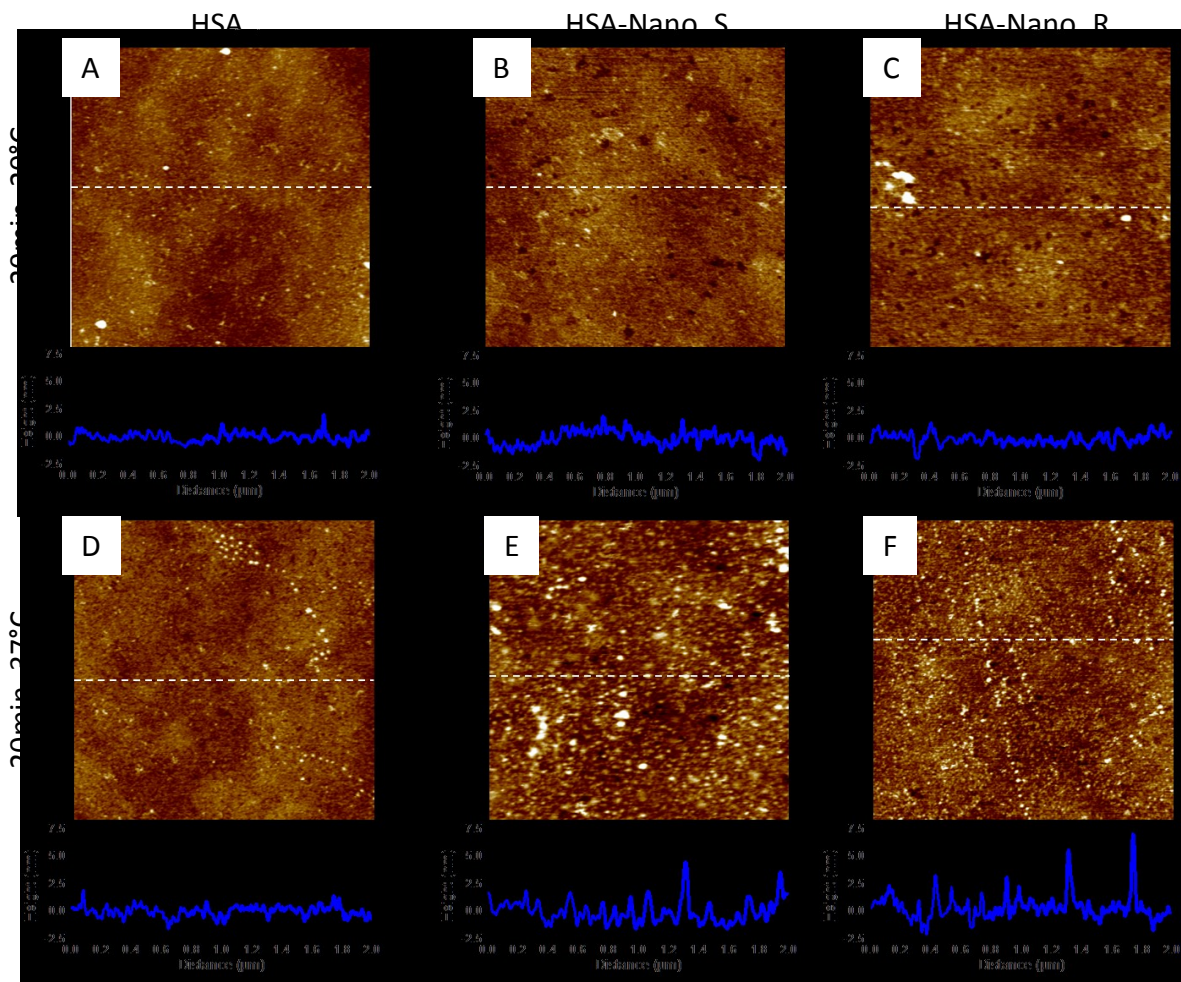


Figure 5.2: AFM topography images (PFT mode) in liquid (2 μm *2 μm) of a SiO₂ substrate surface with HSA adsorbed, z-scale -4/4 nm: (A) 20 min 20°C without NPs, (B) 20 min 20°C with nano-spheres, (C) 20 min 20°C with nano-rods, (D) 20 min 37°C without NPs, (E) 20 min 37°C with nano-spheres, (F) 20 min 37°C with nano-rods. Cross section were taken at the location indicated by dashed lines

b. Organization of fibrinogen layer in the hydrated state

Fibrinogen displays an opposite behavior compared to HSA, the smallest roughness value without NPs is obtained for the longest pre-incubation time and the highest temperature of incubation (1.1 nm). AFM images figure 3 (A and D) and figure S2 (appendix II) show the effect of the pre-incubation time on fibrinogen adsorption. For the longest time of pre-incubation a homogenous protein film without aggregates is observed, the corresponding cross section suggests an adsorbed monolayer, while, for 20 min the formation of clusters with a typical height of 3 nm is observed, this observation suggests a time dependence of adsorbed fibrinogen layer. In the presence of nanoparticle this time dependence disappears, AFM images of figure 3 (B, C, E and F) present a similar pattern of the adsorbed layers whatever the incubation time. They are two interesting observations in the presence of NPs on the roughness value. First, a general decrease in the roughness value is observed for all the experimental conditions in the presence of TiO₂ NPs. Second, the roughness values become similar

whatever the selected experimental conditions of pre-incubation in the presence of TiO₂ NPs. For the two times of pre-incubation no effect of particles shapes is observed.

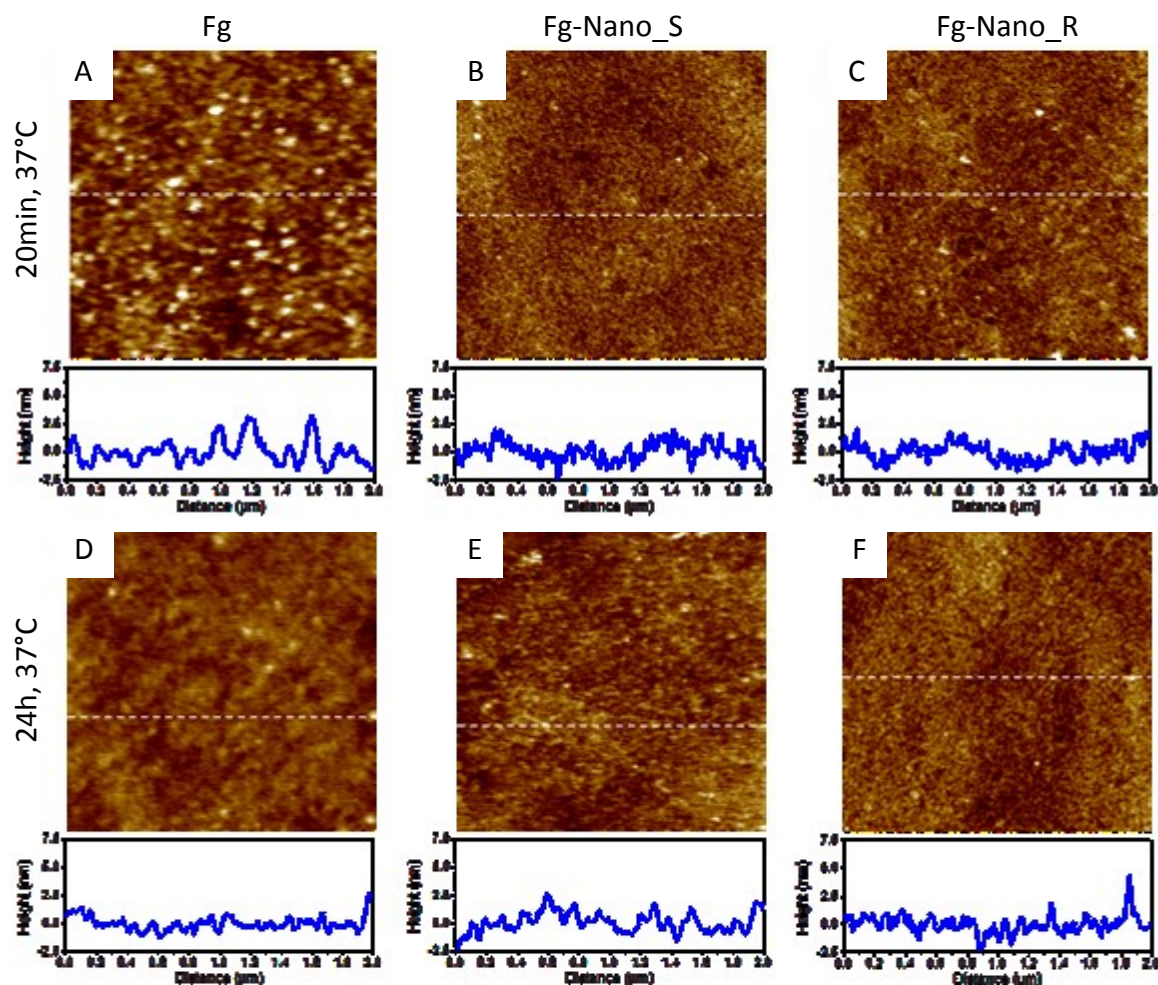


Figure 5.3: AFM topography image PFT mode in liquid (2 μm *2 μm) of a SiO₂ substrate surface with fibrinogen adsorbed, z-scale -4/4 nm: (A) 20 min 37°C without NPs, (B) 20 min 37°C with nano-spheres, (C) 20 min 37°C with nano-rods, (D) 24 h 37°C without NPs, (E) 24 h 37°C with nano-spheres, (F) 24 h 37°C with nano-rods. Cross section were taken at the location indicated by dashed lines

Figure 4 shows the variation of roughness values for adsorbed HSA and fibrinogen on silicon wafer for the different condition of time and temperature pre-incubation. The roughness of the HSA layer presents change only for the highest incubation temperature in the presence of TiO₂ NPs, contrary to the fibrinogen, which presents regular roughness values in the presence of TiO₂ NPs.

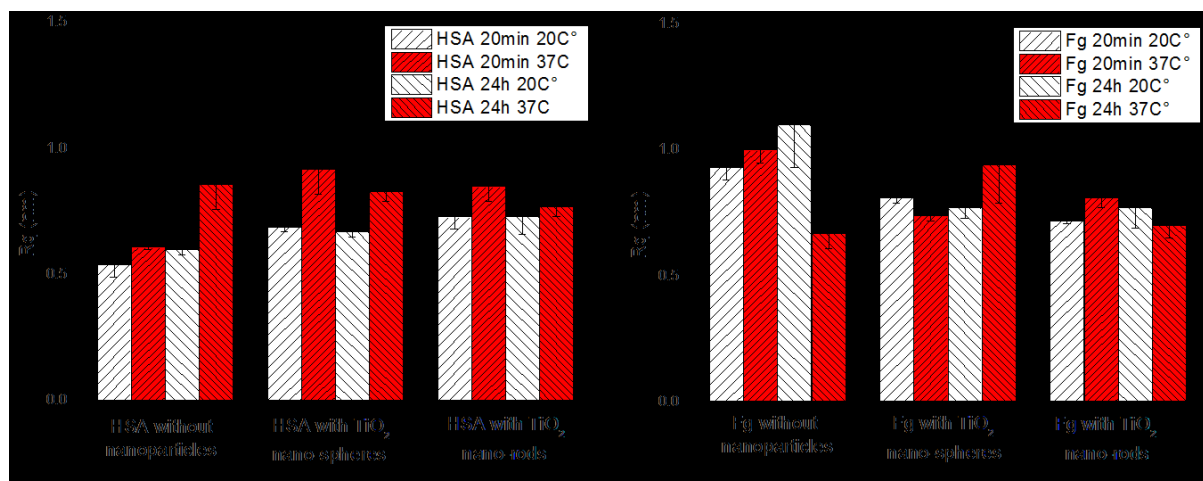


Figure 5.4: Surface roughness of SiO₂ with adsorbed proteins with and without TiO₂ NPs: A Si surface with HSA adsorbed; B Si surface with fibrinogen adsorbed

B. Characterization of the protein-nanoparticle interaction in solution

Proteins and NPs were pre-incubated either at RT or at 37°C during 20 min or 24h in PBS solution before IR-ATR measurements. IR-ATR is a powerful method for investigating the secondary structure of proteins in liquid. In the IR region, the amide I-II vibrations are sensitive to the secondary structure of the proteins. The amide I vibration (1700–1600 cm⁻¹ region) is primarily attributed by C=O stretching vibrations; the amide II vibration (1600–1480 cm⁻¹ region) contains information from the in-plane N-H bend and C-N stretch of the amide bond. Amide I band is known to be more sensitive to structural changes of secondary structure than the amide II band. The amide I bands contains β -sheet between: 1610-1640, random coil: 1640-1650, α -helix: 1650-1658 and β -turn structure: 1660-1700cm⁻¹, in the case of fibrinogen amide I bands contains vibration corresponding to the side chains and extended side chains. By comparing the intensity ratio between the amide I and II band, qualitative information may be provided on the conformational change of secondary structure.

a. IR-ATR analyze of HSA in solution

In the case of the HSA, the amide I band includes signals from the three β -sheet, α -helix and β -turn structures, where α -helix is the principal contribution. For the pre-incubation time of 20 min, a change in relative intensities between amide I and amide II band is observed in the presence of nano-rods comparing without NPs and nano-spheres which are of the same order (0.6 and 0.8 respectively) as shows on Table 1 and figure 5, suggesting a change in the contribution of α -helix in the presence of nano-rods. The contribution of β -sheet and β -turn structure (1630 cm⁻¹ and 1680 cm⁻¹ respectively) shows no variation for HSA and HSA_Nano-S. For 24h of pre-incubation time the obtained spectrum in the presence of NPs are comparable (see table 1), indicating the influence of time incubation on HSA-TiO₂ NPs interaction.

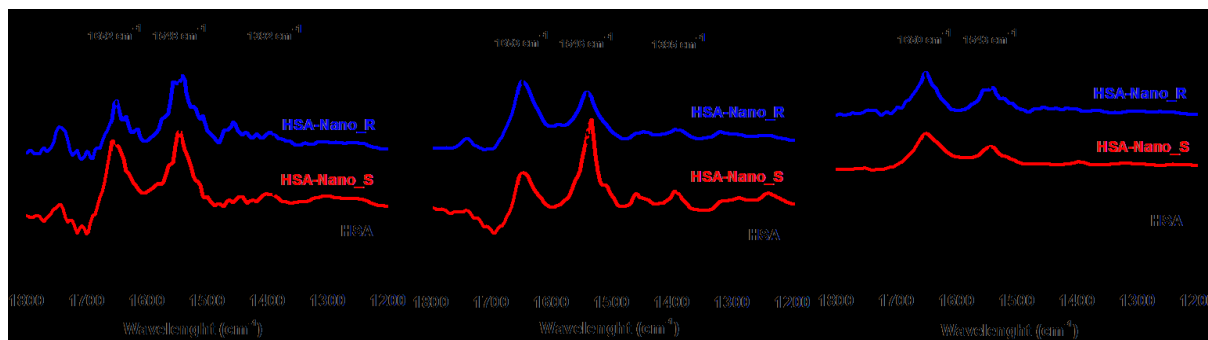


Figure 5.5: Liquid ATR spectra of HSA, (A) 20°C 20 min, (B) 37°C 20 min, (C) 20°C 24 h. HSA: Human serum albumin without NPs, HSA-Nano_S: HSA with nano-spheres, HSA-Nano_R: HSA with nano-rods

b. IR-ATR analyze of fibrinogen in solution

In the case of fibrinogen no significant change in the amideI/amideII ratios is observed as shown on table1. This observation suggests that the secondary structures of fibrinogen in solution are weakly impacted by the different experimental conditions and by the presence of NPs. Figure 6 shows the liquid IR-ATR spectra of fibrinogen, the principal peak at 1648 cm^{-1} has for principal component the α -chains contribution and presents no variation, indicating that the α -chains are not altered. A slight change is observed around 1675 cm^{-1} at 20min and 20°C (figure6: A) comparing with and without NPs. This observation is probably due to a slight change of β -sheets and β -turns secondary structures in the presence of NPs. At 20 min and 37°C (figure 6: B) a shoulder peak around 1620 cm^{-1} is observed in the presence of NPs.

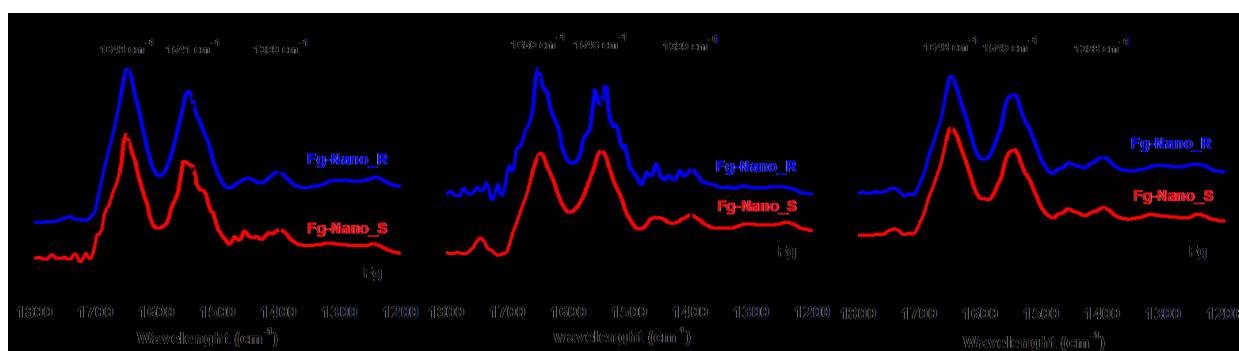


Figure 5.6: Liquid ATR spectra of Fibrinogen, (A) 20°C 20 min, (B) 37°C 20 min, (C) 20°C 24 h. Fg: fibrinogen without NPs, Fg-Nano_S: Fibrinogen with nano-spheres, Fg-Nano_R: Fibrinogen with nano-rods

	20min-20C°	20min-37C°	24h-20C°
HSA	1.1	0.5	3.3
HSA-Nano_S	0.8	0.4	1.7
HSA-Nano_R	0.6	1.2	1.6
Fg	1.1	1.1	1.3
Fg -Nano_S	1.3	1	1.3
Fg -Nano_S	1.2	1.3	1.2

Table 5.1: Intensity ratio AmideI/AmideII (I_{1650}/I_{1550}) of liquid ATR spectra.

III. Interaction process in the adsorbed dried phase

Investigations in air of the adsorbed phase were obtained after consecutive incubation of silicon wafer in protein solution during 2h at RT and in a nanoparticle suspension during 24h at RT.

A. XPS measurements on adsorbed protein layer in dried phase

XPS was used to investigate the chemical composition of the surface with and without adsorbed protein. The survey scans of adsorbed HSA and fibrinogen on silicon surface are showed in figure 7. The signal at 400 eV assigned to N1s band appears after protein adsorption. An increase of C1s band intensity as well as a decrease of Si2p signal is observed after protein adsorption. After protein adsorption the deconposition of the C1s peak gives three different peaks, the first one at 284.8 eV is assigned to carbon in saturated and unsaturated hydrocarbon groups, the second peak at 285.2 eV is related to C-NH amine groups and the last peak detected at 287.4 eV is for the peptide bond HN-C=O (figure 8). These data indicated the presence of proteins on the surface after the steps of rinsing and drying.

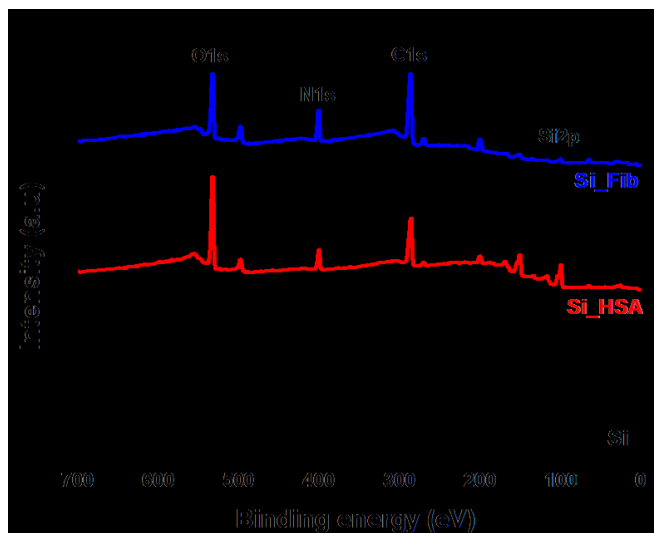


Figure 5.7: XPS survey scans of silicon surface (black-line), silicon surface with adsorbed HSA (red-line) and after adsorption fibrinogen (blue-line).

By XPS data treatment, the relative atomic composition (atom %) of surface samples after proteins adsorption on Si surface was calculated for HSA and fibrinogen with and without NPs (table2). The first and common observation in both cases (HSA and fibrinogen adsorption) is that the signal of Ti2p is detected only in the presence of TiO₂ nano-spheres in very small quantity considering the intensity of Ti2p signal suggesting the absence of nano-rods on the surface. The relative Si percentage between HSA and fibrinogen shows significant change (24% for HSA and 12% for fibrinogen), suggesting a better surface coverage of fibrinogen during the adsorption on the surface.

In the case of HSA a decrease of relative Si percentage is observed in the presence of NPs and significant changes in atomic percentage are observed in the presence of nano-rods. With nano-rods a decreasing of atomic percentage of Si2p, O1s and N1s is observed, while an increasing of C1s intensity is observed. Regarding the corresponding C1s spectra (figure 8) for adsorbed HSA the contribution of peptide bond HN-C=O at 287.4 eV shows a spectacular decrease in the presence of nano-rods compared to without NPs and with nano-spheres suggesting the presence of contamination on the surface.

While for the fibrinogen, the presence of NPs leads to an increase of the relative Si percentage, suggesting a lower surface coverage in the presence of NPs. No significant changes are observed for C1s, N1s and O1s signal. The study of C1s and N1s spectra (figure 8) shows any variation in the contribution of different binding energy and relative intensity contrary to the HSA in the presence of NPs, indicating that fibrinogen is adsorbed in the same proportion on the surface.

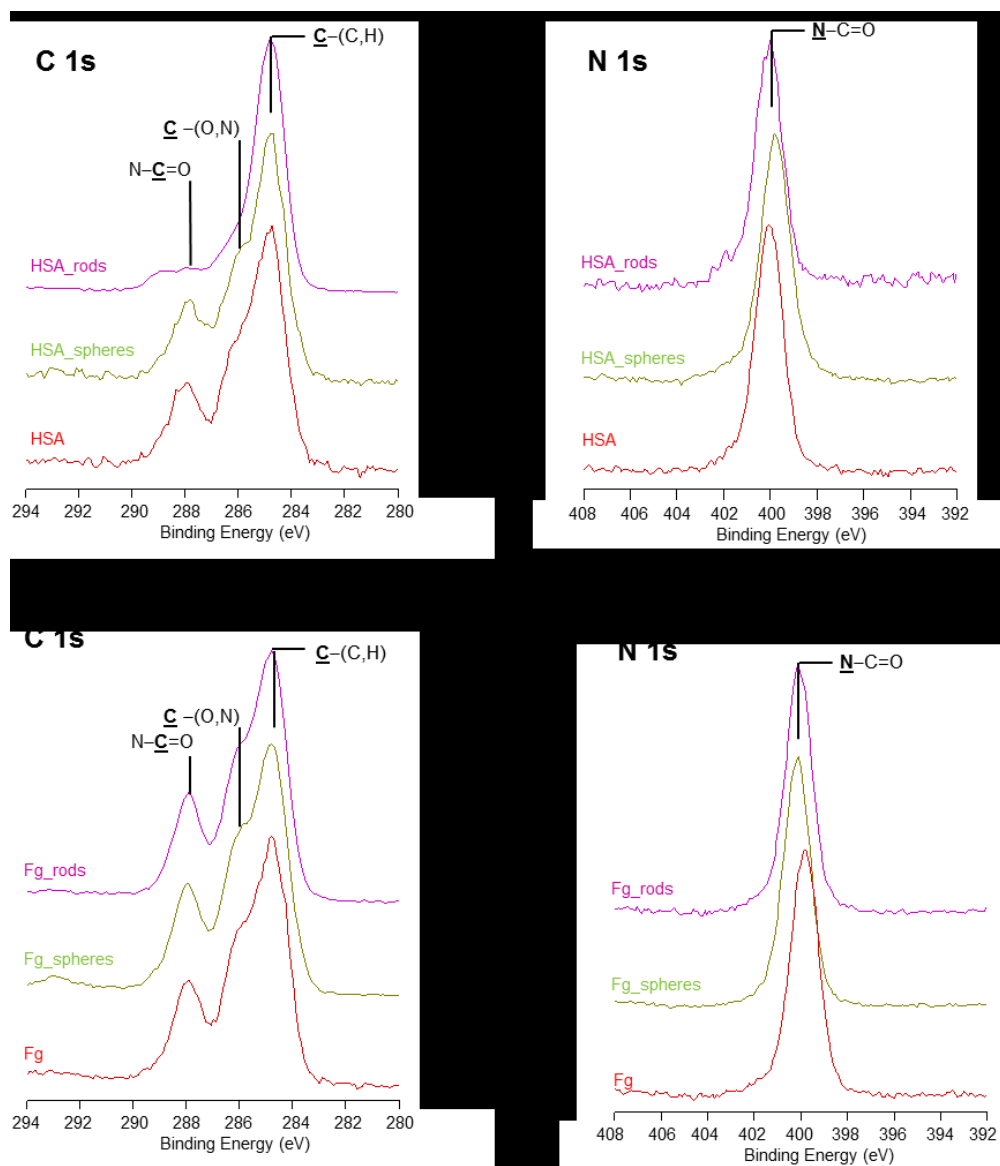


Figure 5.8: XPS C1s spectra and N1s spectra for adsorbed HSA and fibrinogen onto SiO₂ substrate.

Atomic percentage %	C1s	O1s	Ti2p	Si2p	N1s	Na1s	Cl2p
HSA	42.8	21.1	bdl	24	7.4	1.8	2.8
HSA-Nano_S	49.1	20.7	0.1	20.1	8.7	1.3	bdl
HSA-Nano_R	67.9	14.7	bdl	13.6	3.6	0.3	bdl
Fg	61.3	15.6	bdl	4.6	12.2	1.6	4.7
Fg-Nano_S	57.7	18.6	0.1	11.3	11.6	0.9	bdl
Fg-Nano_R	60	17.2	bdl	9.5	11.8	1.5	bdl

Table 5.2: Relative atomic composition (atom %) of SiO₂ surface after HSA and fibrinogen adsorption with and without TiO₂ NPs

B. Organization of the protein layer in dried state

The structure of adsorbed protein layer was analyzed by air AFM measurement in peak force tapping (PFT) mode. The measurements were performed in the presence of TiO₂ nano-spheres and without TiO₂ NPs for the two proteins.

a. Organization of fibrinogen layer in the dried state

In the absence of nano-spheres, the adsorbed fibrinogen presents a regular pattern with the appearance of micro fibrils as shown on figure 9: A. The topography image and the corresponding cross section showed the presence of holes in the protein film with regular size and depth length of 2.5 nm, showing a high degree of molecular organization. In the presence of nano-spheres the adsorbed protein layer changes (figure 9: B). The AFM topography image reveals a more discontinuous film with aggregate on the surface, and the appearance of larger fibrils than without NPs. This observation is confirmed by the cross section, the fibrils are more varied in size and no holes are observed. The image zoom on figure 9 (C and D) confirms these observations, presenting a structured pattern of fibrinogen molecules with a mean length of 50nm which is characteristic of adsorbed fibrinogen on hydrophilic surface¹⁵ without NPs, while in the presence of nano-spheres on the surface the molecule of fibrinogen looks aggregated and no structure is identifiable.

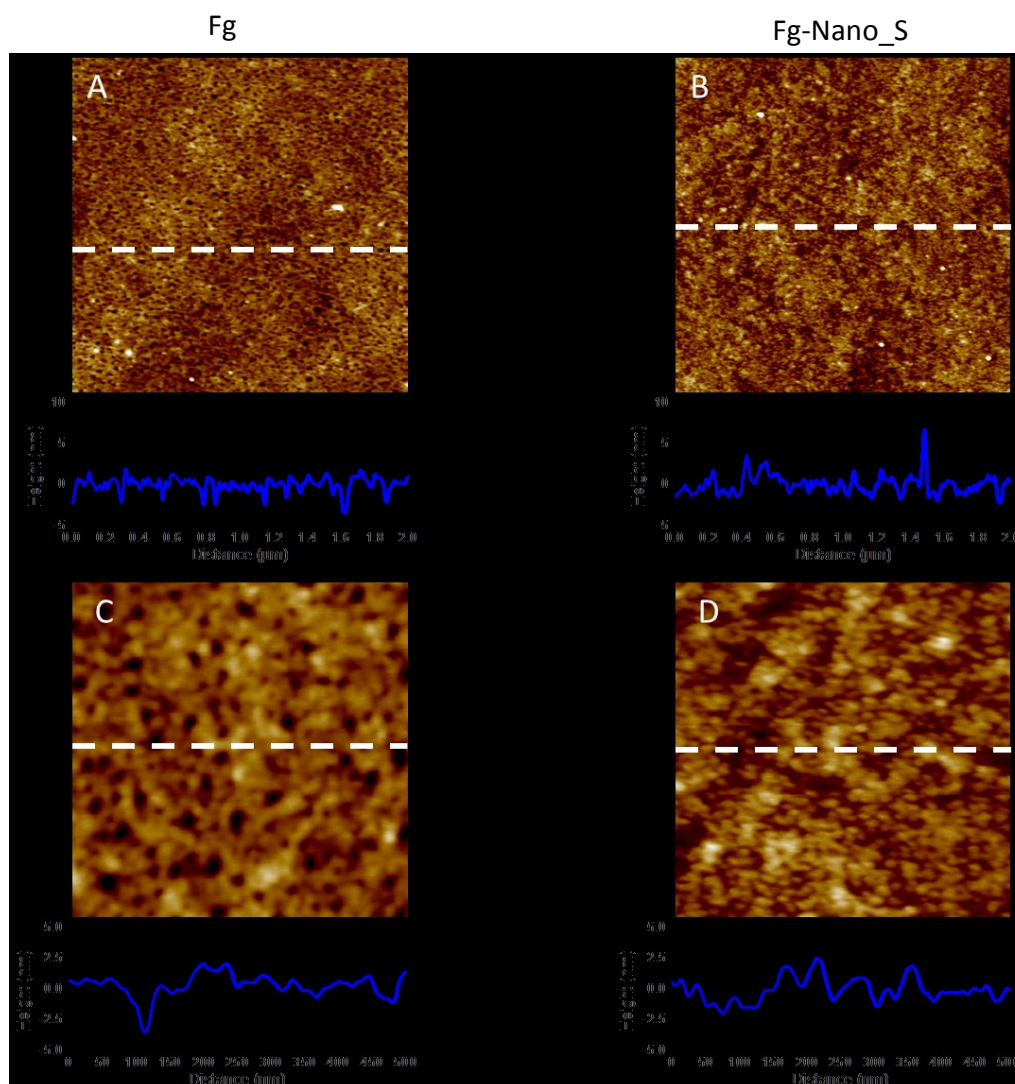


Figure 5.9: AFM topography image PFT mode in air of a SiO₂ substrate surface with fibrinogen adsorbed by procedure II, z-scale -4/4 nm: (A) without NPs and (B) with nano-spheres images (2 μm *2 μm), (C) without NPs image (500 nm* 500 nm), (D) with nano-spheres. Cross sections were taken at the location indicated by dashed lines

b. Organization of HSA layer in the dried state

In the absence of nano-spheres the adsorbed HSA presents a structured film (figure 10: A). The AFM topography image and the corresponding cross section show the presence of holes and aggregates with various sizes. These aggregates may be due to agglomerated HSA or to the salt in PBS solution. In the presence of nano-spheres the structured film disappears totally and the formation of consequent aggregates is visible (figure 10: B). The AFM image and the cross section show an alternation of flat surface and aggregates. This observation suggests a high degree of protein aggregation on the surface in the presence of nano-sphere. Regarding the image C (figure 10) the height of the segments of the network is 2.5 nm, comparing to the dimension of individual HSA molecule (3 nm) suggesting that the network structures are composed of individual HSA without NPs.

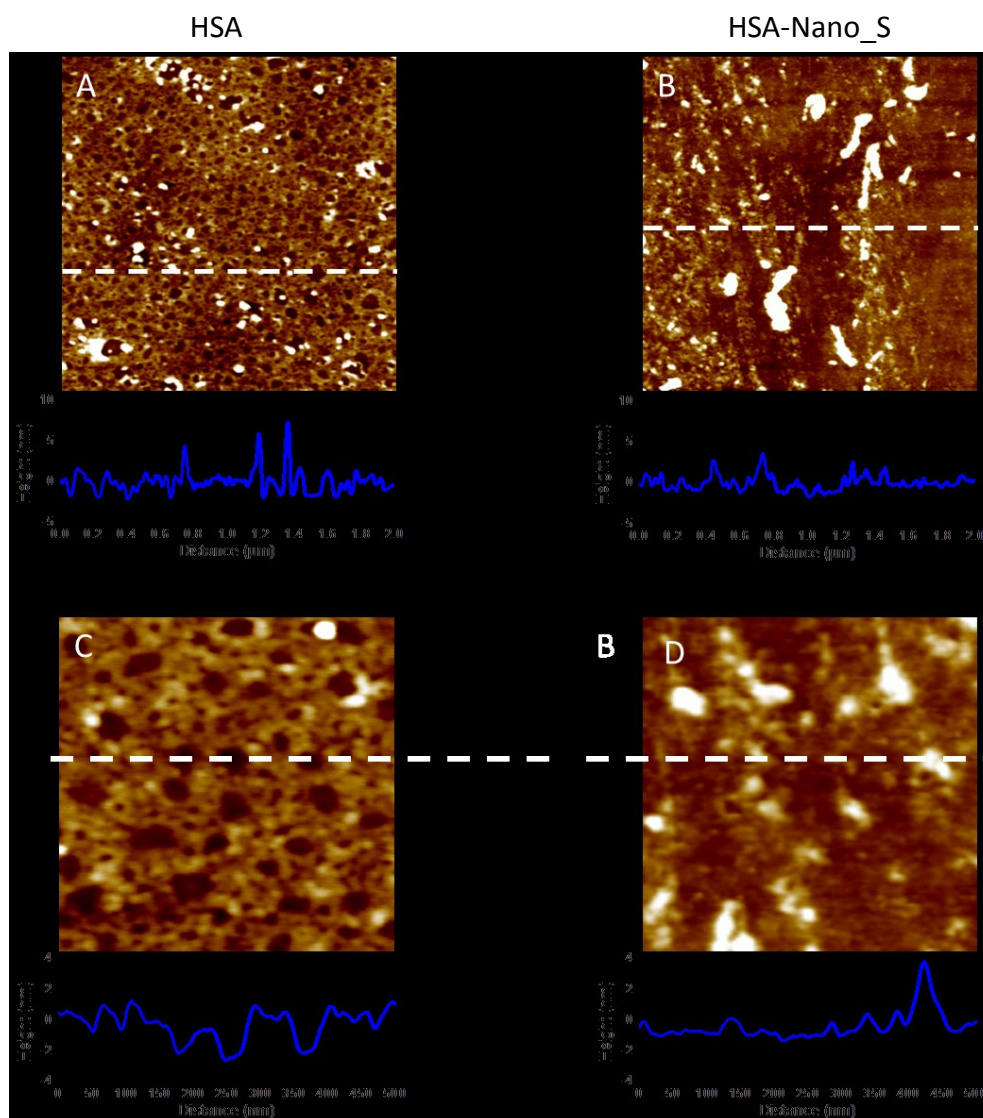


Figure 5.10: AFM topography image PFT mode in air of a SiO₂ substrate surface with HSA adsorbed by procedure II, z-scale -4/4 nm: (A) without NPs and (B) with nano-spheres images (2 μm*2 μm), (C) without NPs and (D) with nano-spheres image (500 nm* 500 nm). Cross sections were taken at the location indicated by dashed lines

IV. Events in liquid phase

The goal of this part is to characterize the impact of NP-protein interaction in solution on protein adsorption at physiological condition, and the involved mechanisms. Though HSA and fibrinogen possess a net negative charge at physiological pH, these proteins present different behaviors which depend on the TiO₂ NPs presence and of the experimental conditions of pre-incubation (time and temperature). This result is not surprising, as mentioned in the introduction due to their difference of size and molecular weight, fibrinogen possesses a high surface affinity and have a strong tendency to self-assemble, forming packing similar to fibrin fibrils¹⁶ contrary to the HSA which possess a highest diffusion constant. Regarding AFM data, HSA and fibrinogen adsorbed layers present various patterns in the presence of NPs comparing without NPs, therefore, no significant changes are observed between nano-rods and nano-spheres. IR-ATR data suggest that the secondary structure of fibrinogen is not impacted by the interaction with NPs in solution. While for HSA the secondary structure seems impacted by the protein-nanoparticle interaction, a change of intensity of the α -helix contribution is observed in the presence of TiO₂ nano-rods for the shortest incubation time.

By analyzing IR-ATR spectra and regarding the supramolecular organization of adsorbed proteins two different mechanisms may be suggested: (I) An indirect action of TiO₂ NPs during the pre-incubation step by modifying the properties of protein solution such as the viscosity which may influence the adsorption behavior of protein at the interface (II) A direct action of TiO₂ NPs during the pre-incubation step resulting in the alteration of proteins properties by the NPs and involving chemical or electrostatic binding. In the experimental conditions used in this study, TiO₂ NPs are in a predominant aggregated state, moreover in PBS solution a partial inhibition of their catalytic properties is observed (see chapter 3) suggesting the absence of formation of ROS species which may deteriorate the proteins.

A. Mechanism of fibrinogen-TiO₂ NPs interaction in solution

The electrostatic interaction is essential in the adsorption of fibrinogen on a surface. The structure of fibrinogen consists of several globular domains, two outer globular D domains and the central globular E domain. A linear coiled-coil region forms the connection between each D domain and the central E domain with two α C termini domains. The D and E domains are negatively charged, whereas the α C termini are positively charged at physiological pH. On hydrophilic surface it was proposed that fibrinogen interacts through the carboxyl terminus of the R-chains¹⁷. SiO₂ surface retains some Si-OH which determines the hydrophilic character of the surface. At physiological pH these groups are weakly acid (Si-OH, pK_a = 6-7), and the surface charge is negative. The electrostatic interaction between fibrinogen molecule and the surface is governed by the α C termini domains and

the negative charge of SiO₂ substrate. Regarding AFM results fibrinogen is strongly impacted by the change of incubation time, this result is in agreement with the literature. The fibrinogen adsorption is composed of two phases, one with dimers or oligomers and another with a three dimensional network. Yang et al¹⁸, has reported an adsorption with two consecutive steps: firstly, the fibrinogen molecules were adsorbed on the surface, secondly, the rearrangement of adsorbed fibrinogen or multilayer adsorption occurred. Nattich et al¹⁹ showed at pH 7.4 the fibrinogen monolayers adsorbed includes two populations of molecules: one irreversibly bounds on the surface, and the other reversibly. This explains the observed decrease of the roughness value when the time of incubation increase, the number of molecules with reversible bounds decrease with the incubation time by the formation of a fibrinogen network. It is less easy to explain the observed effect in presence of NPs at 20 min of time incubation in the presence of NPs. At 20°C and 37°C a homogeneous film with slight topographical variations is observed, suggesting the adsorption of mono-protein network layers without protein agglomeration. This can be due to a lower proportion of fibrinogen molecules with reversibly bound on the surface. The main question is to know if this effect is due to the interaction in solution between NPs and fibrinogen or by an indirect action of TiO₂ NPs. The liquid ATR spectra show no variation of the intensity amide bands, suggesting that the different secondary structures of fibrinogen are not impacted by the presence of NPs in solution. This observation is consistent with the observed network in AFM. Indeed the fibrillation of fibrinogen is initiated by the α C-domains of the molecule, the number of α -helix decreased gradually during the adsorption²⁰ and these last have to be intact to form a complete network during the adsorption¹⁶. Moreover, no difference is observed between the two different experiment temperatures of pre-incubation. Regarding these information we may suppose that the fibrinogen is absorbed in the same condition. The observed effect may due to an indirect action of TiO₂ NPs changing the solution property of fibrinogen.

B. Mechanism of HSA-TiO₂ NPs interaction in solution

Previous studies reported that HSA adsorbed more strongly on hydrophobic surfaces than hydrophilic surface due to hydrophobic interaction which explains the attraction between the non-polar regions of HSA molecules and the hydrophobic surface. HSA is submitted to the Vroman effect, meaning that HSA undergoes a series of adsorption and displacement, due to the protein mobility. For HSA the increase of pre-incubation time leads to a slight increase of the surface roughness without NPs on the adsorbed phase. In the presence of NPs, the formation of these aggregates is more important for the high temperature, this difference may due to the fact that increasing the temperature increases the diffusion constant of the HSA molecule²¹. HSA possesses relative low binding with the surface, after rinsing by PBS HSA molecules should be desorbed from the surface in

same quantity unless these are submitted to a structural change leading to a stronger adsorption. The liquid ATR spectra present important variation in ratio intensity amide band, especially in the presence of nano-rods at 37°C and 20 min, this variation may be due to an alteration of the α -helix secondary structures by the NPs. The interaction between NPs and protein involves electrostatic interaction, Olivia et al² has studied the interaction between HSA and TiO₂ colloidal NPs and shows that TiO₂ NPs interact with HSA by electrostatic interaction at physiological pH. At pH= 7.4 the predominant TiO₂ surface groups are Ti₂=O⁻ and Ti-OH, while the main protein functional groups are R-COO⁻ and R-NH₃⁺. In this condition electrostatic interaction may occur between the different chemical groups at the interface NPs-proteins leading to various interactions such as Ti₂=O⁻NH₃-R (electrostatic interactions) and Ti-OH...⁻COO-R (hydrogen bonding interaction). On the other hand Klotz et al²² found that phosphate ions formed complexes with albumin, on the chapter III the behavior in solution at physiological condition of TiO₂ NPs was investigated. It was proposed that TiO₂ NPs surface are submitted to the adsorption of phosphate ions (HPO₄²⁻). Here we may suppose that the observed effects are due to an electrostatic interaction in solution between the HSA molecule and the charged groups on the NPs surface.

V. Events in the adsorbed phase

In this part the proteins are adsorbed on the silicon substrate during 2 hours, after this time the protein solution is gradually replaced by a NPs suspension and the NPs interact with the adsorbed protein layer during 24 hours. The first observation is that in the both cases (HSA and fibrinogen) XPS data do not show Ti2p signal with nano-rods and a relative low intensity signal in the presence of nano-spheres. The sedimentation test of NPs performed in PBS, and described in chapter III, suggest that the majority of injected NPs should come in contact with the adsorbed protein layer for an incubation time of 24h. Moreover, the absence of Ti2p signal in the XPS data suggests that the NPs are removed from the protein layer during the step of washing or drying. AFM analyses show that the adsorbed protein layer is impacted by the presence of nano-spheres in the both cases. For fibrinogen the observed pattern present a lower degree of supramolecular organization in the presence of nano-spheres. While, in the case of HSA the observed effect is more drastic, the protein layer deteriorates in the presence of nano-spheres presenting a high degree of aggregation on the surface.

Regarding the used procedure two different mechanisms may be suggested: (I) A direct action of TiO₂ NPs at the interface protein layer-NPs suspension by electrostatic interaction (II) A direct action of TiO₂ NPs during the drying step by friction of the NPs on the adsorbed protein layer.

A. Mechanism of fibrinogen-TiO₂ NPs interaction in dried state

Fibrinogen presents a regular pattern in the absence of NPs on SiO₂ surface, while, in the presence of nano-spheres the film presents a discontinuous organization. XPS data shows a slight variation intensity of peptide signal and an increasing of Si2p signal is observed in the presence of NPs suggesting a lowest surface coverage of proteins. Regarding the previous observation in liquid phase the fibrinogen presents no specific interaction with the NPs. In this method the rinsing step consists to replace gradually the solution of protein by a solution of NPs and then by a PBS solution, in this condition it seems unlikely that adsorbed fibrinogen molecule formed a complex or interact with the NPs on the surface. Here we suppose that the observed effect of NPs on the organization of adsorbed state is due to the drying step under N₂ flux. Submitted to the N₂ flux the NPs may remove a part of fibrinogen molecules which are reversibly binding on the protein layer by friction.

B. Mechanism of HSA-TiO₂ NPs interaction in dried state

HSA presents an assembly structure in the absence of nano-spheres on SiO₂ surface, the cross section indicates that the height of the segments of the network is 2.5 nm, comparing to the dimension of individual HSA molecule (3 nm)² this suggest that the network structures is compound by individual HSA. In the presence of nano-spheres the film is degraded, presenting lots of aggregates on the surface. XPS analyses reveal an equivalent amount of adsorbed protein in the presence of nano-spheres and without NPs, this suggests that the observed aggregates are not due to the presence of salt on the surface but to aggregated HSA. The observed effect on the protein layer in the presence of nano-spheres can be explained by the fact that the HSA is weakly bound to the surface. Such as for fibrinogen the involved mechanism may be attributed to the friction of NPs during the drying step. This effect is enhanced by the fact that HSA is weakly bound to the surface. In the presence of nano-rods XPS data shows a net decreasing of peptide bond contribution, two possibilities are plausible, either the protein layer is greatly impacted by the nano-rods or the observed phenomenon is due a surface contamination.

VI. Conclusion

The behavior of HSA and fibrinogen in the presence of TiO₂ NPs was investigated in solution at physiological condition and on adsorbed dried phase on a hydrophilic surface. HSA and fibrinogen show different behavior in the presence of NPs under different experimental conditions of temperature and time of pre-incubation. Moreover, comparing the results in solution and in adsorbed dried phase, some differences are observed.

In liquid phase HSA was influenced by the presence of NPs and the change of experimental temperature, a shape effect of TiO₂ NPs is observed with the nano-rods. The observed changes in liquid ATR spectra suggest that in the presence of nanoparticle the secondary structures of the HSA are impacted by the interaction with the NPs. This is traduced by an increasing of protein agglomeration in the adsorbed state in liquid phase. Investigation on the adsorbed dried state by AFM imaging measurement reveals a disorganized protein layer in the presence of nano-spheres with consequent aggregates on the surface. On the other hand XPS data suggest that the quantity of proteins on the surface is not impacted in the presence of nano-sphere confirming that the observed aggregates are composed of agglomerated HSA.

Contrary to the HSA, the fibrinogen seems not impacted by the NPs shape and more generally by the presence of NPs in solution. However, slight differences are observed on the adsorbed state in liquid phase in the presence of NPs for the shortest incubation time, suggesting that an indirect action of TiO₂ NPs changing the property of fibrinogen solution. In dried phase the XPS data presents an increasing of Si2p signal in the presence of NPs suggesting a lowest surface coverage of the protein layer.

For the two proteins the observed conformational change of the adsorbed protein layer in dried state may be attributed to the effect of drying in the presence of NPs by a friction effect. While in solution the structure of HSA seems impacted by the NPs, suggesting an interaction between the HSA and the TiO₂ NPs contrary to the fibrinogen.

VII. Bibliography

1. Simón-Vázquez, R., Lozano-Fernández, T., Peleteiro-Olmedo, M. & González-Fernández, A. Conformational changes in human plasma proteins induced by metal oxide NPs. *Colloids Surf. B. Biointerfaces* **113**, 198–206 (2014).
2. Oliva, F. Y., Avalle, L. B., Cámara, O. R. & De Pauli, C. P. Adsorption of human serum albumin (HSA) onto colloidal TiO₂ particles, Part I. *J. Colloid Interface Sci.* **261**, 299–311 (2003).
3. Cedervall, T. *et al.* Understanding the nanoparticle-protein corona using methods to quantify exchange rates and affinities of proteins for NPs. *Proc. Natl. Acad. Sci. U. S. A.* **104**, 2050–2055 (2007).
4. Wang, X., Herting, G., Odnevall Wallinder, I. & Blomberg, E. Adsorption of bovine serum albumin on silver surfaces enhances the release of silver at pH neutral conditions. *Phys. Chem. Chem. Phys.* **17**, 18524–18534 (2015).
5. Nakanishi, K. *et al.* REVIEW On the Adsorption of Proteins on Solid Surfaces, a Common but Very Complicated Phenomenon. **91**, 233–244 (2001).
6. Adams, a L. in Plasma at. **55**, 156–159 (1980).
7. Mosesson, M. W. Fibrinogen and fibrin structure and functions. *J. Thromb. Haemost.* **3**, 1894–1904 (2005).
8. Green, R. J., Davies, M. C., Roberts, C. J. & Tendler, S. J. B. Competitive protein adsorption as observed by surface plasmon resonance. *Biomaterials* **20**, 385–391 (1999).
9. Marder, V. J. & Shulman, N. R. High molecular weight derivatives of human fibrinogen produced by plasmin. II. Mechanism of their anticoagulant activity. *J. Biol. Chem.* **244**, 2120–2124 (1969).
10. Noh, H. & Vogler, E. a. Volumetric interpretation of protein adsorption: Competition from mixtures and the Vroman effect. *Biomaterials* **28**, 405–422 (2007).
11. Ortega-Vinuesa, J., Tengvall, P. & Lundström, I. Aggregation of HSA, IgG, and Fibrinogen on Methylated Silicon Surfaces. *J. Colloid Interface Sci.* **207**, 228–239 (1998).
12. Keere, I. Van De, Willaert, R., Hubin, A. & Vereecken, J. Interaction of human plasma fibrinogen with commercially pure titanium as studied with atomic force microscopy and X-ray photoelectron spectroscopy. *Langmuir* **24**, 1844–1852 (2008).
13. Yermolenko, I. S., Lishko, V. K., Ugarova, T. P. & Magonov, S. N. Supporting information High-Resolution Visualization of Fibrinogen Molecules and Fibrin Fibrils with Atomic Force Microscopy. 1–4 (2011).

14. Ray, S. & Shard, A. G. Quantitative analysis of adsorbed proteins by X-ray photoelectron spectroscopy. *Anal. Chem.* **83**, 8659–8666 (2011).
15. Steiner, G., Tunc, S., Maitz, M. & Salzer, R. Conformational changes during protein adsorption. FT-IR spectroscopic imaging of adsorbed fibrinogen layers. *Anal. Chem.* **79**, 225–228 (2004).
16. Koo, J. *et al.* Evaluation of fibrinogen self-assembly: Role of its C region. *J. Thromb. Haemost.* **8**, 2727–2735 (2010).
17. Agnihotri, A. & Siedlecki, C. a. Time-Dependent Conformational Changes in Fibrinogen Measured by Atomic Force Microscopy. *Langmuir* **20**, 8846–8852 (2004).
18. Yang, Q. *et al.* Study of fibrinogen adsorption on hydroxyapatite and TiO₂ surfaces by electrochemical piezoelectric quartz crystal impedance and FTIR-ATR spectroscopy. *Anal. Chim. Acta* **597**, 58–66 (2007).
19. Nattich-Rak, M., Adamczyk, Z., Wasilewska, M. & Sadowska, M. Revealing fibrinogen monolayer conformations at different pHs: Electrokinetic and colloid deposition studies. *J. Colloid Interface Sci.* **449**, 62–71 (2015).
20. Yongli, C. *et al.* Conformational Changes of Fibrinogen Adsorption onto Hydroxyapatite and Titanium Oxide NPs. *J. Colloid Interface Sci.* **214**, 38–45 (1999).
21. Kopac, T., Bozgeyik, K. & Yener, J. Effect of pH and temperature on the adsorption of bovine serum albumin onto titanium dioxide. *Colloids Surfaces A Physicochem. Eng. Asp.* **322**, 19–28 (2008).
22. Klotz, I *et al.* The binding of organic ions by proteins buffer effects. *J. Phys. Chem.*, **1949**, 53 (1), pp 100–114

Appendix I

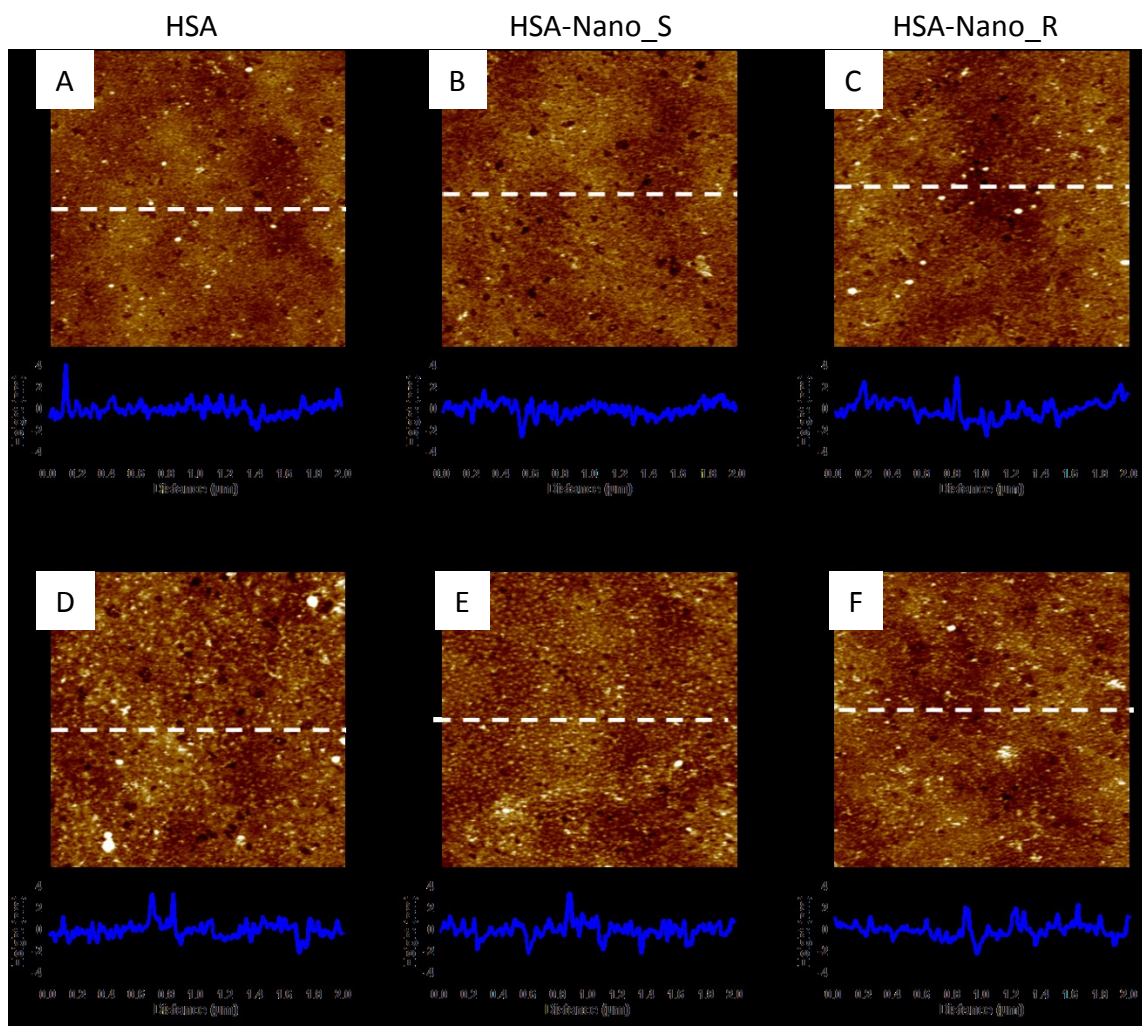


Figure S1: AFM topography image PFT mode in liquid images (2 μm *2 μm) of a SiO₂ substrate surface with HSA adsorbed, z-scale -4/4nm: (A) 24h 20°C without NPs, (B) 24h 20°C ° with nano-spheres, (C) 24h 20°C ° with nano-rods, (C) 24h 37°C without NPs, (D) 24h 37°C with nano-spheres, (E) 24h 37°C with nano-rods. Cross sections were taken at the location indicated by dashed lines

Appendix II

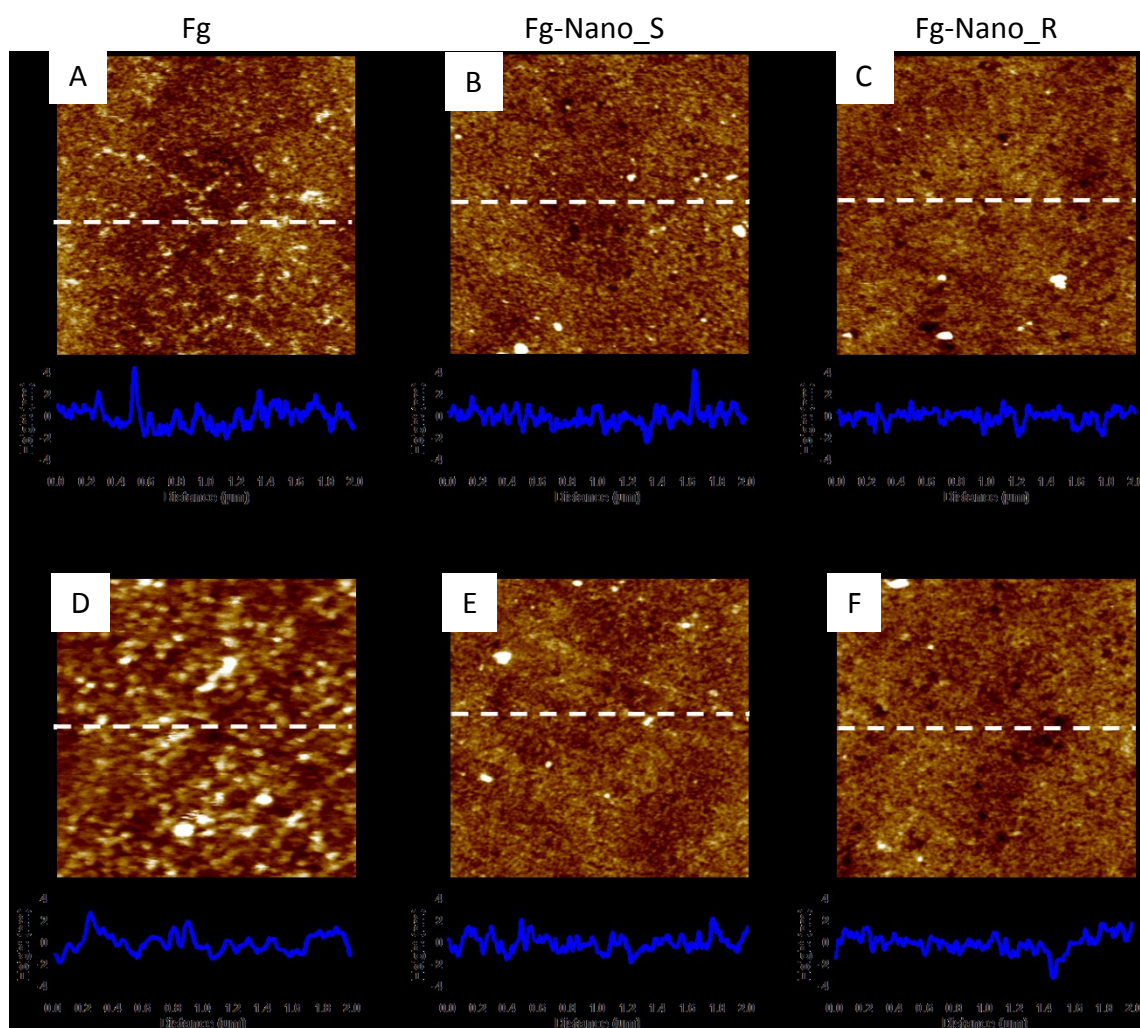


Figure S2: AFM topography image PFT mode in liquid images (2 μm *2 μm) of a SiO₂ substrate with fibrinogen adsorbed, z-scale -4/4nm: (A) 20min 20°C° without NPs, (B) 20min 20°C° with nano-spheres, (C) 20min 20°C° ° with nano-rods, (D) 24h 20°C° without NPs, (E) 24h 20°C° with nano-spheres, (F) 24h 20°C° with nano-rods. Cross sections were taken at the location indicated by dashed lines

Conclusion and perspectives

In the present work, the interaction between three proteins and TiO₂ nanoparticles was investigated under different conditions of incubation and on different phases. The investigated systems were constituted by three different proteins, collagen, human serum albumin and fibrinogen, and two TiO₂ nanoparticles, nano-rods (width of 7.8 ± 0.8 nm, length of 21.8 ± 2.6 nm) and nano-spheres (diameter of 7.6 ± 1.3 nm); this enabled to investigate the effect of size and shape of the nanoparticles on the protein-nanoparticles interaction, and this for proteins having various physico-chemical properties. This work shows that in some cases the presence of nanoparticles affect the protein conformation in the adsorbed phase; in some cases, it does not suggesting that the behaviour of proteins in the presence of nanoparticles depends on the nanoparticle shape as well as on experimental conditions.

In a first time, the chemical and physical properties of synthesized TiO₂ nanoparticles were characterized. The behavior of TiO₂ nanoparticles in solutions, simulating biological fluids, depends on the composition of the surrounding medium and on their shape. Interestingly, nano-rods and nano-spheres present different aggregation states in aqueous environment when increasing the ionic strength. Data showed a dispersive effect of the TiO₂ NPs in phosphate buffer when increasing the ionic strength (modulated by addition of NaCl at constant phosphate concentration). This effect is due to a synergetic effect between phosphate and Na⁺ ions through the formation of NaHPO₄⁻ species, which influence the aggregation state of NPs that is dependent on their shape (rods or spheres). The general behavior in phosphate buffer saline solution reveals an equivalent aggregation such as phosphate solution with 154mM NaCl in both cases (nano-rods and nano-spheres), which depend on the particle size. These results suggest that the proteins interact with agglomerated particles in solution.

The following chapter focuses on the protein-TiO₂ NPs interaction on dried and hydrated phases. An important observation is that the presence of nanoparticles in the dried adsorbed protein layer on silicon and polystyrene wafers was not detected by X-ray photoelectron spectroscopy, suggesting that structural changes observed at the interface are mainly due to the interaction between proteins and TiO₂ nanoparticles in solution, or at the interface surface-protein solution.

The second part of this work focuses on the interaction of TiO₂ nanoparticles with one of the most important extra cellular matrix protein, the collagen. The supramolecular arrangement of the adsorbed phase of collagen greatly depends on the properties of the substrate, showing considerable differences between hydrophilic and hydrophobic substrates on fibril formation. Nanoparticles affect the supramolecular arrangement of collagen molecules especially on a hydrophobic surface, appearing as a significant change in the nanoscale organization of adsorbed collagen. Differences were also observed as a function of the temperature of the medium, incubation time and shape of TiO₂ nanoparticles. AFM force spectroscopy experiments revealed that adsorbed collagen interact differently whether it was pre-incubated with or without NPs after 24h of incubation time, presenting an increase of the rupture length in the presence of sphere or rod-shaped NPs. Moreover, the dewetting process upon drying was shown to be greatly affected by the presence of NPs presenting the formation of dried phases with different morphologies. The process involved in this conformational change may induced by an indirect effect of TiO₂ NPs by the production of ROS species or by modifying the properties of collagen solution.

The last part of this work focuses on the interaction of TiO₂ nanoparticles with two plasmatic proteins possessing different shape and physical properties, HSA and fibrinogen on a hydrophilic substrate. The observed effect on the adsorbed protein layer in solution suggests slight changes of the protein conformation in the presence of nanoparticles. Contrary to the fibrinogen, the HSA which possesses the less adsorption binding and the more important kinetic constant is strongly impacted by the presence of nanoparticles in dried phases, presenting an important structural change. Furthermore, nano-rods do affect HSA structure in solution more strongly than nano-spheres confirming an effect of nanoparticle shape in the involved process. The observed changes on adsorbed phase may due in part to the effect of drying process.

Though the mechanism of interaction between nanoparticles and proteins is not totally elucidated, the results show conformational change of adsorbed proteins in the presence of nanoparticles, depending on nanoparticles size and shape and on experimental condition (temperature and incubation time); to go further in this study, it would be interesting to perform the following experiments:

- (i) Use of biocompatible nanoparticles such as TiO₂ particles functionalized with PEG chains in order to determine the influence of terminal chemical groups on protein-nanoparticles

interaction. Moreover, by varying the size of chains and terminal chemical groups, it would be possible to determine the impact of nanoparticles aggregation in solution on protein-nanoparticles interaction.

- (ii) Nano calorimetric measurement on centrifuged proteins after incubation with nanoparticles to determine the impact on the secondary protein structures resulting from their interaction with the nanoparticles.
- (iii) Electrophoretic measurements on mixing proteins nanoparticles in order to, on one hand characterize the interaction between the used proteins and TiO_2 nanoparticles, and on the other hand determine the surface charge of nanoparticles.
- (iv) AFM force measurement on HSA and fibrinogen after incubation with nanoparticles in order to complete the results, as well as measurement with functionalized AFM tip to perform measurement on unique protein molecule with a nanostructured and functionalized surface as template to control protein adsorption.

Dissemination

Publications

- 1) Thomas Degabriel, Karim El Kirat, Dalil Brouri, Rute Domingos , Sandra Casale, Jessem Landoulsi , Jolanda Spadavecchia : Shape effect of highly crystalline TiO₂ NPs on their aggregation and sedimentation in buffer solutions simulating biological fluids (submit in Colloids and Surfaces A: Physicochemical and Engineering Aspects)

Oral communications

- 1) Thomas Degabriel, Jolanda Spadavecchia, Jessem Landoulsi, Claire-Marie Pradier: Interaction of type I collagen with TiO₂ NPs: Evidences of changes of supramolecular organization in the adsorbed phase; Nano 2014; Moscow; Russia
- 2) Thomas Degabriel, Jolanda Spadavecchia, Jessem Landoulsi,: Interaction of type I collagen with TiO₂ NPs: Evidences of changes of supramolecular organization in liquid and on adsorbed phase; IMPC; Paris: France